

Single-atom imaging of ^{40}K via Raman Sideband Cooling

PhD Thesis

Harikesh Ranganath

First supervisor - Prof. Stefan Kuhr

Second supervisor - Prof. Andrew Daley

Department of Physics

University of Strathclyde, Glasgow

October 7, 2022

Abstract

The focus of this thesis is the trapping, cooling and imaging of fermionic potassium atoms in optical lattice potentials. Our experiment is capable of cooling ^{40}K atoms to a T/T_F of 0.18, well into the degenerate Fermi-gas regime. We then load the atoms into a 3D optical lattice and prepare ~ 500 atoms in one anti-node of the vertical lattice. This 2D ‘layer’ of atoms is imaged with single-site resolution, giving us access to the behaviour of quantum many-body systems in periodic lattice potentials.

The first chapter motivates why this system is so keenly interesting. The experiment aims to function as an analogue quantum simulator for one of the founding questions of quantum theory: the classically inexplicable behaviour of correlated electrons in solid state systems. The second chapter briefly explores the techniques of preparation and control of dilute ultracold gases. The bulk of the thesis, chapters 3 and 4, deal with the design and optimization of the imaging scheme for site-resolved imaging of ^{40}K atoms. In chapter 5, we describe our work with a rubidium quantum-gas experiment, particularly on the laser cooling and state preparation of ^{85}Rb atoms. Finally, we conclude with a look back on what we were able to achieve and learn as well as a look forward to the future of the ^{40}K and ^{85}Rb experiments.

Our results and contributions to the broader field are as follows: We have achieved site-resolved imaging of ^{40}K atoms with $\sim 5\%$ losses via Raman sideband-cooling. Our work characterizing the imaging scheme and the associated challenges adds to the understanding of the vital and broadly applicable technique of RSC. We also compare these results against electromagnetically-induced transparency (EIT) cooling. As we are possibly the only quantum-gas microscope experiment to use both Raman sideband

and EIT cooling, we are uniquely positioned to benchmark both techniques. Additionally, I numerically simulate light-assisted heating and tunneling rates of ^{40}K atoms in the optical lattice via the quantum trajectory technique. The simulations enhance our understanding of our imaging technique as well as contributing to the more general understanding of challenges associated with optically trapping ^{40}K atoms. Finally, our work on implementing grey-molasses cooling of ^{85}Rb has not been demonstrated before. This marks a step forwards in the laser cooling of ^{85}Rb both in quantum-gas microscopes and other cold-atom experiments.

Contents

Abstract	i
List of Figures	v
List of Tables	xi
Acknowledgements	xiii
1 Introduction	1
1.1 High-temperature superconductivity	2
1.2 Electron correlations and the Hubbard model	3
1.2.1 Hubbard Hamiltonian	4
1.2.2 Characteristics of the Hubbard model	6
1.3 Simulating the Hubbard model	7
1.3.1 Neutral atoms in optical lattices	9
1.3.2 Many-body physics with ultracold gases	10
2 Building a quantum simulator	13
2.1 Experimental procedure	14
2.2 Laser cooling	15
2.2.1 Sub-Doppler cooling	16
2.3 All-optical trapping, cooling and transport	18
2.3.1 Crossed optical-dipole trap (CODT) and evaporative cooling	18
2.3.2 Transporting atoms to the science chamber	19

Contents

2.3.3	Optical lattice potentials	20
2.3.4	Selective preparation in a lattice anti-node	20
3	Sideband Cooling	22
3.1	Raman cooling scheme	23
3.1.1	Transition strengths	25
3.2	Implementation and characterization	28
3.2.1	Beam orientations	29
3.2.2	Transition spectra	29
3.2.3	Raman cooling and imaging	33
3.3	Raman imaging optimisation and constraints	35
3.3.1	Inverted excited state	36
3.3.2	Trap inhomogeneity	36
3.3.3	Beam inhomogeneity	39
3.3.4	Optimisation of imaging parameters	41
3.3.5	Benchmarking imaging	42
3.4	Comparing Raman and EIT imaging	43
3.5	Conclusions	47
4	Simulating heating rates	49
4.1	Quantum-trajectory method	50
4.1.1	Computational efficiency	51
4.1.2	Implementation	51
4.2	Two-level atom in a 1D lattice	52
4.2.1	Semiclassical light-atom interaction	53
4.2.2	Including motional degrees of freedom	55
4.2.3	Constructing the initial state	57
4.2.4	Benchmarking with non-inverted excited state	60
4.3	Heating due to inverted excited state	62
4.3.1	Tunnelling probability over time	64
4.4	New intuitions and future work	67

Contents

5	Towards a ^{85}Rb quantum-gas microscope	69
5.1	Experimental setup	70
5.2	Grey-molasses cooling	73
5.2.1	Implementation	74
5.3	Optical pumping for ^{85}Rb	78
5.4	Future work	81
6	Conclusions and outlook	82
A	Discussion of lattice potentials	84
B	Sideband transitions and the Lamb-Dicke parameter	88

List of Figures

2.1	Cross section of experiment chambers: From left to right, (a) ^{40}K oven valve, (b) 2D-MOT chamber, (c) 3D-MOT valve, (d) 3D-MOT chamber and (e) science chamber. Below the science chamber (green) is the microscope objective to collect fluorescence photons.	14
3.1	Three-step Raman cooling cycle: 1. two-photon sideband transition $ n\rangle \rightarrow n-1\rangle$ (red line), 2. transition to excited state (blue line) and 3. decay to ground state preserving motional level $n-1$ (black line). See figure 3.5 to see the internal levels and laser transitions used in our experiment to implement this scheme.	24
3.2	MSquared laser optics setup: $\sim 1.5\text{ W}$ light at 766.7 nm is generated by a Ti-sapphire laser. This is coupled through a 10 m high power fibre to the Raman laser optics board. A wavemeter is used to fine-tune the laser frequency and monitor its stability.	27
3.3	Raman laser optics setup: 766.7 nm Raman light is split into two paths (horizontal and vertical axis beams) with double pass AOMs of opposite order so as to achieve a frequency separation of $4\Delta_{\text{AOM}}$, where $\Delta_{\text{AOM}} = \Delta_{\text{HFS}}/4 + \delta_{2\text{photon}}/4$. D1 resonant polariser (770 nm) is overlapped with the horizontal axis Raman beam.	27
3.4	Beam orientations: Alignment of the lattice and Raman cooling beams to atoms in the science chamber: (a) Top view. (b) Side cross-section.	29

List of Figures

3.5	Level diagrams: D2 (a) and D1 line (b) beams used during Raman imaging. The pumping beams (b) maintain the polarization of the atom and generate the necessary fluorescence for imaging.	30
3.6	(a) Raman spectra and (b) n -level distribution in a deep 3D lattice ($\omega_T = 2\pi \times 330$ kHz): Measuring number of atoms transferred to the $F = 7/2$ manifold vs the two-photon detuning δ of the Raman beams (blue circles in (a)) and corresponding n distribution (blue bars in (b)). The measurement is repeated with pre-cooling the atoms (orange triangles in (a)) with the corresponding n distribution in orange bars in (b).	31
3.7	Polarizer and repumper transitions ((a) and (b) respectively) in a deep 3D lattice ($\omega_T = 2\pi \times 280$ kHz): Scanning the offset frequency of P_1 and P_2 from the master laser provides a spectra with peaks separated by the hyperfine splitting of the $4P_{1/2}$ state.	32
3.8	Width of ^{40}K atom cloud as a function of Raman pulse duration in a deep lattice ($\omega_T = 2\pi \times 300$ kHz), optimal cooling parameters.	33
3.9	Tunneling/Losses: (a) First image of sample taken via 1000 ms exposure to Raman pulse in $2\pi \times 300$ kHz trap. (b) Second image on the same sample taken after 500 ms hold time. (c) From the images we construct a 2D matrix of occupied and unoccupied lattice sites. Comparing occupied sites in the first picture (red circles) and second picture (blue diamonds) allows us to calculate atom loss and hopping rates.	34
3.10	Trap frequency measurement: Modulating the lattice amplitude to drive transitions from $n \rightarrow n + 2$ motional levels in a lattice of $\omega_T = 2\pi \times 200$ kHz (blue circles) and $\omega_T = 2\pi \times 240$ kHz (orange triangles).	38
3.11	EIT imaging: 500 ms exposure of EIT imaging light for (a) sparse and (b) densely filled samples.	44

List of Figures

3.12	Matrix of occupied and unoccupied lattice sites in the central region of images 3.11a and 3.11b ((a) and (b) respectively). The fluorescence per site in locally dense regions of figure (b) is 3-4 times that of the fluorescence of atoms at the edges of the same image.	44
3.13	Failure of image recognition in distinguishing between filled and empty sites in figure 3.11. The left histogram shows the expected two peaks in the per-site fluorescence signal corresponding to empty (near zero) and filled (centred at one) sites. In the right histogram corresponding to dense samples, we are no longer able to separate these peaks.	45
3.14	Fluorescence per atom (normalized) against local atom density (measured as filling fraction) for (a) EIT imaging and (b) Raman imaging. We see that fluorescence per atom in Raman imaging is independent of filling fraction while for EIT there is a strong correlation with density.	46
3.15	Fluorescence imaging using RSC: (a) Atom loss fraction (blue circles), tunneling fraction (orange triangles), and (b) fluorescence per atom vs Raman two-photon detuning.	46
3.16	Fluorescence imaging using EIT: (a) Atom loss fraction (blue circles), tunneling fraction (orange triangles), and (b) fluorescence per atom vs EIT two-photon detuning.	46
3.17	CPL (equation 3.9) against two-photon detuning for Raman imaging (blue circles) and EIT imaging (orange triangles).	47
4.1	(a) ^{40}K $4S$, $4P$ and $3D$ levels relative to 1064 nm light. The lightshift of the $4P$ states without the presence of the $3D$ state is shown in grey. An additional lightshift (orange) is experienced by the $4P$ states owing to the $4P \rightarrow 3D$ transition at 1170 nm (b) Anti-trapped $4P$ states in a 1064 nm lattice. Note, light shifts are not drawn to scale.	50
4.2	Three-site 1D optical lattice: $V = V_0 \sin^2(k_L x)$, $x \in [-3\lambda_L/4, 3\lambda_L/4]$, $V_0 = 1400E_r^L$ used in the quantum-trajectory simulations.	57

List of Figures

4.3	Atom wavefunctions in 3-site optical lattice with sites at $x = -\lambda/2, 0$ and $+\lambda/2$. Eigenstates of $n = 0$ vibrational level ((a) $m = 0$, (b) $m = 1$ and (c) $m = 2$) and $n = 1$ vibrational level ((d) $m = 3$, (e) $m = 4$ and (f) $m = 5$) for a three-site 1D optical lattice with $\omega_T = 2\pi \times 300$ kHz with an additional weak Gaussian confinement ($V_G = 0.01 x^2$).	58
4.4	Comparing harmonic oscillator eigenstates and eigenenergies with one-site lattice: (a) Harmonic trap (orange) centred on a one-site 1D lattice (blue). (b) Eigenenergies of harmonic oscillator potential (orange) and one-site 1D lattice (blue). (c) Inner-product of harmonic oscillator and corresponding 1D lattice eigenstate for $\omega_T = 2\pi \times 50$ kHz (orange) and $\omega_T = 2\pi \times 300$ kHz (blue). Figure (d) shows the harmonic oscillator (orange) and lattice (blue) eigenstate wavefunctions corresponding to $n = 4$	59
4.5	Time evolution of key atomic observables up to 10 spontaneous scattering events for a non-inverted excited state: single-site 1D lattice with $\Omega_0 = 5/6\Gamma$, $\Delta = -1/6\Gamma$, $\omega_T = 2\pi \times 300$ kHz. (a) Damped Rabi oscillations of population in excited state. (b) Motional state distribution. (c) Momentum gain $\langle \hat{p} \rangle$. (d) Kinetic energy gain $\langle \hat{p}^2/2m \rangle$. (e) Potential energy gain $\langle V_0 \sin^2(k_L \hat{x}) \rangle$. (f) Total energy gain $\langle \hat{H}_X \rangle$. Momentum in $\hbar k$ units, Energies in $\hbar^2 k^2/2m$ units where k corresponds to a D1 photon and m is the mass of a ^{40}K atom.	61
4.6	Heating rate dependence on trap depth ω_T . $\Omega_0 = 5/6\Gamma$, $\Delta = -1/6\Gamma$, $\omega_T = 2\pi \times 200$ kHz (blue), $2\pi \times 300$ kHz (orange), $2\pi \times 400$ kHz (green). Figure (a) Non-inverted excited state: $V_{\text{ratio}} = 1$, (b) Strongly-inverted excited state: $V_{\text{ratio}} = -6$	63
4.7	Energy increase/heating vs laser detuning while maintaining 10 kHz scattering rate.	64
4.8	Energy increase/heating vs effective time for initial motional states $n = 0$ to $n = 5$	65

List of Figures

4.9	Tunneling characteristics in the $n = 0$ vibrational level vs lattice trap depth: (a) J parameter. (b) Tunneling timescale $\tau(J) = \hbar/2J$	65
4.10	(a) Tunnelling parameter J and (b) tunnelling timescale $\tau = \hbar/2J$ for atoms in energy band n in a lattice of $\omega_T = 2\pi \times 300$ kHz.	66
4.11	Probability of atom staying in the central site of a 3-site lattice over increasing effective time $\Gamma_{\text{eff}}t$. Simulated for different initial motional state n for light-field parameters $\Omega = 2.5\Gamma$, $\Delta = -10\Gamma$, $\omega_T = 2\pi \times 300$ kHz.	67
5.1	3D rendering of Rb experiment, reproduced from [149]	71
5.2	D2 transition level diagram of ^{85}Rb and cooling/repumping transitions for (a) MOT lasers and (b) Λ grey-molasses lasers, adapted from [162].	73
5.3	Circuit diagram depicting microwave signal generation, amplification, and input to microwave antennae/EOM for ^{87}Rb and ^{85}Rb , reproduced from [162].	75
5.4	^{85}Rb atom cloud width as a function of two-photon detuning, plotted for varying global detunings: 1.64Γ (blue circles), 2.47Γ (orange triangles) and 4.94Γ (cyan squares) where $\Gamma = 6.066$ MHz.	76
5.5	Temperature of ^{85}Rb atoms after $1\ \mu\text{s}$ of Λ grey molasses at varying two-photon detuning (global detuning $\Delta = 1.64\Gamma$).	77
5.6	Temperature of ^{85}Rb atoms at varying durations of Λ grey molasses pulse. Two-photon detuning $\delta = 2\pi \times -50$ kHz, global detuning $\Delta = 5\Gamma$	77
5.7	^{85}Rb atom number transferred to $F = 2$ hyperfine level for applied microwave pulse detuning.	79
5.8	^{85}Rb optical pumping: pulse duration and resulting atom population in states $ F, m_F\rangle = 3, -3\rangle$ (blue circles), $ 3, -2\rangle$ (orange triangles) and $ 3, -1\rangle$ (cyan squares).	80
A.1	Comparing lattice potential $U_L = U_0 \sin^2(k_L x)$ (blue), 1st term of U_L Taylor expansion - $U_{HO} = m\omega^2/2$ (orange) and sum of 1st and 2nd terms (green).	85

List of Figures

B.1 Lamb-Dicke parameter in the vertical (blue) and horizontal axes (orange)
as a function of lattice depth. 91

List of Tables

2.1	Summary of molasses cooling schemes: $\delta = \omega - \omega_0$ where ω_0 is the resonance frequency for the cooling transition. Optimal detuning per technique depends on multiple factors, values in table indicate an approximate value where the cooling scheme becomes effective. The cooling/polarizer transitions for the standard molasses and red-molasses schemes are the $F = 9/2 \rightarrow F' = 11/2$. The grey-molasses and Λ grey-molasses schemes drive the $F = 9/2 \rightarrow F' = 9/2$ transition. The repumper is tuned near-resonant to the $F = 7/2 \rightarrow F' = 9/2$ transition. For the implementation of these schemes in our experiment, see [22].	17
3.1	Inhomogeneity sources and the resulting frequency variation: Variations in the frequency of Raman red-sideband transitions from $ 9/2, -9/2\rangle \rightarrow 7/2, -7/2\rangle$ across a 50 μm diameter field of view.	39
3.2	Detuning and scattering timescales for beams used during fluorescence imaging. Scattering rate of P_2 reflects the repumping rate of atoms prepared in $ F, m_F\rangle = 7/2, -7/2\rangle$ manifold. All other beams scatter from a 60:40 mixture of $ 9/2, -9/2\rangle$ and $ 9/2, -7/2\rangle$	42

Acknowledgements

A full account of all the support I've received would require its own thesis. The busy reader may skip this section but take away only that I have been extraordinarily fortunate with the people in my life and PhD. These acknowledgements may be unusually long, but well, these were unusual times.

First, I must thank my parents, for their unwavering faith in me and willingness to bet on me at every turn. My wisest decision was to be as less unlike them as possible. I'm nothing without their love and support, and it will be the work of a lifetime to live up to their example. Another early stroke of fortune was to be born a twin (I highly recommend this). Hrishi's faith in me, even when undeserved, was an unending comfort in all weathers. Bhargav, and his courage to face his adversities was a constant inspiration. Shruthi further enriched all our lives simply by becoming part of it.

I would never have dreamed to return to physics if not for Vishala, whose example was a shining north star. Watching her, I could not help but walk forward even should my feet tremble. Your friendship filled this decade with immense love, joys, sorrows, inside jokes and erratic adventures. Amogh, who has been my best friend and brother for more than half my life, made my life richer in more ways than I can easily count. I have the rare luxury to know without having to ask that he is ever on my side. I had the great privilege to share music, physics and beers with Gaurav. Rekindling my friendship with him would by itself have been sufficient reward for moving here. Kanaad and 'the bois' became an anchor of my time here, a place where I effortlessly belonged. I would not have survived this pandemic and could not have completed my PhD without all of you, thank you.

Chapter 0. Acknowledgements

From my Masters' program I must specially mention Professors Marco Piani, Andrew Daley, and most of all Stefan Kuhr, who would later go on to be the supervisor of my Masters' thesis and subsequent PhD. I also will never forget Elliott and Marilyn who stayed up all night with me so I could write my thesis. Elliott, know that you will never be rid of me.

On starting my PhD, the lines between friend and mentor are quickly blurred. As example were Andres' and Illian's who introduced me to the lab with great care and professionalism. I am deeply indebted to Manuel and Bruno, who alongside being my role models, were also a lot of fun to work with. Their quiet camaraderie and appreciation of goat farming will forever be fond memories. After Bruno left for more permanent pastures, I was fortunate to retain Manuel's kindness and patient guidance for some more time. I am lucky also to call him a dear friend.

Arthur took over as PostDoc for the rest of my PhD, and somehow always knew what I needed before I knew I needed it. I could never thank him enough for all his guidance and efforts on my behalf, however, to make but a start - thank you, Arthur! Thanks are due also to Dr. Andrea di Carli and his willingness to answer my questions with unending patience. Those of our group will invariably mention Dr. Elmar Haller, who was an almost infallible source of knowledge. The supervisor for your PhD is its most important factor, and I struck gold with Professor Stefan Kuhr. His guidance, enthusiasm and encouragement were an invaluable bedrock for my PhD. He would descend to our labs at every chance he had, and in his passing would leave an air of renewed energy and enthusiasm. Paul, Christopher, Max, Clemens and Lennart, it was a pleasure to be part of the Kuhr group with all of you!

I must also thank members of the EQOP group who made my time here memorable. These legends include Carolyn and Craig with whom I started a book club and a warm friendship during lockdown. James for many an interesting conversation. Also from next door, Sean, Ben and Rachel who survived my ringing laughter the past years and also caused a fair bit of it. Allan, Ross, Nick and Andy whom I always looked forward to bumping into either in our corridors or on the football field. You and many others made sure that when it came time for my farewell, I didnae want to leave.

Chapter 0. Acknowledgements

Lastly, I thank the people who made this thesis and subsequent defence possible. Arthur, Andrea, Manuel and Stefan gave me amazing and detailed feedback. Particularly Stefan and Arthur, who helped in everything from the broad structure and flow to the most minute grammatical corrections for every chapter. This work is vastly better for their interventions. Dr Gordon Robb, the chair for my defence, Professor Thorsten Ackermann and Professor Adrian Kantian who served as examiners went out of their way to make my thesis defence possible from across the pond. I will never not be grateful for their valuable time; my defence and thesis benefited greatly from having both a theoretical and experimental voice. And of course, I must again thank most of all Professor Stefan Kuhr, who gave me these opportunities and made all these experiences possible.

To beloved family, friends and V

Chapter 1

Introduction

Prior to the development of quantum mechanics, a striking new phenomenon was observed that could not be explained classically. Low-temperature studies of mercury [1] in 1911 demonstrated a sharp fall in resistivity on cooling below 4.2 K. Shortly thereafter, this change in phase was observed for tin and lead at 3.8 K and 6 K respectively. In addition to being a fascinating piece of the puzzle that would become quantum theory, the practical significance of the discovery was immediately apparent: perfectly conducting wires of such materials can sustain currents indefinitely without any drop in voltage, decay in current or heating across the wire. Perfect diamagnetism was also observed to emerge simultaneously with the onset of perfect conductivity in 1933 [2]. When these metals were cooled in the presence of a weak magnet, the phase transition is observed indirectly as an expulsion of the external magnetic flux from the material, repelling the nearby magnet. Perfect conductance and perfect expulsion of magnetic fields (known as the Meissner effect) occurring below a critical temperature T_c became the hallmarks of a new phenomenon - superconductivity. Whether the Meissner effect is independent of perfect conductance [3] or if it is the energetically favourable outcome when balancing the magnetic and kinetic energy in a perfect conductor [4], any theory of superconductivity must simultaneously explain both. To this end, the Bardeen-Cooper-Schrieffer (BCS) theory [5] proposes a phonon-mediated pairing between electrons of opposite spin and momentum to create zero-spin Bose particles. The macroscopic occupation of these ‘Cooper-pairs’ into zero-momentum states is at

the heart of superconductivity [6]. As such binding is only possible at energies smaller than typical phonon energies, the theory predicts an upper limit $T_c \leq 30 - 40$ K.

As early as 1935, superconductivity with differing magnetic characteristics was observed [7]. These results were initially considered to arise from inhomogeneities in the experiment sample. The evidence eventually mounted that this was a new class of superconductors - Abrikosov or type-II superconductors [8]. Where the first metallic superconductors (type-I) show perfect diamagnetism up to a critical field H_c beyond which the superconducting phase is broken, type-II superconductors have two critical field values H_{c1} and H_{c2} . At the first critical point H_{c1} , the material is no longer perfectly diamagnetic, however, the superconducting phase survives. Magnetic field lines penetrate the material causing vortexes of normal material surrounded by superconducting current. At the much higher H_{c2} where the density of vortexes through the material is past a critical point, the superconducting phase is lost. Perhaps most striking of all, these materials at temperatures far above T_c show properties incompatible with the conventional theory of metals [9]. At these temperatures, their conductivity drops two orders of magnitude below than that of conventional metals, earning them the title of ‘strange metals’.

1.1 High-temperature superconductivity

The early discovered type-II superconductors like the transition-metal alloys Nb_3Sn and NbN demonstrated critical temperatures at ~ 18 K, i.e. required liquid Helium cooling in application. However, the discovery of Ba-La-Cu-O compounds demonstrating superconductivity at 30 K in 1986 [10] sparked renewed interest in these materials. The T_c record was shattered the very next year with a Yb-Ba-Cu-O compound demonstrating the superconducting phase transition at 93 K [11]. Crucially, the pairing state of these high-temperature superconductors (T_c above the phonon-energy limit) show strong indications of d-wave symmetry [12–14] as opposed to s-wave symmetry in conventional superconductors [15, 16].

With higher critical temperatures (above the boiling point of nitrogen at 77 K),

higher resilience against external magnetic fields and the ability to carry bulk currents, d-wave superconductors promised greater access to real-world applications. Power transmission, magnetic levitation, nuclear fusion reactors and quantum computation are among several fields with potential to be revolutionized by superconductivity [17]. It is then critical to better understand these systems. These discoveries have spurred a phenomenal interest in the physics of solid-state systems with approximately 50,000 papers published on superconductivity and related problems in just the 10 years after their discovery. Refer figure 50.2a,b of [3] for a more complete experimental history of superconductivity. For a phenomenological treatment of the two types of superconductivity, refer [18]. For a review of the most current understanding of high- T_c superconductors and their doping-dependent phase diagram, see [19].

Phenomenological approaches [20] have provided significant insight into phase transitions of condensed matter systems, including the type-I and type-II superconducting phases. However, an *ab initio* microscopic description remains out of reach. In section 1.2, we introduce the simplest microscopic model of electron correlations in a crystal, the Hubbard model [21]. Following this, in section 1.3 we discuss the challenge of simulating this system and the role experiment can play. In doing so, we will justify how quantum-gas microscopes (QGMs) can be a powerful investigative tool, wherein the behaviour of electrons in a crystal can be recreated via neutral fermionic atoms in an optical lattice. In section 2 we introduce the key elements of our experiment - a quantum-gas microscope equipped to prepare ^{40}K atoms in 2D sub-systems of a 3D optical lattice [22].

1.2 Electron correlations and the Hubbard model

Superconductivity was far from the only phenomenon condensed-matter physicists grappled with. Transition metals had been experimentally demonstrated to show a mixture of properties that could not be fully explained solely via atomic descriptions (electrons localized to atoms) or lattice-band theory descriptions ('free' electrons delocalized in real space while being localized in momentum space). As examples of these

dual properties, we observe spin-wave phenomenon in ferromagnetic metals [23]. This is well explained by the Heisenberg model which describes spins localized to lattice sites. At the same time, the observed non-integral magnetic moments per atom of ferromagnets cannot be explained by spin-localized models and require a band-theory description [24, 25]. Furthermore, certain transition-metal oxides predicted to be conductors by band-theory were instead insulators (see table 1 of [26]). These findings suggested a need for a theory of electron correlations that does not disregard the atomic and localized nature of atoms in a lattice [27, 28].

We require of a microscopic model of solid-state systems to capture the qualitative behaviour - the physics - of the system. A ‘good’ model, however, does so with the fewest possible degrees of freedom [29]. I.e., by distilling the system down to the elements essential to its qualitative behaviour, a good model reveals the ‘root cause’ of a physical phenomenon. The approximations made in the process must also be relevant to a broad set of systems such that we can extract physical intuitions that are widely applicable. Under this rubric, among the simplest and most successful descriptions of solid-state systems is the Hubbard model [21, 30, 31] developed independently in England, Osaka and Zurich in 1963. The Hubbard model aims to bridge the gap between the atomic and lattice band descriptions and better explain the characteristics of transition metals including their magnetic properties. When the strongly correlated many-body effect of type-II superconductivity was discovered in 1986, the Hubbard model became a prime candidate to explain this phenomenon.

1.2.1 Hubbard Hamiltonian

The Hubbard model describes correlations between electrons in solid-state systems. Atoms are considered to be fixed in place, forming a periodic crystal lattice. Valence electrons are localized to these lattice sites but are able to tunnel to the nearest neighbouring sites. Despite its simplicity it retains the characteristics of a many-body theory, i.e. inter-particle correlations, with electrons repelling each other when they occupy the same site.

Consider the non-relativistic Hamiltonian for particles (in this case, electrons) in a

periodic 1D potential, [32]

$$\hat{H} = \sum_{i=1}^N \left(\frac{\hat{p}_i^2}{2m} + V_L(\mathbf{x}_i) \right) + \sum_{1 \leq i < j \leq N} V_I(\mathbf{x}_i - \mathbf{x}_j), \quad (1.1)$$

where V_L refers to the periodic potential of the lattice and V_I describes the inter-particle interactions (Coulomb interaction in case of electrons). N is the number of particles on the lattice. This can be re-written as a periodic one-body potential $V_{\text{eff}}(\mathbf{x}_i) = V_L(\mathbf{x}_i) + V_A(\mathbf{x})$ and an effective two-body term $U(\mathbf{x}_i, \mathbf{x}_j) = V_I(\mathbf{x}_i - \mathbf{x}_j) - V_A(\mathbf{x})$, where $V_A(\mathbf{x})$ is an auxiliary potential sharing the periodicity of the lattice. The Hamiltonian is therefore:

$$\hat{H} = \sum_{i=1}^N \left(\frac{\hat{p}_i^2}{2m} + V_{\text{eff}}(\mathbf{x}_i) \right) + \sum_{1 \leq i < j \leq N} U(\mathbf{x}_i, \mathbf{x}_j). \quad (1.2)$$

This approach neglects edge-effects and makes the reasonable assumption that the N -body wave function of the particles on the lattice shares the periodicity of the lattice resulting in a mean-field potential, $V_A(\mathbf{x})$, felt by every particle in the system. The interaction term, U , deals with on-site interactions (which cannot be approximated as a mean field in first quantization). I.e. we associate an energy cost of two particles occupying the same site. This effective inter-particle repulsion is significantly reduced in magnitude and range as compared to the original interaction and can be treated perturbatively.

The eigenstates of the non-interactive periodic Hamiltonian are the Bloch waves [33]. We represent these waves in the Wannier basis:

$$\psi_{\alpha k}(\mathbf{x}) = \frac{1}{\sqrt{N}} \sum_j e^{i\mathbf{k} \cdot \mathbf{r}} w_{\alpha}(\mathbf{x} - \mathbf{R}_j). \quad (1.3)$$

Here, $w_{\alpha}(\mathbf{x} - \mathbf{R}_j)$ are Wannier functions centred at the sites \mathbf{R}_j corresponding to the N ions in the crystal. This ensures that they are plane wave solutions of momentum k strongly localized at the lattice sites R_j , where α refers to the band index. This fits well with the tight-binding approximation that particles are strongly localized at lattice sites and can only tunnel to their nearest neighbours. Applying the single-band

approximation $\alpha = 1$, we arrive at the most familiar form of the Hubbard Hamiltonian (represented concisely in second quantization):

$$\hat{H}_{FH} = -t \sum_{\langle i,j \rangle} (c_{i,\sigma}^\dagger c_{j,\sigma} + \text{h.c.}) + U \sum_i n_{i\uparrow} n_{i\downarrow} = \hat{H}_t + \hat{H}_U. \quad (1.4)$$

The terms $-t$ and U are the nearest-neighbour tunnelling strength and the on-site interaction strength respectively. $c_{i\sigma}^\dagger$, $c_{i\sigma}$ are the on-site creation and annihilation operators where σ indicates spin (either \uparrow or \downarrow). The occupation number of the site i is given by $n_{i,\sigma} = c_{i,\sigma}^\dagger c_{i,\sigma}$. The tunnelling/kinetic component of the Hamiltonian, H_t , couples ordered pairs of nearest neighbour lattice sites $\langle i, j \rangle$. H_U describes a potential energy arising from on-site interaction when two electrons of opposite spin occupy a single site. Finally, in the experimentally relevant context of an additional weakly confining potential, we also include a per-site chemical potential term, $H_c = \sum_i \epsilon_i n_i$, in the total Hamiltonian. A similar treatment can be carried out for bosons in periodic potentials, referred to as the Bose-Hubbard model [34, 35].

1.2.2 Characteristics of the Hubbard model

Without being exhaustive, we discuss the features of the Hubbard model. As a general (and much simplified) intuition, when $|U|/t \ll 1$, tunnelling dominates the inter-particle interaction and we expect metallic behaviour consistent with band theory. When instead, $|U|/t \gg 1$, the Hubbard model reduces to a strongly-localized Heizenberg-like model. All properties of the undoped systems arise from a competition between interaction strength U and the band width $W = 4Dt$, where D is the dimensionality of the system. For different regimes of these parameters in relation to the free-gas Fermi energy E_F , we expect a metal ($U \ll E_F \ll W$), Mott insulator ($E_F \ll W \ll U$) and band insulator ($E_F \gg U, W$).

We are interested in strongly-correlated systems ($U \gg t$) and restrict our discussion accordingly. In such systems at low temperatures, spin ordering occurs due to a ‘virtual hopping’ interaction between opposite-spin particles on neighbouring sites. This does not change the spin configuration at each site, however, the virtual hopping between

sites allows particles to lower their energy (if the hopping is not Pauli-forbidden). The resulting behaviour for half-filling (i.e. an average atom number per site of $n = 1$) can be treated as a Heisenberg-spin Hamiltonian. The Hamiltonian takes the form $\hat{H} = J_{\text{ex}} \sum_{\langle i,j \rangle} \hat{S}_i \cdot \hat{S}_j$, where \hat{S}_i is the spin-1/2 operator at site i and the strength of this superexchange interaction is given by $J_{\text{ex}} = 4t^2/U$. The interaction favours antiferromagnetic ordering for a repulsive ($U > 0$) on-site interaction [36]. Hence, for a temperature $k_B T \leq U$, we expect to see a paramagnetic MI, and at the much lower temperature $k_B T \leq J_{\text{ex}}$, we expect the emergence of an antiferromagnetic MI [37]. These predictions match well with the behaviour of transition-metal oxides [38, 39].

A parameter that greatly alters the behaviour of these compounds is doping, i.e. changing the number of electrons/holes in the system. The presence of holes in the Mott-Insulator makes particles effectively less correlated for fixed interaction strength U [40]. A modification of the Hubbard model known as the t-J model explicitly includes the most likely forms of tunneling for $n \neq 1$, i.e., tunneling from a singly occupied to an empty site and tunneling from singly occupied site to form a doubly occupied site. In addition, this model perturbatively includes the more rare tunneling events such as two electrons simultaneously tunneling to an empty site to form a doubly occupied site, tunnelling between three sites with or without a spin flip at the central site, etc. These additional tunnelling terms and the reduced effective correlation in doped crystals are thought to be key factors in high- T_c superconductivity [41–44], so much so that the undoped parent compounds of cuprate superconductors are typically insulators. Much of current research focuses on better understanding these effects [45].

1.3 Simulating the Hubbard model

The Hubbard model though deceptively simple has withstood every attempt at an exact solution in all but 1D [46, 47]. Numerically simulating such systems, however, are beyond the reach of classical computers [48]. The Hilbert space for a quantum system grows exponentially with the number of particles. Therefore, the necessary size of a classical computer also grows exponentially with the size of the system it aims to

simulate. In describing the behaviour of electrons in solid-state systems, the Hilbert space quickly becomes unwieldy.

Where exact diagonalization is challenging, computational methods typically exploit symmetries of this system or find approximations that reduce complexity while preserving essential characteristics of the system. The commonly applied methods include Hartree-Fock approaches [49], quantum Monte-Carlo (QMC) techniques [50, 51], density-matrix renormalization group (DMRG) algorithms [52, 53], density functional theory (DFT) [54] and dynamical mean-field theory (DMFT) [55]. Each of these techniques have relative advantages and applications to which they are well suited. However, these techniques are typically challenged in higher dimensional systems [56] where entanglement is spread more broadly (damping the advantages of DMRG), finite temperature or high energy systems with a higher density of energy states, fermionic systems (owing to the ‘sign problem’ emerging from anti-symmetry of exchange that introduce negative probability terms in QMC calculations and make difficult DMFT impurity models that rely on QMC), disordered systems that break symmetries, and particularly - strongly-correlated systems (that makes DFT impractical). Hence, it is uncertain the degree to which these techniques are applicable to the Hubbard model, which is a fermionic, strongly-correlated and many-body model.

As of yet, it remains unknown whether the Hubbard model allows for superconductivity except in the small- U limit [57]. Here is where *experimental* quantum simulators [58, 59] can play an invaluable role in understanding exotic many-body phenomenon and the limits of the Hubbard model. They can be used to verify the results from theoretical and numerical techniques as well as access regimes not accessible to these techniques. In section 1.3.1 we explore how atoms in optical lattices [60, 61] provide a simulation platform uniquely suited to modelling Hubbard systems. Later, in section 2 we introduce our experiment, and delve into many of the techniques that have made cold-atom experiments possible.

1.3.1 Neutral atoms in optical lattices

Though the Hamiltonian we have discussed in section 1.2.1 deals with the behaviour of electrons in solid-state systems, the universality of quantum mechanics [62] provides an opportunity to study this Hamiltonian in a more controllable system. In place of electrons, we can use fermionic atoms, and instead of the typical lattice separation scales of angstroms, we trap these atoms in periodic optical potentials of sub-micrometer separation. Internal magnetic states of the atoms serve as proxy for discrete spins spin states of electrons and the on-site Coulomb interaction of electrons of opposing spins can be simulated via *s*-wave scattering of neutral atoms. Atoms illuminated by an optical field experience a potential $V_{\text{dip}}(\mathbf{r}) = -1/2\langle\mathbf{d}\cdot\mathbf{E}(\mathbf{r})\rangle \propto -I(\mathbf{r})$ [63]. The parameter \mathbf{d} is the light-induced atomic dipole moment, $\mathbf{E}(\mathbf{r})$ the laser's oscillating electric-field amplitude and $I(\mathbf{r})$ the spatially-dependent intensity of the laser. Therefore, we can generate spatially periodic potentials for periodic $I(\mathbf{r})$. Most commonly, as is the case in our experiment, these potentials are generated by retro-reflecting optical laser beams to create standing-wave optical fields with a resulting potential of the form $V_x = V_0 \sin^2(k_L x)$ along each axis. See appendix A for a more detailed treatment of the resulting potential.

For the rescaling above to faithfully represent the physical system, the atoms need to be cooled to extremely low temperatures. The de-Broglie wavelength, an estimate of the 'quantum-ness' of a system is defined as $\lambda_{\text{dB}} = (2\pi\hbar^2/mT)^{1/2}$, where m is the mass of the particle and T is its temperature in Kelvin. i.e. $\lambda_T \propto 1/\sqrt{mT}$. Since atoms have mass 10^6 times that of electrons, the atoms have to be cooled to the ultracold regime ($< 1 \mu\text{K}$) such that their de-Broglie wavelength is comparable to their electron counterparts, and cool even further ($\sim \text{nK}$) for λ_{dB} to be on the order of inter-atomic separation. Sections 2.2 and 2.3 discuss how such low temperatures are achieved.

In section 1.2, we discussed what makes the Hubbard model a suitable microscopic model for solid-state systems. Similarly, it is instructive to consider what makes atoms in optical lattices a suitable simulation platform for the Hubbard model. First, this platform provides the essential elements of the Hubbard model - a periodic potential, nearest-neighbour tunnelling and on-site interaction - without introducing additional

degrees of complexity. This is because optical lattice based crystals, in comparison to real materials provide much better homogeneity and low-noise periodic potentials. The second critical advantage of the platform is its low simulation time and high scalability in comparison to classical computers. A Hubbard system can be prepared and measured with a cycle time in the order of a few 10s of seconds. Even accounting for the number of repetitions necessary for reliable statistics this is several orders of magnitude faster than the best supercomputers. In addition, quantum-gas microscopes are highly scalable: capable of simulating quantum systems with hundreds of atoms [64] without appreciable increase in simulation time. Finally, the neutral atom simulation platform offers tunability over a wide range of parameter space. The parameters t , U , depend on the depth of the lattice trapping potential V_0 . Deeper traps reduce the likelihood of atoms being able to tunnel to neighbouring sites, reducing t , while also increasing the confinement and strength of on-site interaction U . The interaction parameter U can be tuned independently by tuning the scattering length of the inter-atom interaction via magnetic Feshbach resonances [65], i.e., both Hubbard parameters are experimentally accessible. This allows us to explore both regimes: $|U|/t \gg 1$ (the interaction dominated, strongly-correlated regime), and $|U|/t \ll 1$ (the hopping dominated regime).

1.3.2 Many-body physics with ultracold gases

Several important review articles track the development and successes of optical lattice simulators (see [36,37,66–70] and most recently [45,71,72]). In this section we highlight a few key experimental milestones for optical lattice experiments that illustrate the features of the Hubbard model.

The early successes were achieved for the Bose-Hubbard model, i.e. bosonic neutral atoms in optical lattices. They were aided by advances in the trapping and cooling of bosonic atoms, particularly the demonstration of Bose-Einstein condensation (BEC) [73] in 1995. A BEC is a macroscopic wavefunction formed when the bulk of microscopic particles in the system occupy the ground state, only possible when atoms are cooled to \sim nK temperatures. In an optical lattice, a BEC has superfluid characteristics, analogous to a conventional s-wave superconductor. In 2002, researchers reported the

observation of the superfluid-MI phase transition of the bosonic Hubbard model [60,74], observed as a sudden and reversible disappearance of the phase coherence across the lattice. A molecular BEC of fermionic atoms was created by tuning the inter-atom interaction strength via Feshbach resonance in 2003 [75]. In 2008, the transitions for the fermionic Hubbard model were also demonstrated [76,77]. Unlike the quantum phase-transition of bosonic systems, the Mott-insulator phase emerges as a crossover-transition from the degenerate fermi-gas, with the transition complete only for $T = 0$.

Quantum-gas microscopes for 2D Hubbard systems

Optical lattice experiments took a big step forward with the development of single-atom resolved imaging of 2D Hubbard systems. Strong confinement (i.e. $t \sim 0$) across one axis of the 3D lattice creates independent 2D optical crystals at each anti-node of the strongly confining lattice beam. Preparing and imaging a single 2D ‘layer’ (atoms in a single anti-node) of this system with high-resolution microscopes allows for unprecedented insight into their microscopic behaviour [78]. Such devices are best known as ‘quantum-gas microscopes’ (QGMs). The necessary experimental techniques to achieve single-atom imaging were pioneered for bosons [79] and used to probe the SF-MI transition with single-atom resolved imaging [80,81]. Due to mixing of P state m_F levels in deep optical traps that make laser cooling inefficient for fermionic atoms ^{40}K and ^6Li , single-atom imaging of fermions was only achieved in 2015 [82,83], followed by the observation of a Mott insulator [84,85].

Quantum-gas microscopes have proven to be powerful investigative tools into superconductivity and related strongly-correlated phenomenon. The QGM-accessible 2D Hubbard model [86] is particularly relevant to superconductivity. Cuprate superconductors are built of 2D copper-oxide planes sandwiched between rare-earth or alkaline-earth oxide layers [87,88] leading to a pseudo-2D structure with planar sheets of charges. In addition, single-atom resolved imaging allows us to measure local correlation functions that are otherwise inaccessible [89,90] including the emergence of anti-ferromagnetic order [91,92]. Lastly, it is an ideal tool to explore the all-important effects of doping [93–95] and microscopic effects such as spin-charge separation [96,97].

Chapter 1. Introduction

Though precise critical temperatures are uncertain, optical-lattice experiments inch ever closer to the temperature regimes where we expect to observe superconductivity in doped systems (see figure 1 of [45]). The species chosen for our experiment, ^{40}K is well suited to the task of simulating the Hubbard model [98, 99]. Particularly, a broad Feshbach resonance at 191 G would allow us to tune the interaction strengths between the $|9/2, -9/2\rangle$ and $|9/2, -7/2\rangle$ states of the ^{40}K hyperfine ground state. A more thorough understanding of single-atom imaging techniques for neutral atoms and specifically ^{40}K (the subject of this thesis), the parameters that dictate its fidelity and limitations is a key part of designing QGMs for many-body physics.

This work is structured as follows. The following chapter describes the building blocks of a quantum-gas microscope and the necessary laser-cooling techniques. As several years of literature on the specific tools and techniques involved exist, we focus on providing an overview and connecting the dots between different laser-cooling schemes. Chapter 3 focuses on the implementation of the Raman sideband-cooling scheme for single-atom imaging. We aim to thoroughly characterize the scheme and compare it against a similar sideband cooling scheme - electromagnetically-induced transparency (EIT) cooling. In chapter 4, we will discuss an approach to simulating the imaging process known as the quantum-trajectory method. This simulation work has been crucial in guiding the optimization of our experiment, and has provided valuable qualitative insights on the behaviour of ^{40}K atoms in optical lattices. Lastly, in chapter 5 we discuss the optical pumping and grey-molasses cooling of a different atom, ^{85}Rb , implemented in a parallel bosonic experiment.

Chapter 2

Building a quantum simulator

Quantum-gas microscopes of today are the culmination of decades of progress in the cooling, trapping and imaging of neutral atoms [66, 69, 100, 101]. The implementation of these techniques in our experiment is well documented in the thesis of D. Cotta [22]. We summarize briefly the cooling and trapping of ^{40}K and discuss our single-atom imaging scheme in the following chapter.

To prevent the condensation of these cold gases, the inter-atomic separation, $n^{-1/3}$ (where $n \sim 10^{12} \text{ m}^{-3}$ is the particle density), should be greater than the length scales of inter-atomic interaction. As discussed in section 1.3.1, the atoms need to be cooled to extremely low temperatures ($\sim \text{nK}$) such that their de-Broglie wavelength exceeds the inter-atomic interaction length scales. Such dilute and ultra-cold quantum gases need to be prepared in ultra-high vacuum ($\sim 10^{-11} \text{ mbar}$) environments such that their coherence and lifetimes are not hindered by collisions with background gases. As a general principle, quantum-gas microscopes aim to trap atoms at ever lower background pressures and atom temperatures. Here, the richest features of the Hubbard model (such as superconductivity in the repulsive Fermi-Hubbard model) would not be hindered by thermal fluctuations or background collisions [45]. Key to achieving these low temperatures are magneto-optical traps (MOTs) (section 2.2) and optical-dipole traps (section 2.3).

2.1 Experimental procedure

Our experiment cools and traps atoms in three interconnected chambers, referred to as the 2D-MOT chamber, 3D-MOT chamber and science chamber (See figure 2.1). A 5% enriched ^{40}K ampoule is heated to $105\text{ }^\circ\text{C}$ in an oven that can be opened to the 2D-MOT chamber. This provides a pressure of 6×10^7 mbar in the 2D-MOT chamber, where we estimate $\sim 10^{11}$ atoms trapped in a cigar shaped cloud. A differential-pumping tube ($\varnothing 1\text{ mm} \times 55\text{ mm}$) along the long-axis of the 2D-MOT opens to the 3D-MOT chamber. Aligned with the 2D-MOT, differential-pumping tube and 3D-MOT is a near-resonant “push” beam that transports atoms from the 2D to 3D MOT. The 3D-MOT captures $\sim 10^8$ atoms, bringing them to a minimum temperature of $29\text{ }\mu\text{K}$ via grey-molasses cooling [102] (section 2.2.1). Atoms are transported 15 cm via an optical-dimple trap from the 3D-MOT chamber to the science chamber (section 2.3) where they are evaporatively cooled to the nanokelvin regime. The 3D-MOT and science chambers are maintained at ultra-high vacuum (10^{-11} mbar).

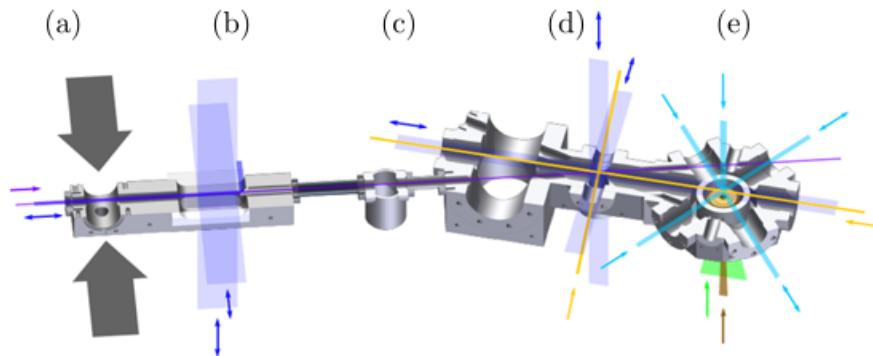


Figure 2.1: Cross section of experiment chambers: From left to right, (a) ^{40}K oven valve, (b) 2D-MOT chamber, (c) 3D-MOT valve, (d) 3D-MOT chamber and (e) science chamber. Below the science chamber (green) is the microscope objective to collect fluorescence photons.

2.2 Laser cooling

Atoms experience two kinds of forces on interacting with light. The first is photon scattering [103]: atoms absorb light to undergo an atomic transition to the excited state, and scatter the light in an arbitrary direction to return to the ground state. Since the atom absorbs photons with momentum in one direction (the direction of laser propagation) and emit photons in a random direction, the atoms gain a net momentum along the field. A second force arises due to a dipole interaction. The light-field brings the atom into a superposition of states, inducing a dipole moment which oscillates with the driving frequency of the electromagnetic field. The former is the basis for the 2D and 3D MOTs, the latter results in a conservative force that allows for all-optical trapping and evaporative cooling.

A magneto-optical trap [104] uses the scattering force from opposing beams of light at frequencies near to the resonant transition to trap and cool atoms. The rate of absorption from each of the opposing beams and thus the magnitude of scattering force depends on the atoms position and velocity [105, 106]. The setup requires two coaxial coils with opposite directional currents to set up a space varying magnetic field (zero at trap center, but increasing magnetic fields on moving away from the center). The counter propagating laser fields have a frequency below the electronic transition frequency ($\omega < \omega_0$ where ω_0 is the resonance frequency) and opposite handedness. Hence, they drive transitions from m_F states of opposite sign. Thus, when an atom moves away from the center, it preferentially absorbs photons from the laser moving opposite its velocity.

More importantly, at these laser frequencies atoms absorb more photons from the beam opposing its velocity as the light is Doppler-shifted closer to resonance. This results in gaining more momentum from one light field than the other, slowing the atoms down. The net force exerted on low-velocity atoms near the centre of the MOT takes the form [106]

$$F_{\text{MOT}} = -\frac{\alpha\beta}{k}z - \alpha v, \quad (2.1)$$

i.e., a force dependent on the atom's position z and velocity v . $\beta = g\mu_B/\hbar\delta B/\delta z$,

where g , μ_B and \hbar are the Lande-g factor, Bohr magneton and planck's constant while B is the external magnetic field. i.e. βz describes the zeeman shift on moving from the centre of the trap to z . The damping co-efficient $\alpha = 2k\delta F/\delta\omega$, where k is the wavevector and ω is the frequency of incident light.

These same principles can be extended to two (2D MOT) and three dimensions (3D MOT) by using a quadrupole magnetic field and opposing lasers from two or three directions (for 2D and 3D MOT respectively). The minimum temperature that can be achieved by a MOT is known as the Doppler cooling limit, $k_B T_D = \hbar\Gamma/2$. The natural linewidth Γ of the cooling transition, typically of the order of \sim MHz, allows for final MOT temperatures $T_D \sim 120 \mu\text{K}$ for ^{40}K when the cooling beams are detuned to $\delta \sim \Gamma/2$.

2.2.1 Sub-Doppler cooling

The Doppler limit (in the μK range) is an order of magnitude hotter than temperatures typically required in optical lattice experiments (\sim nK). To bridge this gap, we look closer at what limits the temperatures achieved in doppler cooling. Equation 2.1 shows an anti-linear relationship between an atom's velocity and the force it experiences. I.e., $\delta F_{\text{MOT}}/\delta v = -\alpha$. This is akin to the atoms experiencing a viscous force, earning this cooling scheme the moniker of "molasses" cooling. The width of the cooling transition sets the capture velocity - atoms moving faster than this velocity are Doppler-shifted out of resonance of both beams and cannot be cooled. The gradient of the velocity-dependent force, $(-\alpha)$, affects the minimum final temperature the scheme achieves. Intuitively, the greater the magnitude of $\delta F/\delta v$ the greater the force that can be applied on atoms with low velocities leading to a slower equilibrium velocity. As $\alpha \propto \delta F/\delta\omega$, broad transitions where the coupling strength changes more gradually with frequency correspond to smaller magnitude of α .

The first stage of molasses cooling in most atomic physics experiments - the MOT - features a broad cooling transition (of the order of $\Gamma = 2\pi \times 6$ MHz for ^{40}K). Hence, it is characterized by the highest capture velocities as well as the hottest final temperature of the molasses schemes [105,107]. This serves as the pre-cooling stage for a grey-molasses

cooling scheme in our experiment. Such enhanced molasses schemes typically feature narrower effective transition widths that allow for lower final temperature with the tradeoff of lower capture velocities. Table 2.1 summarizes the sub-Doppler laser cooling schemes commonly used in atomic physics experiments. While the MOT relied entirely

Cooling Scheme	δ polarizer/repumper	T (^{40}K)
Molasses cooling (MOT)	$-0.5 \Gamma / 0$	$200 \mu\text{K}$
Red/Bright molasses	$-3 \Gamma / 0$	$48 \mu\text{K}$
Grey-molasses cooling	$+3 \Gamma / 0$	$35 \mu\text{K}$
Λ grey-molasses cooling	$+3 \Gamma / +3 \Gamma$	$29 \mu\text{K}$

Table 2.1: Summary of molasses cooling schemes: $\delta = \omega - \omega_0$ where ω_0 is the resonance frequency for the cooling transition. Optimal detuning per technique depends on multiple factors, values in table indicate an approximate value where the cooling scheme becomes effective. The cooling/polarizer transitions for the standard molasses and red-molasses schemes are the $F = 9/2 \rightarrow F' = 11/2$. The grey-molasses and Λ grey-molasses schemes drive the $F = 9/2 \rightarrow F' = 9/2$ transition. The repumper is tuned near-resonant to the $F = 7/2 \rightarrow F' = 9/2$ transition. For the implementation of these schemes in our experiment, see [22].

on the scattering of photons, red molasses or polarization gradient cooling utilizes a combination of photon scattering and the atom-light dipole interaction. Retroreflecting lasers in a $\text{lin}\perp\text{lin}$ configuration causes a spatially varying polarization of the light field experienced by the atoms. This leads to a spatially dependent dipole-interaction, resulting in moving atoms experiencing a periodic lattice potential that depends on the atoms internal state m_J . For example, since opposite m_J levels of the atom couple more strongly to opposite polarizations the lattice potential experienced by atoms in state $-m_J$ is phase shifted by π as compared to that of atoms in state $+m_J$. The laser detuning is chosen such that an atom climbing the top of the dipole potential hill (losing kinetic energy in the process) is pumped to a different m_J state at a lower dipole potential energy (see figure 8.5 of [108]). Hence, the moving atom converts its kinetic energy to dipole potential energy and then is optically pumped to a lower potential energy state, leading to a net cooling effect [109]. This effect dominates over the Doppler cooling of the previous section when the lasers are detuned by $\geq 3 \Gamma$.

Variations on this technique, the grey-molasses and Λ grey-molasses schemes achieve a further reduction in temperatures by reducing the photons scattered by the slowest-

moving atoms via coherent population trapping (CPT) of hyperfine-structure sublevels into velocity-selective dark states. The heavier ^{85}Rb atom can reach colder final temperatures via the MOT and molasses cooling techniques and will be discussed in chapter 5.

The additional cooling step after the 3D-MOT is essential to loading atoms more efficiently into optical traps. Typically, only atoms with temperatures $k_B T \leq 1/10^{\text{th}} V_0$ can be trapped in an optical trap of maximum depth V_0 . The optical trapping schemes used in our experiment are discussed in section 2.3.

2.3 All-optical trapping, cooling and transport

The laser cooling techniques described in previous sections are limited by the recoil limit (the kinetic energy of a resonant photon scattered by the atom) because they involve scattering of photons. This corresponds to $\sim 0.8 \mu\text{K}$ and $\sim 0.3 \mu\text{K}$ for ^{85}Rb and ^{40}K respectively. To reach still lower temperatures, we need to trap and cool in ways that do not scatter photons. This is achieved in our experiment by the use of far off-resonant 1064 nm lasers (red detuned to the D1 and D2 transitions) to create optical-dipole traps and evaporatively cool the atoms.

The dipole potential experienced by atoms interacting with a light field takes the form: $V_{\text{dip}}(\mathbf{r}) = -\mathbf{d} \cdot \mathbf{E}(\mathbf{r}) \propto \alpha(\omega_L) |\mathbf{E}(\mathbf{r})|^2 \propto I/\delta$. By using far off-resonant lasers ($\delta \gg 0$), the photon scattering rate ($\propto 1/\delta^2$) is almost entirely suppressed and the dipole interaction ($\propto 1/\delta$) becomes the dominant effect of the atom-light interaction. The red-detuned Gaussian beams in our experiment generate a Gaussian potential where atoms are attracted to regions of higher optical intensity. We will briefly describe the experimental procedures that bring atoms from a MOT in the 3D-MOT chamber to 3D lattices in the science chamber. For complete details, refer D. Cotta's thesis [22].

2.3.1 Crossed optical-dipole trap (CODT) and evaporative cooling

On fully loading the 3D-MOT (1.2×10^8 atoms of ^{40}K 8 s), the cloud is compressed by increasing the B-field gradient. We then turn off the magnetic-field and blue-detune

the polarizer and repumper beams by $\sim 12\Gamma$ for 10 ms of grey-molasses cooling. The additional compression and cooling enables us to load an optical dipole trap formed by a pair of 100 W lasers of waist $300\ \mu\text{m}$ crossed at 17° (referred to as the 17°CODT). Where a single beam would trap atoms radially but allow them to move freely along its axis, the crossed beam configuration traps atoms in all axes. The efficiency of loading into the 17°CODT is directly dependent on how cold the atoms are after the Λ grey-molasses stage.

What follows is a key element of ultracold atomic experiments - evaporative cooling. The technique cools a thermal sample by targeting the removal of the hottest atoms in the thermal distribution. The remaining atoms are allowed to thermalize and find a new (lower) temperature. Evaporative cooling via optical traps is straightforward: we lower the depths of the trap, allowing the hottest atoms to escape. Trap intensities are lowered via slow (of the order of seconds) exponential ramps allowing the cooler atoms time to thermalize.

2.3.2 Transporting atoms to the science chamber

We use this evaporation stage to both cool the atoms as well as load them into a tightly focused optical trapping beam referred to as the transport trap. The transport trap passes through both the 3D-MOT chamber and the science chamber and it is loaded with the focus of the beam centred on the 17°CODT . Atoms are un-polarized (mixed m_F states) during evaporation to maximize the collision rate and hence the rate of thermalization. Once they are loaded into the transport trap, we optically pump them into the $F = |9/2, -9/2\rangle$ state to minimize collisions in preparation for transport.

Using a focusing beam allows trapping in all 3-axes, including along the axis of the beam. The atoms are attracted to regions of higher optical intensity and hence follow the focus of the trapping beam. We are able to change the beam path with a configurable translation stage and hence move the focus of the beam along its axis from the 3D-MOT chamber to the science chamber, allowing us to move atoms from one chamber to another without scattering photons.

2.3.3 Optical lattice potentials

In the science chamber, atoms are trapped by a crossed optical trap with 14 W beams of waist $\sim 69 \mu\text{m}$ crossed at 90° in the horizontal plane. An RF pulse prepares atoms in a mixture of states $F = |9/2, -9/2\rangle$ and $F = |9/2, -7/2\rangle$ in preparation for two additional evaporative cooling stages where inter-state collisions are essential for thermalization. We achieve our coldest temperatures ($\sim 5 \text{ nK}$) via evaporation, reaching as low as $T = 0.18T_F$ where T_F is the Fermi temperature. Atoms are then loaded into a vertical lattice created by retroreflecting a laser from the bottom window of the chamber. Such a retro-reflection creates a standing wave pattern with a node fixed on the reflecting surface. The potential the atoms experience is of the form $V = V_0 \sin^2(k_L x)$ where $k_L = 2\pi/\lambda$ is the wavenumber of the light. Finally, once the 90°CODT beams are off, we turn flip-mirrors to retro-reflect the horizontal dipole beams and ramp them back up to load a full 3D optical lattice.

2.3.4 Selective preparation in a lattice anti-node

The final preparatory step involves a position dependent microwave transition to empty all but one anti-node of the vertical lattice, resulting in a 2D ‘layer’ of atoms in the horizontal plane [81, 110]. A vertical magnetic field gradient of $\delta_z B = 7.27 \text{ mG } \mu\text{m}^{-1}$ is generated by a pair of coils with counter-propagating currents, with a field strength of $B_0 = 11.6 \text{ G}$ at the position of the atoms. Additional shim coils allow us to shift the position of the field minimum in the horizontal plane. As described in the previous section, atoms at this stage are prepared in a mixture of states $|F, m_F\rangle = |9/2, -9/2\rangle$ and $|9/2, -7/2\rangle$. We aim to transfer atoms in a selected layer from the $F = 9/2$ to the $7/2$ manifold via microwave transitions from $|9/2, -9/2\rangle$ ($|9/2, -7/2\rangle$) to $|7/2, -7/2\rangle$ ($|7/2, -5/2\rangle$). B_0 causes a Zeeman-shift between the two transitions of $2\pi \times 7 \text{ MHz}$ while $\delta_z B$ causes a spatially-dependent frequency shift $\Delta_1 = 2\pi \times 9.68 \text{ kHz}$ ($\Delta_2 = 2\pi \times 7.37 \text{ kHz}$) between adjacent lattice layers. A large fraction ($\sim 98\%$) of the selected layer of atoms can be transferred to the $F = 7/2$ hyperfine state via adiabatic passage, with two 10 ms microwave pulses sweeping linearly in frequency across the central frequency of the selected layer (with a sweep width $< \Delta_i$) and peaking in intensity at the centre

Chapter 2. Building a quantum simulator

frequency. Following this, a D2-resonant removal pulse on the $F = 9/2 \rightarrow F' = 11/2$ cycling transition heats out all atoms in the lattice outside of the selected layer prepared in the $F = 7/2$ manifold. The same microwave pulses are then applied to return the remaining layer of atoms into the $F = 9/2$ state prior to Hubbard evolution and imaging.

We have shown in chapter 1 why we want to study Hubbard physics and how cold atoms in an optical lattice are well suited for this purpose. In chapter 2, we discussed briefly the experimental procedures necessary to implement such a quantum simulator. In the remainder of this thesis, we will discuss our experimental and theoretical approaches to improve the imaging of ^{40}K atoms.

Chapter 3

Sideband Cooling

Once the ^{40}K atoms are prepared in an anti-node of the 3D optical lattice, what follows is their coherent evolution according to the Hubbard Hamiltonian. In this coherent evolution period, the combination of optical and magnetic potentials and the filling fraction of atoms in the lattice determine the dynamics of the system. The final step is to image the resulting atom distribution. The intensity of lattice beams are quickly ramped up, preventing further evolution of the system. We aim to image atoms in these deep lattice potentials with high fidelities. This chapter describes the imaging scheme to generate the necessary fluorescence from individual atoms such that we can re-construct the atom distribution in the lattice.

Fluorescence imaging of single atoms requires the scattering of a large number of photons ($\sim 1 \times 10^4$) per atom. It is essential that the atoms are simultaneously cooled to prevent inter-site tunneling or atom losses in the process. The cooling scheme common for bosonic alkali atoms is the red-detuned optical molasses [79, 81]. However, for fermionic ^{40}K closely spaced excited hyperfine levels make molasses cooling inefficient. Furthermore, m_F levels of the excited state begin to mix in deep optical traps owing to tensor light shifts, making it a poor choice for cooling in the deep optical traps used for imaging. We rely instead on sideband cooling techniques [111], i.e. driving atomic transitions tuned to simultaneously couple lower energy motional states (as shown in figure 3.1). This can be seen as analogous to optically pumping to the $n = 0$ motional state in a harmonic potential [112].

Sideband cooling was historically feasible only for heavier ions such as Hg^+ [113] and Ba^+ [114]. For a trapping frequency of ω_T , we require atoms with accessible narrow-linewidth ($\Gamma \ll \omega_T$) optical transitions between states such that sidebands can be resolved from the carrier. Raman sideband cooling (RSC) [115] and more recently electromagnetically induced transparency (EIT) cooling [116] extend these principles to lighter ions [117, 118] and neutral atoms [119, 120]. Raman cooling uses narrow optical transitions between metastable states whereas EIT cooling leverages an asymmetric (Fano-like) resonance to preferentially drive sideband transitions between ground and excited state.

The focus of this chapter is the RSC technique applied to neutral atoms in a 3D optical lattice. We will explore in detail the cooling scheme, implementation and optimisation of RSC for fluorescence imaging of single atoms. In the final section, we will compare RSC results against the EIT technique which was previously employed in this experiment and the motivation behind shifting to RSC-based imaging. The implementation of EIT cooling is described in detail in sections 3.3 and 3.4 of D. Cotta's thesis [22].

3.1 Raman cooling scheme

The RSC scheme relies on a two-photon dipole forbidden transition between hyperfine levels of the ground state mediated by the presence of an excited state (figure 3.1). As the transition has a narrow linewidth, the relative detuning between the Raman beams can be tuned to access different motional sidebands without driving the carrier transition. The technique has been used in several quantum gas microscope experiments [121–124], for deterministic preparation of single atoms in microscopic dipole traps (optical tweezers) in their motional ground state [125, 126], achieving ^{87}Rb Bose-Einstein condensation without direct evaporation [127] among others.

We have implemented the cooling scheme as follows (see figure 3.1): a far off-resonant (~ 30 GHz detuned from the D2 transition) laser drives two-photon transitions from $|F, m_F\rangle = |9/2, -9/2\rangle$ to $|7/2, -7/2\rangle$ of the $4S_{1/2}$ ground state (henceforth referred

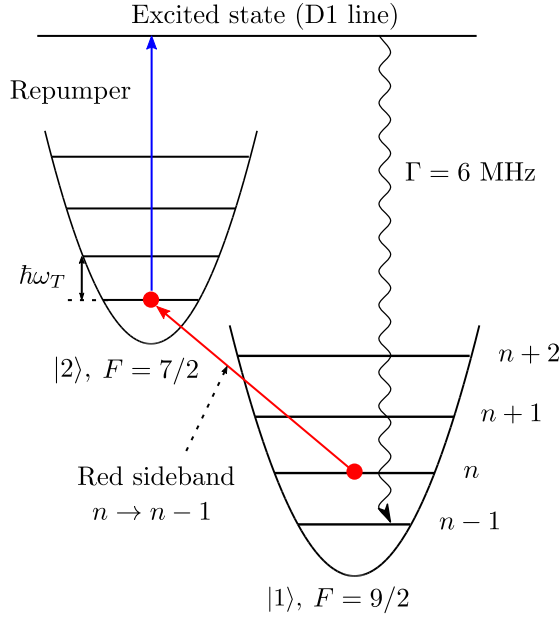


Figure 3.1: Three-step Raman cooling cycle: 1. two-photon sideband transition $|n\rangle \rightarrow |n-1\rangle$ (red line), 2. transition to excited state (blue line) and 3. decay to ground state preserving motional level $n-1$ (black line). See figure 3.5 to see the internal levels and laser transitions used in our experiment to implement this scheme.

to as $|1\rangle$ and $|2\rangle$ respectively). For a lattice trapping frequency of ω_T , the two-photon transition is red-detuned from resonance frequency by ω_T to couple $|1, n\rangle \rightarrow |2, n-1\rangle$, where n is the atom's motional energy state in the lattice (see Appendix A). This is referred to as the red-sideband transition. A repumping laser near resonant to the D1 line depopulates the $F = 7/2$ manifold allowing the atoms to spontaneously decay back into $|1\rangle$ driving $|2, n-1\rangle \rightarrow |1, n-1\rangle$ via the $4P_{1/2}$ excited state. When trap depths are sufficient to preserve the atom's n state after a photon scattering event, the system is said to be in the Lamb-Dicke regime [128].

This process repeats, with each cycle lowering the n level and reducing the atom's vibrational energy by $\hbar\omega_T$ per cycle. The first step of the cycle (red-sideband transition) drives transitions at rates of $\sim 2\pi \times 50$ kHz, and is typically the slowest part of the cycle.

3.1.1 Transition strengths

The effective Hamiltonian for the RSC scheme describes a λ system in the rotating frame (following chapter 6 of [129]) after adiabatic elimination of the fast oscillating excited state:

$$H_R = \frac{p^2}{2m} + \hbar(\Delta_1 + \omega_{AC1}) |g_1\rangle \langle g_1| + \hbar(\Delta_2 + \omega_{AC2}) |g_2\rangle \langle g_2| + \frac{\hbar\Omega_R}{2} \left(\sigma_R e^{i(\vec{k}_2 - \vec{k}_1) \cdot \vec{r}} + c.c \right) \quad (3.1)$$

The second and third terms describe the energy separation of the ground states $|g_1\rangle, |g_2\rangle$ from the excited state energy. Δ_1, Δ_2 correspond to the single-photon detuning from $|g_i\rangle \rightarrow |e\rangle$, $\omega_{ACi} = \Omega_i^2/4\Delta_i$ are the AC stark shifts of the ground states. The last term is the two-photon coupling between ground states, i.e. $\sigma_R = |g_2\rangle \langle g_1|$. Importantly,

$$\Omega_R = \frac{\Omega_1\Omega_2}{2\Delta}, \quad (3.2)$$

where Ω_i are the single photon coupling strengths between $|g_i\rangle \rightarrow |e\rangle$ and $\Delta = (\Delta_1 + \Delta_2)/2$. The transition results in a momentum kick operator of the form $e^{i\vec{k} \cdot \vec{r}}$. This provides the necessary change in momentum to couple motional levels in harmonic traps, which we will address more closely in this section.

A single site of a 3D lattice potential can to first order be treated as a 3D harmonic trap (see appendix A). In such a case the atom has equally spaced motional energy levels in each axis - $\vec{n} = [n_x, n_y, n_z]$, where the total motional energy of the system is $E_p = \sum_{\mu}^{x,y,z} (n_{\mu} + 1/2) \hbar\omega_{T\mu}$. The matrix element for the resulting two-photon transition including motional degrees of freedom is:

$$\begin{aligned} \langle g_2, \vec{n}_2 | H_R | g_1, \vec{n}_1 \rangle &= \langle g_2, \vec{n}_2 | \frac{\hbar\Omega_R}{2} \sigma_R e^{i\Delta\vec{k} \cdot \vec{r}} | g_1, \vec{n}_1 \rangle + c.c \\ &= \frac{\hbar\Omega_R}{2} \langle g_2 | \sigma_R | g_1 \rangle \langle \vec{n}_2 | e^{i\Delta\vec{k} \cdot \vec{r}} | \vec{n}_1 \rangle + c.c, \end{aligned} \quad (3.3)$$

where $\Delta\vec{k} = \vec{k}_2 - \vec{k}_1 = [k_x, k_y, k_z]$, and k_{μ} are the components of $\Delta\vec{k}$ along the axis μ . After Taylor-expanding the exponential in equation 3.3, the motional component of

the inner product is:

$$\langle \vec{n}_2 | e^{i\Delta\vec{k}\cdot\vec{r}} | \vec{n}_1 \rangle = \langle \vec{n}_2 | \left(1 + i\Delta\vec{k}\cdot\vec{r} - \frac{(\Delta\vec{k}\cdot\vec{r})^2}{2!} + \dots \right) | \vec{n}_1 \rangle. \quad (3.4)$$

We can substitute $\Delta\vec{k}\cdot\vec{r} = k_x\bar{x} + k_y\bar{y} + k_z\bar{z}$ where $\bar{\mu}$ are unit vectors in the μ axis. In a harmonic trap, this takes the operator form, $\bar{\mu} = \mu_0(\hat{a}_\mu + \hat{a}_\mu^\dagger)$ where $\hat{a}_\mu, \hat{a}_\mu^\dagger$ are harmonic oscillator creation and annihilation operators and $\mu_0 = \sqrt{\hbar/2m\omega_{T\mu}}$, the characteristic length scale of the trap. Of interest to us are the first and second terms of the Taylor expansion which act independently in each axis. To better understand these two terms, we apply them in 1D, i.e. $\vec{r} = \bar{x}$ and $\vec{n}_i = n_i(x) = n_i$. We then have:

$$\langle n_2 | e^{ik_x\bar{x}} | n_1 \rangle \simeq \langle n_2 | 1 + ik_x x_0 (a + a^\dagger) | n_1 \rangle \quad (3.5)$$

This shows we observe three possible transitions: the carrier ($n_2 = n_1$), red sideband ($n_2 = n_1 - 1$) and the blue sideband ($n_2 = n_1 + 1$) with relative strengths 1, $k_x x_0 \sqrt{n_1}$ and $k_x x_0 \sqrt{n_1 + 1}$ respectively. The third term in equation 3.4, $(\Delta\vec{k}\cdot\vec{r})^2/2$, is typically an order of magnitude weaker, allowing for second-order sideband transitions (of the form $n_2 = n_1 \pm 2$) in each axis as well as coupling motional levels between the three axes. The Rabi frequency for red-sideband (cooling) transitions in the x axis is therefore

$$\Omega_{RSB} = \eta_x \sqrt{n_1} \Omega_R, \quad (3.6)$$

where the quantity $\eta_x = k_x x_0$ is the Lamb-Dicke parameter [128] in the x axis for the two-photon transition. A similar treatment can be applied to find the red-sideband Rabi frequency in the y and z axes. In appendix B, we detail the Lamb-Dicke parameter in each lattice axis and the Rabi frequency for the blue-sideband transition, Ω_{BSB} .

The implementation of this scheme and associated limitations are discussed in the following sections.

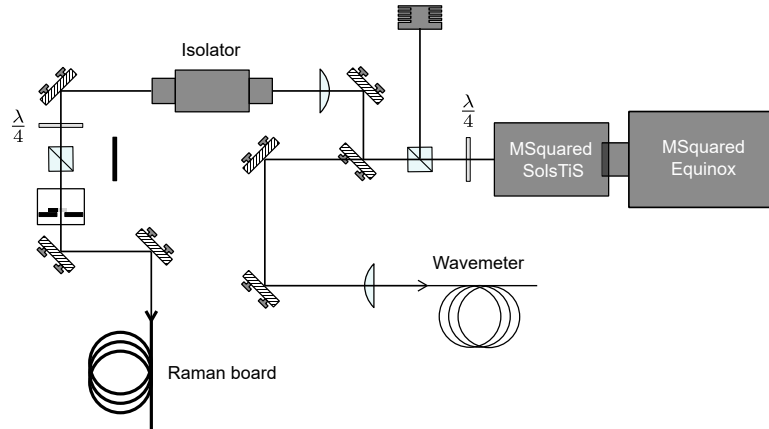


Figure 3.2: MSquared laser optics setup: ~ 1.5 W light at 766.7 nm is generated by a Ti-sapphire laser. This is coupled through a 10 m high power fibre to the Raman laser optics board. A wavemeter is used to fine-tune the laser frequency and monitor its stability.

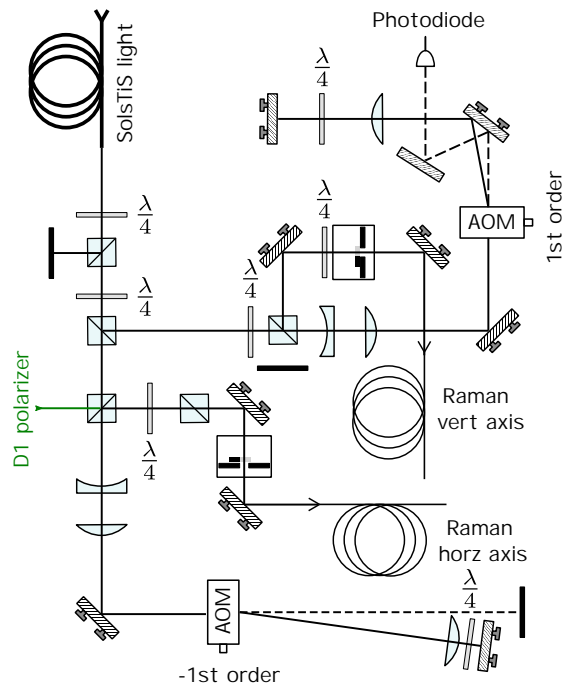


Figure 3.3: Raman laser optics setup: 766.7 nm Raman light is split into two paths (horizontal and vertical axis beams) with double pass AOMs of opposite order so as to achieve a frequency separation of $4\Delta_{\text{AOM}}$, where $\Delta_{\text{AOM}} = \Delta_{\text{HFS}}/4 + \delta_{2\text{photon}}/4$. D1 resonant polariser (770 nm) is overlapped with the horizontal axis Raman beam.

3.2 Implementation and characterization

To simplify the nomenclature of these beams, we utilize our abbreviations for the $4S_{1/2}$ hyperfine states; $|F, m_F\rangle = |9/2, -9/2\rangle = |1\rangle$ and $|F, m_F\rangle = |7/2, -7/2\rangle = |2\rangle$. The excited states $4P_{3/2}$ and $4P_{1/2}$ are referred to as $|3\rangle$ and $|4\rangle$ respectively. Under this scheme, the Raman beams are denoted as R_i referring to the beam targeting the $|i\rangle \rightarrow 4P_{3/2}$ transition (D2 line). Similarly, the optical pumping lasers are referred to as P_i near resonant to the $|i\rangle \rightarrow 4P_{1/2}$ transition (D1 line). We couple 8 W of 532 nm light from an MSquared Equinox pump laser to an MSquared SolsTiS [130] ($< 2\pi \times 50$ kHz linewidth Ti:Sapphire laser) to generate 1.5 W of 766.7 nm light (see figure 3.2) 40 GHz detuned from the D2 resonance of ^{40}K . This is fibre coupled to the Raman laser optics setup (see figure 3.3) where a polarizing beam splitter cube splits the beam into the R_1 and R_2 beam paths. Double-pass acousto-optic-modulators (AOMs) in each path are driven by a tunable frequency generator. For a driving frequency Δ_{AOM} , the net frequency separation between the Raman beams is $4\Delta_{\text{AOM}} = \delta_{2\text{photon}} + \Delta_{\text{HFS}}$ where $\Delta_{\text{HFS}} = 1.286$ GHz, the hyperfine splitting of the $4S_{1/2}$ state. Furthermore, we use a PID controller to regulate the intensities of the Raman beams for reproducibility and stability.

The frequency reference for both 770 nm beams is a moglabs tunable cat-eye laser (CEL) [131] fitted with an Eagleyard EYP-RWE-0790 diode [132]. A pickoff from this laser is used to generate a saturated absorption spectroscopy signal to lock the laser 80 MHz blue to the ^{39}K D1 line. The remainder of the setup is described in section 2.2.2 of D. Cotta's thesis [22]. Two secondary MOGLabs extended cavity diode lasers (ECDL) are offset locked to the frequency reference via beat signals on fast photodiodes. These beat signals are amplified and input to a frequency-to-voltage (F-V) converter that generates a slope of 50 MHz V^{-1} for the polarizing laser (P_1) and 100 MHz V^{-1} for the repumping laser (P_2). An external voltage from the control computer shifts the zero-crossing of the input error signal to the PID regulators. This is used to tune the secondary laser frequency offsets from the primary laser in a range (100,900) MHz and (100, 1700) MHz respectively for the beams P_1 and P_2 .

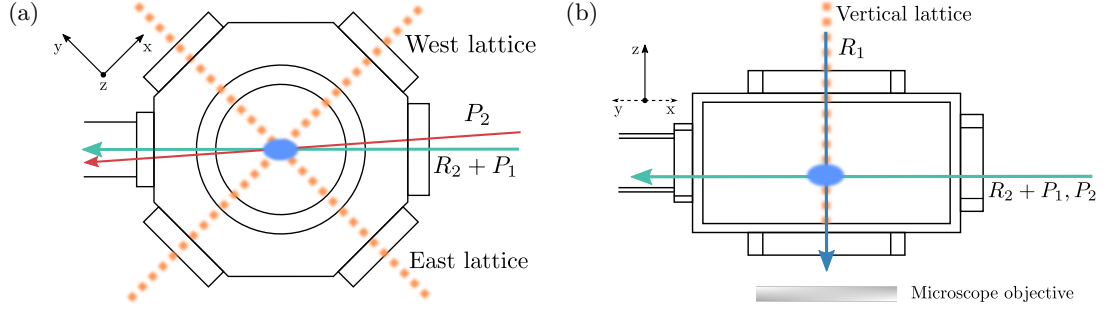


Figure 3.4: Beam orientations: Alignment of the lattice and Raman cooling beams to atoms in the science chamber: (a) Top view. (b) Side cross-section.

3.2.1 Beam orientations

To ensure that the net k-vector of the Raman beams have a component in each of the lattice axes, the vertical Raman beam R_1 is aligned parallel to the vertical lattice axis and the horizontal Raman beam R_2 bisects both the horizontal axes while being perpendicular to the vertical axis (see figure 3.4). The horizontal Raman beam is circularly polarised via a $\lambda/4$ waveplate while the vertical Raman beam is linearly polarised. Therefore in sufficiently strong guiding field we couple the $|9/2, -9/2\rangle \rightarrow |7/2, -7/2\rangle$ states via the Raman process. Implementation of the Raman cooling scheme requires additional lasers on the D1 line ($4S_{1/2} \rightarrow 4P_{1/2}$), referred to as the polariser beam P_1 ($F = 9/2 \rightarrow F' = 9/2$) and the repumping beam P_2 ($F = 7/2 \rightarrow F' = 9/2$). The relevant level diagrams are shown in figure 3.5b. The polarizing beam P_1 is overlapped with the horizontal R_2 on the laser table itself (see figure 3.3) and serves to maintain the polarisation of the sample during imaging. The more critical re-pumping beam P_2 that generates fluorescence necessary for imaging is aligned at a small angle to the horizontal axis on the experiment table such that an independent power regulation can be set up for the R_2 and P_2 beams respectively. Figure 3.4 shows the beam alignments.

3.2.2 Transition spectra

We measure the Raman spectra by preparing atoms in state $|F, m_F\rangle = |9/2, -9/2\rangle$ followed by a 10 ms Raman probe pulse. This transfers a fraction of atoms into the

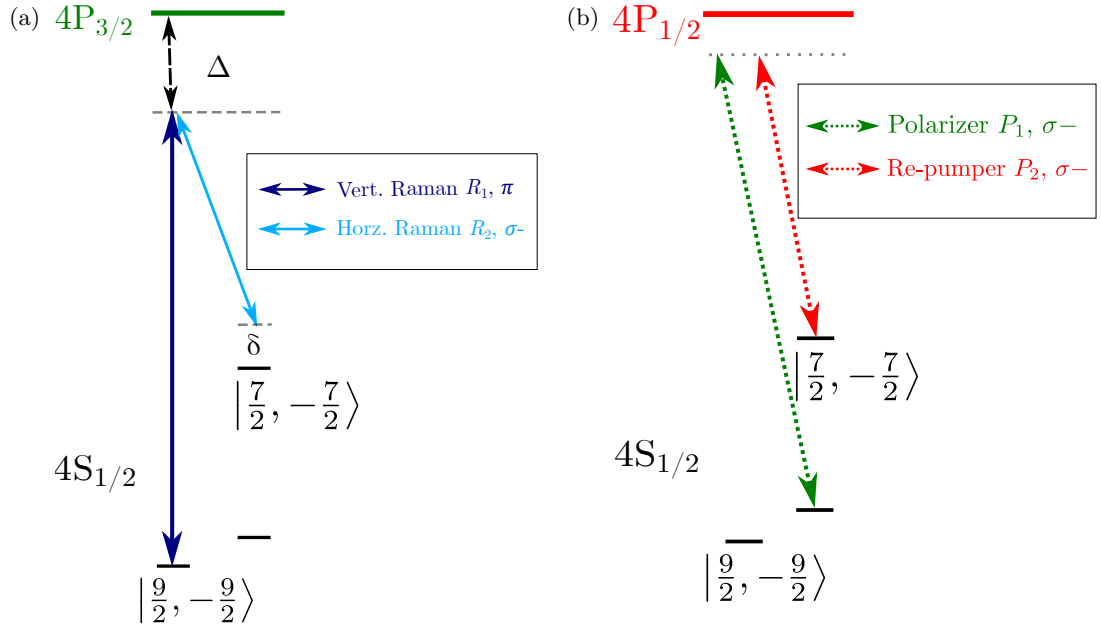


Figure 3.5: Level diagrams: D2 (a) and D1 line (b) beams used during Raman imaging. The pumping beams (b) maintain the polarization of the atom and generate the necessary fluorescence for imaging.

$|F, m_F\rangle = |7/2, -7/2\rangle$ state. We then heat out atoms in the $F = 9/2$ manifold with a resonant D2 pulse before imaging the atoms transferred by the Raman pulse into the $|F, m_F\rangle = |7/2, -7/2\rangle$ state. The beam intensities for the Raman probe pulse are low enough to maintain $\Omega_R \ll \omega_T$. We observe three different transitions (see figure 3.6a):

- The carrier ($|n\rangle \rightarrow |n\rangle$), at $\delta = \delta_{hfs}$ where δ_{hfs} is the separation between the $|9/2, -9/2\rangle \rightarrow |7/2, -7/2\rangle$ states including Zeeman effects as well as tensor light shifts in deep lattices (~ 0 for $B = 0$).
- The red-sideband ($|n\rangle \rightarrow |n - 1\rangle$) situated ω_T red detuned off the carrier (where ω_T is the trapping frequency in the lattice) which corresponds to a loss of one motional quanta per RSC cycle.
- The blue sideband ($|n\rangle \rightarrow |n + 1\rangle$), situated ω_T blue detuned off the carrier corresponding to an increase in the motional quanta of the system.

The sideband frequencies for each lattice are independent of one another. i.e. by changing the trap depth in one of the three lattice axes, we can observe two additional

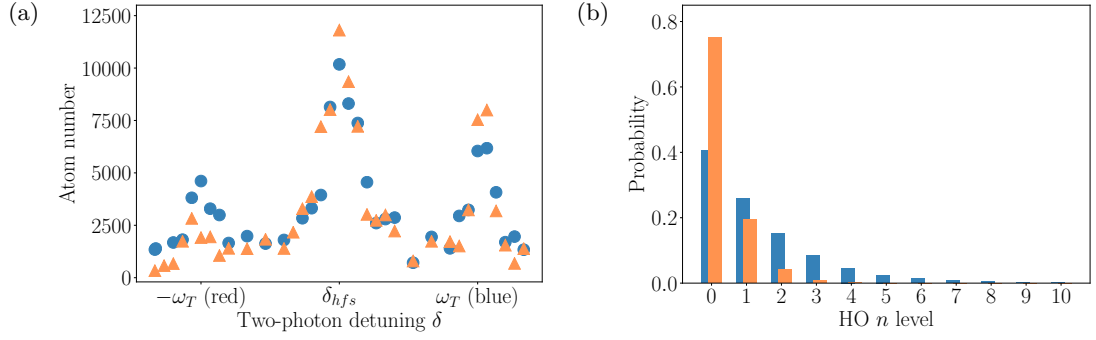


Figure 3.6: (a) Raman spectra and (b) n -level distribution in a deep 3D lattice ($\omega_T = 2\pi \times 330$ kHz): Measuring number of atoms transferred to the $F = 7/2$ manifold vs the two-photon detuning δ of the Raman beams (blue circles in (a)) and corresponding n distribution (blue bars in (b)). The measurement is repeated with pre-cooling the atoms (orange triangles in (a)) with the corresponding n distribution in orange bars in (b).

peaks corresponding to the trap frequencies of that lattice axis. Since the red-sideband coupling strength $\Omega_{\text{red}} \propto \sqrt{n}$, the $n = 0$ motional state is dark to the red-sideband transition. This can be observed as an imbalance in the red/blue spectra which is enhanced after cooling the sample (i.e. preparing a larger fraction of atoms in the $n = 0$ state). In figure 3.6a we show the Raman spectra both before cooling and after reaching an equilibrium state at typical imaging parameters (table 3.2 on page 42). The ideal imaging parameters are not equal to the best cooling parameters, as the latter preserves all atoms in the $n = 0$ dark state.

The probability of atoms in the lowest n motional state ($n = 0$) can be approximated from the Raman spectra as

$$P(0)_{\text{measured}} = 1 - \frac{N_R}{N_B}. \quad (3.7)$$

N_R and N_B are the number of atoms resonant to the red-sideband and blue-sideband transitions respectively. The approximation is improved by detuning two lattices and measuring red/blue atom number ratios independently in each axis. From figure 3.6a we find $P(0)_{\text{measured}} = 0.4$ before cooling and $P(0)'_{\text{measured}} = 0.76$ after 2 s of Raman cooling.

Equation 3.7 gives us information only regarding the population fraction in the

Chapter 3. Sideband Cooling

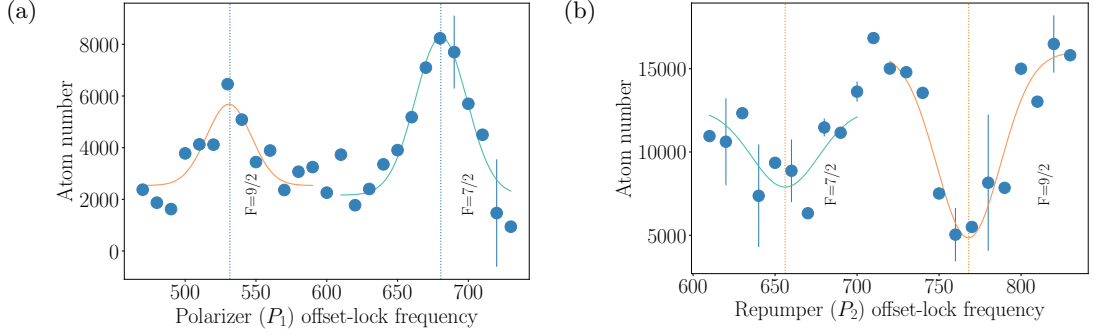


Figure 3.7: Polarizer and repumper transitions ((a) and (b) respectively) in a deep 3D lattice ($\omega_T = 2\pi \times 280$ kHz): Scanning the offset frequency of P_1 and P_2 from the master laser provides a spectra with peaks separated by the hyperfine splitting of the $4P_{1/2}$ state.

$n = 0$ state, to recover the population distribution in all n levels, we consider the Fermi-Dirac distribution: $\bar{n}_i = 1/(e^{(\epsilon_i - \mu)/k_B T} + 1)$, where \bar{n}_i is the average distribution in state i , ϵ_i is the energy of state \bar{n}_i and μ the total chemical potential. For deep lattices we can neglect μ as $\epsilon_i \gg \mu$. Therefore, we can calculate

$$P(0)_{\text{fermi}} = \frac{1/(\beta\epsilon_0 + 1)}{\sum_i 1/(\beta\epsilon_i + 1)}, \quad (3.8)$$

where $\beta = 1/k_B T$, ϵ_i is the energy of motional level n_i . The steady state temperature measured after 1 s of Raman cooling is measured to be $9.8 \mu\text{K}$. Calculating $P(0)_{\text{fermi}}$ at this temperature gives us a population fraction of 0.745 which agrees well against $P(0)_{\text{measured}}$. We can therefore estimate temperature and n level distribution for the atoms corresponding to the red/blue sideband imbalance (figure 3.6b).

The lasers near-resonant to the D1 line show transitions separated by ~ 150 MHz, the hyperfine splitting of the $4P_{1/2}$ state (see figure 3.7). Similar to the Raman spectra, the D1 polarizer spectrum is measured by imaging the atoms in the $F = 7/2$ state after a short P_1 pulse that transfers atoms from the $F = 9/2$ to $F = 7/2$ manifold. For the repumper spectra, atoms are first shelved in the $F = 7/2$ manifold via an adiabatic transfer MW pulse, followed by a short P_2 pulse and imaging the atoms returned by P_2 to the $F = 9/2$ manifold.

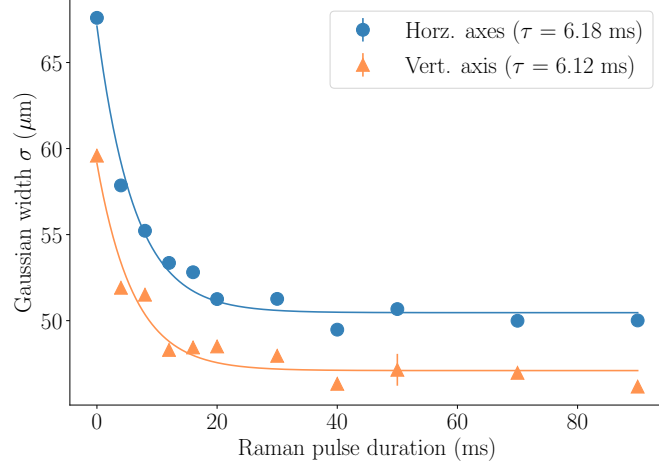


Figure 3.8: Width of ^{40}K atom cloud as a function of Raman pulse duration in a deep lattice ($\omega_T = 2\pi \times 300 \text{ kHz}$), optimal cooling parameters.

3.2.3 Raman cooling and imaging

The conditions that must be satisfied for efficient cooling are (appendix A of [115]):

1. $\eta_{D1}^2 \ll 1$: The probability of raising n level via D1 photon absorption and spontaneous scattering is low. i.e. the system is in the Lamb-Dicke regime.
2. $\Delta_i \gg \pi\Gamma/2\eta_{D2}\sqrt{n}$: Raman beams drive very few single-photon transitions compared to two-photon transitions.
3. $\Omega_R \ll \omega_T$: carrier transition width is less than sideband-carrier spacing.

Scanning the power and frequencies of the Raman beams and repumping beam allows us to optimise the cooling rate (see figure 3.8) with atom lifetimes $\sim 30\text{s}$. As maximally efficient cooling would trap atoms in a dark state, we need to optimise simultaneously to achieve long lifetime and to generate a high enough for the fluorescence signal to reconstruct the atom distribution. We will find in later sections that condition 3 for efficient cooling is relaxed to $\Omega_R \leq 2\omega_T$ when optimising for fluorescence (section 3.3.4) at our trap frequencies, i.e., we do not image with sideband resolved (figure 3.6a) parameters.

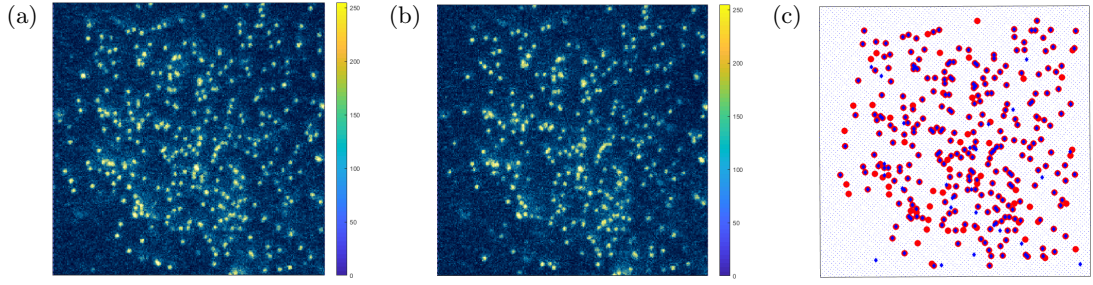


Figure 3.9: Tunneling/Losses: (a) First image of sample taken via 1000 ms exposure to Raman pulse in $2\pi \times 300$ kHz trap. (b) Second image on the same sample taken after 500 ms hold time. (c) From the images we construct a 2D matrix of occupied and unoccupied lattice sites. Comparing occupied sites in the first picture (red circles) and second picture (blue diamonds) allows us to calculate atom loss and hopping rates.

The typical procedure for imaging is as follows: First, the lattices depths are raised to have trap frequencies $\omega_T \sim 2\pi \times 300$ kHz such that atoms cannot tunnel to neighbouring lattice sites (i.e. $J \sim 0$) and the atom distribution remains fixed during imaging. Atoms are then exposed to the imaging pulse consisting of R_2 , P_1 , P_2 along the horizontal axis and R_1 along the vertical axis for 1000 ms. A high numerical aperture camera captures $\sim 12\%$ of the resulting isotropic fluorescence. Narrow linewidth filters ensure only D1 photons reach the camera such that it is not blinded by the vertical Raman beam R_1 . This process is repeated once more without atoms to provide an image of the background which is then subtracted from the original image. A full understanding of inter-site hopping and atom losses during imaging requires that two successive images are taken on the same sample (see figure 3.9) before the final background image. Occupation matrices (a binary map of occupied and unoccupied sites) are generated via Lucy-Richardson deconvolution [133] for both images. Atoms that are imaged in the first picture while not being present in the second picture are considered loss events. We mark as tunnelling events those atoms that appear in the second image in previously unoccupied sites.

3.3 Raman imaging optimisation and constraints

We measure that fluorescence per atom as well as percentage of losses and hopping events scale linearly with image exposure duration. i.e. for otherwise constant imaging parameters, a fluorescence image with 1000 ms exposure-time will have twice the fluorescence per atom as well as twice the loss and hopping events as a 500 ms exposure-time image.

This gives us the opportunity to calculate a quantity independent of exposure duration referred to as the fluorescence counts per loss percentage - CPL:

$$\text{CPL} = \frac{N_F}{P_L}. \quad (3.9)$$

N_F is the average number of fluorescence photons detected for each atom, P_L is the percentage of atoms lost during imaging. This parameter simplifies the optimising of imaging for two reasons. First, it is a single figure of merit that comprises of multiple aspects of Raman imaging. Secondly, it is a quantity independent of exposure duration, hence allows us to temporarily use longer exposure duration to get higher contrast in loss rates during optimisation. As an example, it is easier to differentiate 12% loss against 18% loss at 1500 ms exposure as compared to differentiating 4% loss and 6% loss at 500 ms exposure. We will compare the CPL values for Raman and EIT imaging in the final section of this chapter.

The imaging efficiency depends on the frequency and intensity of four D2 and D1-resonant beams and the trapping frequency of 1064 nm lattice beams. While optimizing on these parameters there are two additional considerations we keep in mind. First, when we reduce imaging duration to reduce loss rates in the image, the signal to noise ratio must remain sufficient for single atom detection. Secondly, we need to ensure that our final parameter configurations do not induce a non-linear loss mechanism. In the remainder of this section we discuss the experimental constraints of our imaging scheme and which of these limitations can be mitigated.

3.3.1 Inverted excited state

As will be studied in chapter 4, the excited $4P$ states of ^{40}K experience an anti-trapping potential six times greater than the trapping of the $4S$ ground state in an optical potential created by 1064 nm wavelength light. This presents as an additional heating mechanism. As an extreme example, if near resonant light couples the $4S$ and $4P$ states such that the lower dressed state is a 6:1 admixture of $4S$ and $4P$ character, this dressed state would be un-trapped and insensitive to the lattice potential, leading to atom loss. During imaging, the small fraction of time atoms spend in the anti-trapped state leads to rapid heating and broadening of the atomic wavefunction. This heating mechanism is discussed in more detail in chapter 4, and we will find that deeper traps ($\omega_T > 2\pi \times 300 \text{ kHz}$) increase the heating and tunneling rates owing to the anti-trapped excited state.

3.3.2 Trap inhomogeneity

RSC involves a two-photon narrow-linewidth transition. Additionally, the carrier transition (Ω_R) power broadens faster than the red-sideband transition ($\eta_R \Omega_R$) when $\eta_R \ll 1$ and limits the effective width of the red-sideband transition to a few tens of kHz. This makes the RSC scheme more sensitive to inhomogeneities on the order of kHz. Such inhomogeneities could present as spatial fluorescence signal variations or spatial variation in atom losses leading to errors in reconstructing the atom distribution. Hence, inhomogeneities that affect the $|1\rangle \rightarrow |2\rangle$ transition (section 3.3.2) are relevant to our image quality. Moreover, since we aim to drive sideband transitions $|1, n\rangle \rightarrow |2, n-1\rangle$ we are sensitive to variations of the spacing of harmonic oscillator levels in the trap (section 3.3.2).

Inhomogeneities affecting the carrier transition

The energy difference between the $|1\rangle$ and $|2\rangle$ levels can vary due to light shifts or due to magnetic field gradients parallel to the 2D sheet of atoms. Since the $|1\rangle$ and $|2\rangle$ are light shifted slightly differently, the energy spacing between them varies from the centre

of the trap to the edges owing to the Gaussian shape of the lattice beams. Over our $50\ \mu\text{m}$ field of view, we estimate this to vary by at most $2\pi \times 6.6\ \text{kHz}$ for a deep lattice of $\omega_T = 2\pi \times 330\ \text{kHz}$. The variation owing to differential Zeeman-shift between the two levels is $2\pi \times 4.6\ \text{kHz}$, corresponding to a $1.85\ \text{mG}$ magnetic field variation over the field of view due to an estimated $0.37\ \text{G cm}^{-1}$ gradient at the trap centre. We can thus expect carrier resonance inhomogeneities to be an order of magnitude smaller than the RSC Rabi frequency.

Inhomogeneities affecting the sideband transition

The above shifts convolve to broaden both the carrier and sideband spectra. However, inhomogeneities in the harmonic oscillator frequency ω_T affect only the sideband spectrum. We find these inhomogeneities play a larger role in the efficiency of RSC.

The radial intensity profile of a Gaussian beam is of the form $I(r) = I_0 e^{-2r^2/w^2}$, where w is the $1/e^2$ width of the beam. Therefore our Gaussian lattice beams would cause a radial trap frequency variation $\omega_T(r) \propto \sqrt{I} = \omega_0 e^{-r^2/w^2}$. Each lattice axis must be considered separately as the trap frequency variation in one axis does not affect the other. For the tightest lattice axis of beam waist $69\ \mu\text{m}$, we expect a 12% frequency variation across the field of view. For the deepest imaging lattice of $\omega_T = 2\pi \times 330\ \text{kHz}$, this corresponds to $2\pi \times 40.6\ \text{kHz}$ variation from centre to edge. For red-sideband transition width smaller than the variation in trap frequency, not all atoms across the field of view are resonant to RSC at a particular two-photon detuning δ . Scanning δ , this inhomogeneity results in concentric rings of fluorescing atoms with the radius from centre depending on δ . To ensure that all atoms in the field of view are simultaneously resonant to RSC, we must ensure that Ω_{RSB} is greater than the radial trap frequency variation.

Finally, we consider the variation in harmonic oscillator frequency resulting from the anharmonicity of the individual potential wells, i.e. the non-uniform spacing of motional energy levels at each lattice site. We can show (appendix A) that the energy

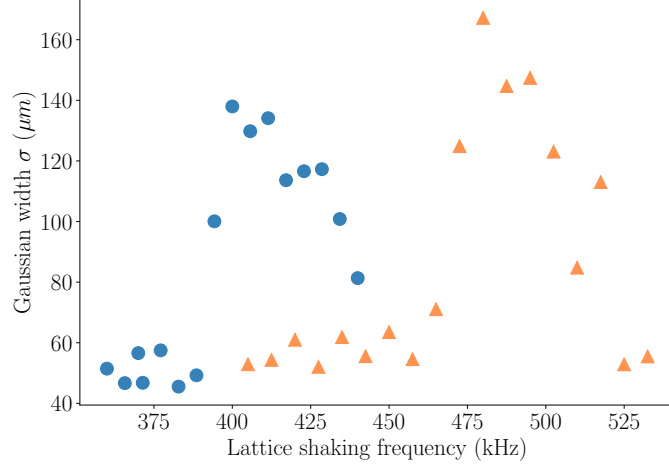


Figure 3.10: Trap frequency measurement: Modulating the lattice amplitude to drive transitions from $n \rightarrow n + 2$ motional levels in a lattice of $\omega_T = 2\pi \times 200$ kHz (blue circles) and $\omega_T = 2\pi \times 240$ kHz (orange triangles).

spacing between $n \rightarrow n - 1$ energy levels varies as

$$\Delta\epsilon_{(n \rightarrow n-1)} = \hbar\omega_T - nE_r^L. \quad (3.10)$$

Here E_r^L is the lattice recoil energy, i.e. the recoil energy corresponding to scattering a 1064 nm photon. Whereas previous sources of inhomogeneity could in part be mitigated by lower lattice depths, the anharmonicity does not depend on the lattice depth. For our system the energy spacing between successive levels and thus the spacing between the carrier and sideband transition decreases by $E_r^L = 2\pi\hbar \times 4.4$ kHz. This inhomogeneity can be observed as an asymmetry in the sideband spectra which spread towards the carrier as higher motional levels have lower spacing from the carrier. The anharmonicity can also be observed as asymmetry in trap frequency measurements (figure 3.10). To measure trap frequencies, we can excite atoms in the trap by modulating the intensity of lattice beams as $V(t) = V_0 + V_s \cos(\omega_s t)$. When $\omega_s = 2\omega_T$ atoms in the motional level n are excited from $n \rightarrow n + 2$ energy level in the trap, referred to as parametric heating. This is observed as an increase in temperature (and thus the size of the clouds) via absorption imaging. Due to the anharmonicity of the trap, the resonance

Source	Frequency broadening
Magnetic field gradient	4.6 kHz
Differential light shift	$0.02 \omega_T$
Trap frequency spread (ω_T)	$0.12 \omega_T$
Anharmonicity (n)	$4.4 \text{ kHz} \times n$

Table 3.1: Inhomogeneity sources and the resulting frequency variation: Variations in the frequency of Raman red-sideband transitions from $|9/2, -9/2\rangle \rightarrow |7/2, -7/2\rangle$ across a $50 \mu\text{m}$ diameter field of view.

frequency for the $n \rightarrow n + 2$ transition for atoms in motional level n varies as $\omega_s(n) = 2\omega_T - (2n + 3)E_r^L/\hbar$. i.e. the higher level motional states, corresponding to higher energy are accessible at lower frequencies than those of the $n = 0 \rightarrow 2$ transition.

The estimates of expected trap inhomogeneities are summarised in Table 3.1.

3.3.3 Beam inhomogeneity

As in the case of trap inhomogeneities, there is also a spatial variation of two-photon resonance δ and Rabi frequencies Ω_R across the atom cloud and along the different axes caused by the D1 and D2 resonant beams. These arise out of constraints on access to the atoms which restrict the beams to certain sizes and incident angles.

Carrier resonance inhomogeneity

Beam alignments with the atom cloud play a crucial role in imaging. For example, P_1 light-shifts the $|1\rangle$ state, while P_2 light-shifts the $|2\rangle$ state. A slight misalignment in either D1 resonant beam leads to a variation in the separation between the $|1\rangle$ and $|2\rangle$ state across the sample due to their gaussian intensity variation. Critically, the P_2 beam is aligned at a small angle from the horizontal axis to allow for independent power regulation (see figure 3.4). As a consequence, the beam is clipped by the vacuum chamber and cannot be imaged on a camera. When the beam is not well aligned, the resonant two-photon detuning δ for imaging varies across the field of view. Hence, for a particular δ we only see a narrow band of fluorescing atoms while the rest of the atom layer is dark. Scanning δ brings different parts of the layer in resonance to imaging. This enables us to measure the exact inhomogeneity gradient (kHz/ μm) across the field

of view. We can then optimize the alignment to minimize this gradient such that the entire field of view is simultaneously resonant to Raman imaging.

Carrier frequency variation

From equation 3.2 we see that $\Omega_R \propto \sqrt{I_1 I_2}$, where I_1, I_2 are the intensities of the two Raman beam. While the horizontal Raman beam width R_2 is significantly larger than the size of a 2D layer, the vertical Raman beam R_1 is of the same order of magnitude as our field of view (50 μm). The Gaussian shape of the vertical beam leads to $\sim 7\%$ variation of Raman coupling Ω_R leading to a $\sim 7\%$ variation in the red-sideband Rabi frequency from centre to edge.

Sideband axial variation

Imperfect beam alignment lead to an additional variation of red-sideband coupling strengths that does not impact the carrier coupling strength Ω_R . This too is a constraint of access which sets the beam angles we can achieve for the lasers involved in Raman imaging. The horizontal Raman beam (R_2) bisects the horizontal lattice axis directions x and y , and is aligned to $-(x + y)/\sqrt{2}$. The Raman beam in the vertical axis (R_1) is aligned as $-z$, i.e. pointing towards the microscope objective (figure 3.4). This alignment of beams determine the resultant k_R wavevector for the two-photon process. This particular configuration is chosen such that there is a k_R component along each of the \hat{x} , \hat{y} and \hat{z} axes, thereby driving Raman sideband transitions in each axis. However, the k_R components and therefore the η_R are not equal along each axis (see figure 3.4).

For a fixed trap frequency, we see a large Lamb-Dicke parameter η_R , and consequently Raman sideband coupling strength $\eta_R \Omega_R$ along the vertical axis compared to the horizontal axis. For typical imaging trap depths, the Lamb-Dicke parameters are 0.17 and 0.12 for the vertical and horizontal lattices respectively. We therefore observe a higher frequency on sideband Rabi oscillations of the vertical \hat{z} lattice. Since we image atoms in a single anti-node of the vertical lattice (a single “layer” of the 3D lattice), and the coupling strengths along the horizontal lattices are symmetric, this does not present as an inhomogeneity in the field of view. However, the dephasing caused by

unequal coupling strengths could lead to inefficient cooling. The major heating sources (near resonant beams) are aligned in the horizontal direction where the reduced Lamb-Dicke parameter in the horizontal axis limits the cooling rate it is possible to achieve. For further discussion on the single-photon and two-photon Lamb-Dicke parameters in the experiment see appendix B.

3.3.4 Optimisation of imaging parameters

The above considerations provide guidelines within which we can fine-tune our imaging parameters. A point to remember is that deep traps can negatively impact imaging fidelity for two reasons: a) Increased heating from inverted excited state and b) Larger variations of trap frequencies across field of view. These factors lead to an upper limit on lattice depths suitable for imaging using RSC. The lower limit for trap depth is set by requiring the Lamb-Dicke parameter of D1 transition photons η_{D1} being sufficiently small to mitigate heating via scattering. We find that $2\pi \times 250$ kHz to $2\pi \times 300$ kHz is the range of trap frequencies for which we are best able to optimise imaging fidelity.

The primary sources of inhomogeneity are trap frequency variation and anharmonicity of the lattice potential. While the former can be mitigated by reducing trap depths, anharmonicity depends only on the wavelength of light used for trapping. This sets a lower bound on the Rabi frequency of the red-sideband ($\eta_R \Omega_R$) sufficient to be simultaneously resonant to multiple n levels in the lattice. The maximum Rabi frequency is constrained by the carrier transition growing faster than the sideband transitions, and for $\Omega_R \gg 2\omega_T$ overpowering the red-sideband transition. We find that $\Omega_R \sim 2\omega_T$ is ideal for imaging rather than the sideband resolved case $\Omega_R \ll \omega_T$. A slight overlap of the carrier transition with the red-sideband (in addition to optical pumping beam P_1) prevents the atoms in the $n = 0$ state being entirely dark to imaging.

Lastly, the beams near resonant the D1 line are $\sim 30\Gamma$ detuned to mitigate heating from the inverted excited state. Operating the experiment in pulsed mode (such that D1 and D2 transitions are independent of light shifts caused by the other) also demonstrated that cooling is more effective when both D1 beams are red-detuned from both $4P_{1/2}$ hyperfine levels. However, when returning to continuous mode operation which

Purpose	Beam	Detuning (Γ)	Scattering time τ (ms)
Pumping	P_1 ($\sigma-$)	25	0.06/1.5
repumping	P_2 ($\sigma-$)	35	0.043
Vert. Raman	R_1 (π)	-	81
Horz. Raman	R_2 ($\sigma-$)	-	122

Table 3.2: Detuning and scattering timescales for beams used during fluorescence imaging. Scattering rate of P_2 reflects the repumping rate of atoms prepared in $|F, m_F\rangle = |7/2, -7/2\rangle$ manifold. All other beams scatter from a 60:40 mixture of $|9/2, -9/2\rangle$ and $|9/2, -7/2\rangle$

has an improved signal, we find the two-photon detuning δ of the Raman transition is more sensitive to fluctuations in P_2 power as opposed to when P_2 is blue detuned from the $F' = 9/2$ and red-detuned from the $F' = 7/2$ hyperfine states. In this configuration, both hyperfine states of the $4P_{1/2}$ state contribute to a red-shift of the $F = 7/2$ state and hence red-shift the two-photon detuning. Hence, we implement an independent laser power regulation for P_2 instead of overlapping with R_2 and P_1 (see figure 3.4a).

3.3.5 Benchmarking imaging

Stable imaging with high signal-to-noise is a balance between cooling and heating processes that lead to an equilibrium distribution of n levels (see figure 3.6b) that is cold enough to prevent tunneling and loss events while not dark to imaging. We characterize all beams used during fluorescence via their detuning and scattering rates such that the characterization is independent of beam size or alignment to the atoms (see table 3.2). The single photon detuning for the Raman beams is set to $\Delta = 2\pi \times 40$ GHz, orders of magnitude greater than the linewidth $\Gamma = 2\pi \times 6$ MHz. We observe two timescales of scattering for P_1 which quickly pumps $|9/2, -7/2\rangle$ atoms but due to its polarisation only weakly affects $|9/2, -9/2\rangle$. The expected Raman Rabi frequencies for $n = 1$ are $2\pi \times 593$ kHz (carrier), $2\pi \times 100$ kHz (red-sideband vertical) and $2\pi \times 71$ kHz (red-sideband horizontal lattices).

3.4 Comparing Raman and EIT imaging

In the EIT cooling scheme a coupling laser near resonant to the D1 line is tuned $\sim 10\Gamma$ blue of the $4S_{1/2}, F = 9/2$ to $4P_{1/2}, F' = 7/2$ transition, creating light-dressed states which are admixtures of the ground and excited states. A probe laser from a metastable state then presents a Fano-like excitation profile [116] due to interference between the scattering amplitudes from the resulting dressed states. The detuning of the coupling beam from the excited state sets the asymmetry of the excitation profile and the sharpness of the transition. By calibrating the coupling beam intensity, we Stark shift the dressed state energies in magnitude equal to the trapping frequency ω_T . Thereby, we preferentially drive the red sideband transition while suppressing the carrier and blue sideband transitions via EIT. This cooling scheme has been used for single-atom imaging in optical lattices [134, 135], for efficient cooling to motional ground states in long ion-strings [136] and multimode EIT schemes [137, 138] are proposed for cooling more difficult ion crystals and molecules. For complete details on the implementation of this scheme for imaging in our experiment, refer to chapter 3 of D. Cotta's thesis [22].

While the previously implemented EIT imaging scheme was successful in imaging of sparse 2D layers of atoms, an unexpected issue arose when imaging dense layers with filling fractions $\langle n \rangle \sim 1$. The fluorescence per atom detected in regions of high filling was 3-4 times that of fluorescence in regions of low filling (figure 3.12b). While we are yet to fully understand this density dependent enhanced fluorescence, it significantly impairs image reconstruction (see figure 3.11, 3.13). At dense filling we cannot reliably determine when a site is empty. As can be seen in figure 3.13, in the case of sparse filling we can distinguish filled and empty sites in the histogram (separated by the green divider line). However, this fails in the case of dense images, with the separation between full and empty sites entirely masked in areas of high local density. This motivated our shift from EIT cooling to Raman cooling. Figure 3.14a demonstrates that the fluorescence per atom increases as the local filling fraction increases for EIT imaging. We expect that lattice sites with ~ 1 normalized fluorescence in areas of high local filling are likely empty sites or atoms lost partway through imaging. For Raman

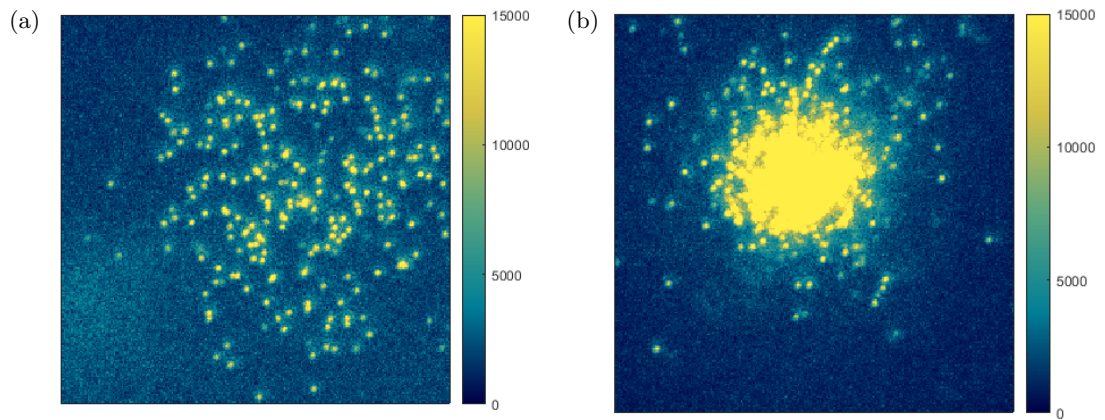


Figure 3.11: EIT imaging: 500 ms exposure of EIT imaging light for (a) sparse and (b) densely filled samples.

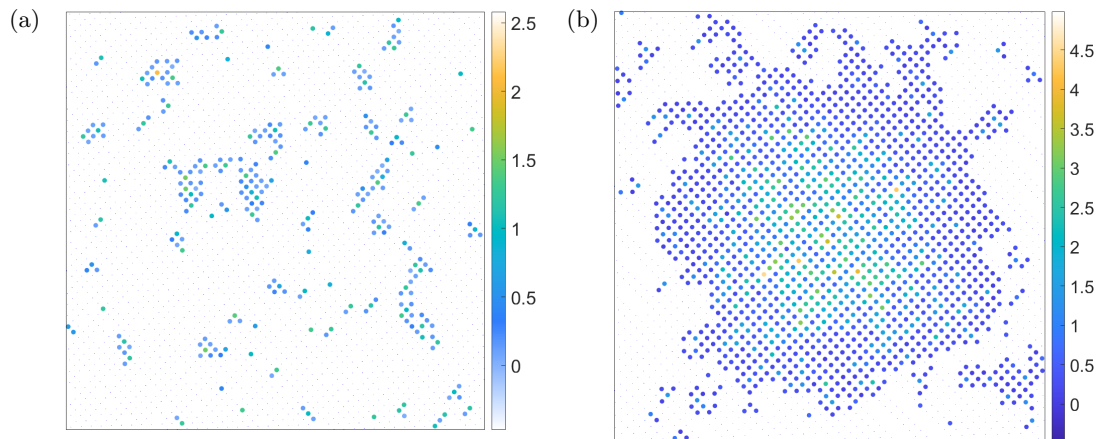


Figure 3.12: Matrix of occupied and unoccupied lattice sites in the central region of images 3.11a and 3.11b ((a) and (b) respectively). The fluorescence per site in locally dense regions of figure (b) is 3-4 times that of the fluorescence of atoms at the edges of the same image.

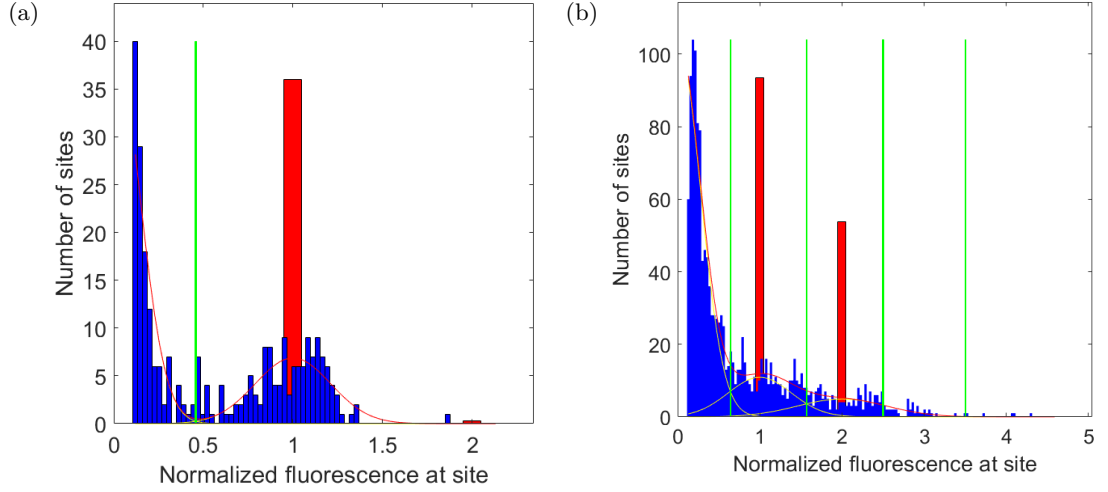


Figure 3.13: Failure of image recognition in distinguishing between filled and empty sites in figure 3.11. The left histogram shows the expected two peaks in the per-site fluorescence signal corresponding to empty (near zero) and filled (centred at one) sites. In the right histogram corresponding to dense samples, we are no longer able to separate these peaks.

imaging (figure 3.14b) the fluorescence per atom is independent of the filling fraction. The local filling fraction $\langle n_i \rangle$ about a site i in figure 3.14b is calculated by taking the average number of particles in the 25 closest neighbouring sites of site i (hence the minimum $\langle n_i \rangle$ value possible for an occupied site is $1/25$). In the case of EIT imaging, we are unable to reliably reconstruct the occupation matrix of the sample and hence estimate that the region of highest fluorescence corresponds to the region of highest density $\langle n_i \rangle_{\max}$. The filling fraction at all other sites is normalized against this value (i.e. $\langle n_i \rangle_{\max} = 1$). The fluorescence at each site in figure 3.14a was normalized against the fluorescence for sparse atoms that do not have immediate neighbours.

Analysing the efficiency of EIT and Raman imaging we find comparable CPL (923 and 805) and loss rates (4.8(1.2)% and 5.3(1.7)% respectively) with both imaging techniques.

Comparing figures 3.15 and 3.16 we see as expected that Raman imaging is more sensitive to the two-photon detuning δ_R , with the effective cooling region with $\leq 10\%$ losses $\Delta\delta_R$ being $\sim 2\pi \times 20$ kHz (figure 3.15a). The effective range of the EIT two-photon detuning $\Delta\delta_E$ is an order of magnitude wider. We also observe that the flu-

Chapter 3. Sideband Cooling

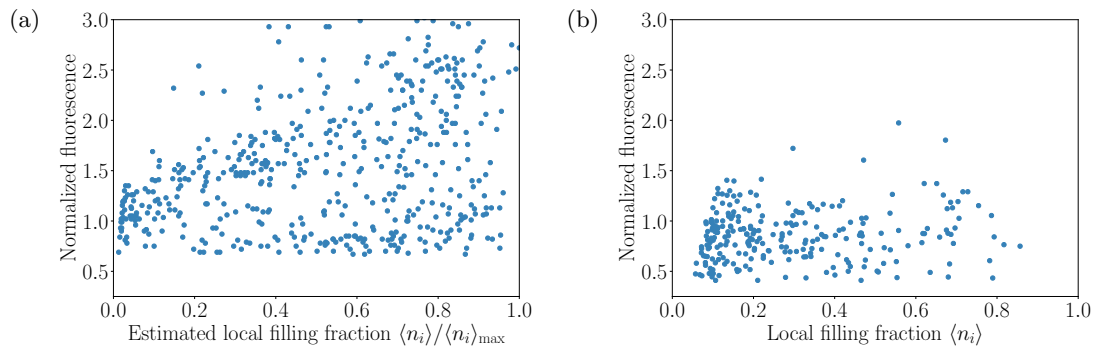


Figure 3.14: Fluorescence per atom (normalized) against local atom density (measured as filling fraction) for (a) EIT imaging and (b) Raman imaging. We see that fluorescence per atom in Raman imaging is independent of filling fraction while for EIT there is a strong correlation with density.

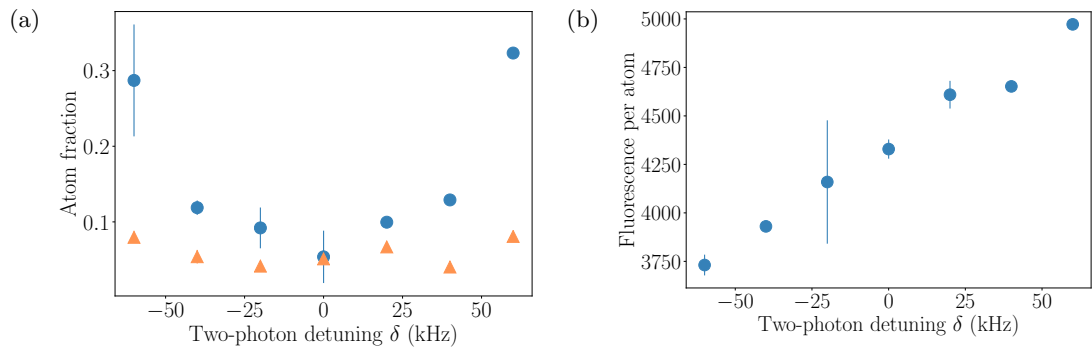


Figure 3.15: Fluorescence imaging using RSC: (a) Atom loss fraction (blue circles), tunneling fraction (orange triangles), and (b) fluorescence per atom vs Raman two-photon detuning.

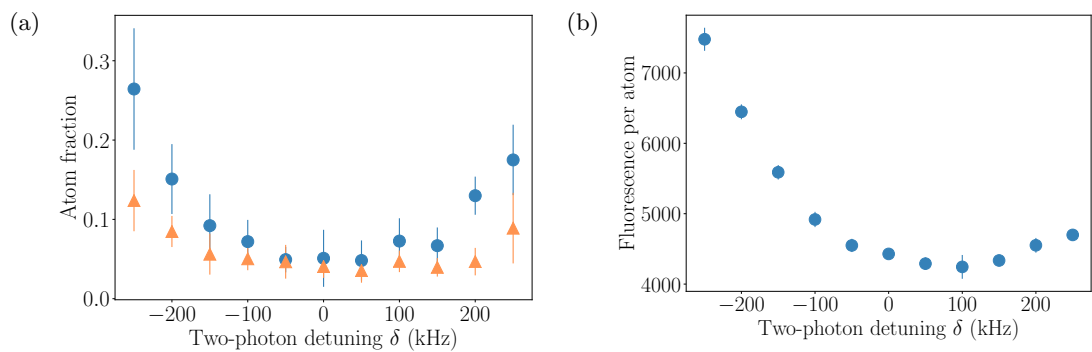


Figure 3.16: Fluorescence imaging using EIT: (a) Atom loss fraction (blue circles), tunneling fraction (orange triangles), and (b) fluorescence per atom vs EIT two-photon detuning.

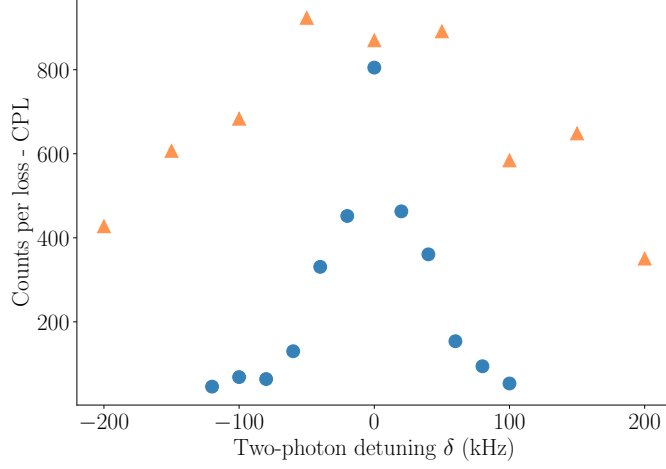


Figure 3.17: CPL (equation 3.9) against two-photon detuning for Raman imaging (blue circles) and EIT imaging (orange triangles).

orescence per atom in the case of the Raman imaging grows on increasing δ_R as we reach closer to the carrier transition peak. The CPL values of typical Raman and EIT two-photon detuning measurements (figure 3.17) show us that the two techniques are comparable for single atom detection. It also demonstrates how narrow the effective imaging regime is for Raman imaging as compared to EIT.

3.5 Conclusions

We have demonstrated that our implementation of Raman imaging is a viable tool for single atom detection and extracting inter-site correlations. We are able to capture 4000 photons per atom with the microscope and record a loss of 5% of atoms over two successive 1 s images. With the implementation of PI regulation of laser powers, we also find that this performance is stable and reproducible. Applying an improved image recognition algorithm (currently being developed by our group), we expect to be able to reliably reconstruct the atom distribution with fewer photons captured per atom, i.e., we aim to image with shorter exposure duration and hence lower loss of atoms ($< 4\%$) during imaging.

Most importantly, comparing the local density against fluorescence at each site for

Chapter 3. Sideband Cooling

Raman and EIT imaging, we observe that the Raman scheme is not handicapped by the same density dependent issue as EIT (figure 3.14). With a more reliable imaging scheme, we are better positioned for future work exploring strongly correlated Hubbard systems. In parallel, other members of the group have developed improved image analysis algorithms, which will be the subject of future publications. In combination with the experimental progress described in this chapter, we have demonstrated reliable single-atom imaging with high fidelities.

Chapter 4

Simulating heating rates

In the previous chapter, we considered the constraints on effective cooling and imaging in our experiment. A key source of the heating discussed was the strongly inverted excited state of ^{40}K in a 1064 nm optical potential. While the dipole-trapping lasers are red detuned from the $4S$ to $4P$ transition, they are blue detuned from the $4P$ to $3D$ transition. This proximity of the $3D - 4P$ transition to the 1064 nm laser frequency (figure 4.1a) results in an additional light-shift of the $4P$ state. In comparison, the $4P$ states experience a light-shift six times greater and opposite to the light-shift of the $4S$ state (figure 4.1b). When an atom is excited to the short-lived $4P$ states, it experiences a strong repulsive potential which accelerates and heats the atoms. This is in addition to heating from photon scattering. However, while a minimum amount of photon-recoil heating is inherent to any imaging scheme as we require the atoms to scatter a minimum number of photons to be detected, we can aim to minimize the heating from the inverted excited state. To better understand the characteristics of this effect we numerically study a two-level ^{40}K atom in presence of near resonant light in a 1D optical lattice trap. This simulation is carried out via the Quantum Toolbox in Python (QuTiP) package [139] using the quantum-trajectory method [140]. In doing so we aim to gain a better understanding of hopping and loss rates during fluorescence imaging.

In following sections we discuss the implementation of the quantum-trajectory technique and investigate how experimentally controlled parameters of lattice trap depth

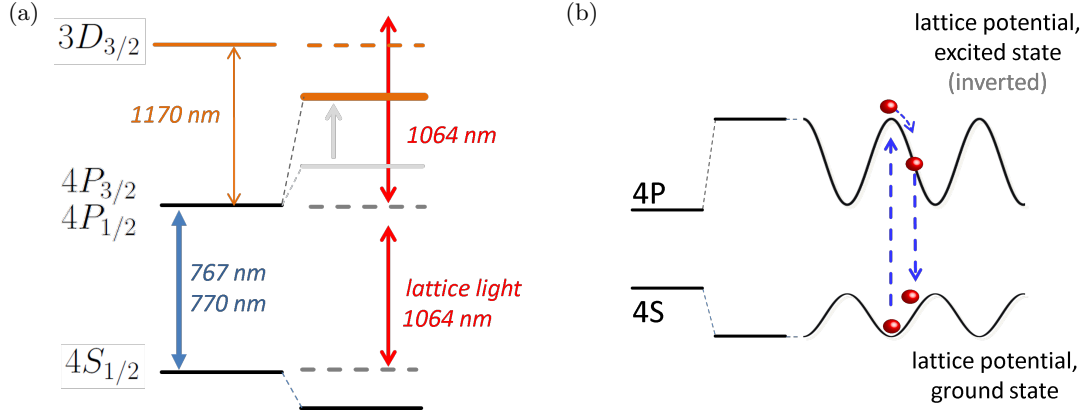


Figure 4.1: (a) ^{40}K $4S$, $4P$ and $3D$ levels relative to 1064 nm light. The lightshift of the $4P$ states without the presence of the $3D$ state is shown in grey. An additional lightshift (orange) is experienced by the $4P$ states owing to the $4P \rightarrow 3D$ transition at 1170 nm (b) Anti-trapped $4P$ states in a 1064 nm lattice. Note, light shifts are not drawn to scale.

and laser detuning affect heating rates. Further, we will evaluate the probabilities of light-assisted tunnelling to neighbouring lattice sites, i.e. whether atoms excited into the $4P$ state by the near-resonant light can tunnel to neighbouring lattice sites faster than predicted by the Hubbard model. Similarly, we explore light-assisted excitations into weakly trapped energy-states of the lattice.

In this chapter we will often refer to evolution time as t and temperature as T . Therefore, we will use the symbol J to refer to the tunnelling term of the Hubbard model (introduced in chapter 1 as t). We did not make this substitution in previous chapters so as to prevent any ambiguity with the spin-exchange interaction J_{ex} of the related Heisenberg model (as in section 1.2.2) or the $t - J$ model of strongly correlated electrons on a lattice [141]. In this chapter, we simulate an isolated spinless two-level atom, hence can unambiguously refer to the Hubbard tunnelling parameter as J .

4.1 Quantum-trajectory method

During the imaging process in deep lattices, we expect no more than one atom per lattice site with negligible inter-site tunnelling, i.e., a negligible possibility of interactions between atoms. Hence, we simulate a single isolated atom and ignore the effects of

interactions. Combining the electronic and motional degrees of freedom of the atom leads to a large Hilbert space, which makes full density-matrix evolutions (which scale as N^2 , where N is the size of the Hilbert space) computationally demanding.

4.1.1 Computational efficiency

A computationally efficient alternative is to take a stochastic average of pure states evolving over time (N variables) in multiple parallel trajectories. For an observable \hat{A} , state density operator $\hat{\rho} = \sum_i p_i |\psi_i\rangle \langle \psi_i|$, the two quantities at each time step are related as

$$\langle \hat{A} \rangle = \text{Tr}\{\hat{A}, \hat{\rho}\} = \sum_i p_i \langle \psi_i | \hat{A} | \psi_i \rangle = \sum_i p_i A_i \equiv \bar{A}_i. \quad (4.1)$$

\bar{A}_i is the stochastic average of the observable over individual trajectories. Instead of propagating a density-matrix of N^2 variables, we propagate multiple pure-states of size N . When the number of such pure-state ‘trajectories’ averaged over is less than N it is computationally less expensive than the traditional density matrix evolution. The quantum-trajectory approach also lends itself naturally to parallelization as the trajectory are independent of each other, significantly reducing computation time. The tradeoff inherent in the method is that statistical error enters into the time-evolution of the system. The magnitude of the error is inversely proportional to \sqrt{M} (where M is the number of trajectories) and hence must be mitigated by averaging over several trajectories.

4.1.2 Implementation

Under the Markov approximation [142], the Lindblad form of the master equation is:

$$\dot{\hat{\rho}} = -\frac{i}{\hbar}[H, \hat{\rho}] - \frac{1}{2} \sum_m \Gamma_m [c_m^\dagger c_m \hat{\rho} + \hat{\rho} c_m^\dagger c_m - 2c_m \hat{\rho} c_m^\dagger]. \quad (4.2)$$

The time evolution (equation 4.2) depends on two components, the first being the reversible Schrödinger equation, the second term corresponding to the linear irreversible

interaction with the environment (referred to as the Lindbladian). The operators c_m are collapse operators for the m decay channels, and Γ_m is the decay linewidth. In the case of a typical two-level atom, equation 4.2 can be rearranged as

$$\dot{\hat{\rho}} = -\frac{i}{\hbar}[\hat{H}_{\text{eff}}, \hat{\rho}] + \sum_m \Gamma_m \hat{c}_m \hat{\rho} \hat{c}_m^\dagger, \quad (4.3)$$

where $\hat{H}_{\text{eff}} = \hat{H} - i\hbar/2 \sum_m \Gamma_m \hat{c}_m^\dagger \hat{c}_m$. \hat{H}_{eff} is no longer hermitian, leading to a reduction in the trace of $\hat{\rho}$ over time. The second term from Eq 4.3 "recycles" this lost atom population back into the ground state via any of the m decay channels.

The effective Hamiltonian is applied on a pure state at time t which leads to a reduction in the norm of the state. i.e. $\langle \psi(t+dt) | \psi(t+dt) \rangle = 1 - dp < 1$. The reduction in norm,

$$dp = \sum_m \langle \psi(t) | \hat{c}_m^\dagger \hat{c}_m | \psi(t) \rangle = \sum_m dp_m, \quad (4.4)$$

is the probability for the state to decay via the m channels.

Thus, with a probability of $1 - dp$, the state continues its coherent evolution, where we renormalize the state $\psi(t+dt)$ at each time step. With a probability of dp_m it collapses into the decay channel m as $\psi'(t+dt) = \hat{c}_m \psi(t) / dp_m$. This approach is realized by the Monte-Carlo solver - `qutip.mcsolve` [139]. A trajectory begins by choosing a random number r such that $0 < r < 1$. We evolve the system coherently under \hat{H}_{eff} while $dp < r$. If $dp \geq r$ we then collapse it into one of the m decay channels with probability proportional to dp_m and generating a new random number r for the subsequent collapse probability.

4.2 Two-level atom in a 1D lattice

In this section we treat the system semi-classically [143], with the atom being a two-level quantum-mechanical system while the light interaction is classical (i.e., we do not include the energy of the photon field in the Hamiltonian). We then include spatial and kinetic terms to create the total Hamiltonian. We introduce the appropriate collapse

operators for atoms spontaneously decaying from the excited state to complete the master equation. Finally, we implement the quantum-trajectory method with and without an inverted excited state and compare results with our physical intuitions.

4.2.1 Semiclassical light-atom interaction

The two orthonormal states $|1\rangle$ and $|2\rangle$ have an energy spacing E . We consider their interaction with a narrow-linewidth laser with modes centred at ω_l . We denote the detuning between the laser and atomic energy levels as $\Delta = \omega_l - E/\hbar$. We represent the two states as

$$|1\rangle = \begin{pmatrix} 1 \\ 0 \end{pmatrix}, |2\rangle = \begin{pmatrix} 0 \\ 1 \end{pmatrix}. \quad (4.5)$$

The Hamiltonian describing this system is $\hat{H}_A = \frac{E}{2} |2\rangle \langle 2| - \frac{E}{2} |1\rangle \langle 1|$ (where the reference energy is $E_0 = (E_{|1\rangle} + E_{|2\rangle})/2$, i.e., the mean of the two atomic energy levels). The total internal Hamiltonian for this system, \hat{H}_{AL} , considers only the bare atomic system and the interaction energy with a classical light field. i.e. $\hat{H}_{AL} = \hat{H}_A + \hat{H}_I$.

The dipole interaction between light field and the atom arises due to the electric-field amplitude $E_0 \cos(\omega_l t)$ of the incident light. Under the rotating-wave approximation [144] we find matrix elements of the interaction Hamiltonian $\langle 1 | \hat{H}_I | 2 \rangle = \langle 2 | \hat{H}_I | 1 \rangle^* = \hbar g e^{i\omega_l t}$, where

$$g = E_0 \frac{e}{2\hbar} \int_{-\infty}^{+\infty} \psi_1^* D_{E_0} \psi_2 d\vec{r} \quad (4.6)$$

characterizes the strength of the interaction [106], where D_{E_0} is the induced dipole moment of the atom. Since the dipole-interaction term has odd parity, the integral vanishes unless ψ_1 and ψ_2 (the wavefunctions of states $|1\rangle$ and $|2\rangle$ respectively) have opposite parity. Therefore, the diagonal terms of the interaction Hamiltonian vanish

and we have

$$\hat{H}_I = \begin{pmatrix} 0 & \hbar g e^{i\omega t} \\ \hbar g e^{-i\omega t} & 0 \end{pmatrix}. \quad (4.7)$$

Adding the above interaction Hamiltonian to the bare atomic Hamiltonian, \hat{H}_A , we have an atom-light interaction Hamiltonian \hat{H}_{AL} :

$$\hat{H}_{AL} = \begin{pmatrix} -\frac{E}{2} & \hbar g e^{i\omega t} \\ \hbar g e^{-i\omega t} & \frac{E}{2} \end{pmatrix}. \quad (4.8)$$

It can be shown that

$$\begin{pmatrix} -\frac{E}{2} & \hbar g e^{i\omega t} \\ \hbar g e^{-i\omega t} & \frac{E}{2} \end{pmatrix} = \begin{pmatrix} e^{i\hbar\omega t/2} & 0 \\ 0 & e^{-i\hbar\omega t/2} \end{pmatrix} \begin{pmatrix} -\frac{E}{2} & \hbar g \\ \hbar g & \frac{E}{2} \end{pmatrix} \begin{pmatrix} e^{-i\hbar\omega t/2} & 0 \\ 0 & e^{i\hbar\omega t/2} \end{pmatrix}. \quad (4.9)$$

This is of the form $\hat{H}_{AL} = \hat{U}(t)\hat{H}_T\hat{U}^\dagger(t)$, i.e., we can transfer the explicit time dependence of the Hamiltonian into the state via a unitary transformation $\hat{U}(t)$ into a rotating frame such that

$$\hat{U}(t) = \begin{pmatrix} e^{i\hbar\omega t/2} & 0 \\ 0 & e^{-i\hbar\omega t/2} \end{pmatrix}, \quad (4.10)$$

where $\psi = \hat{U}(t)\phi(t)$. The Schrödinger equation before this transformation is:

$$i\hbar \frac{\partial}{\partial t} \psi = \hat{H}_{AL} \psi. \quad (4.11)$$

Substituting ψ , we have

$$i\hbar \frac{\partial}{\partial t} \hat{U}(t)\phi = \hat{H}_{AL} \hat{U}(t)\phi, \quad (4.12)$$

$$i\hbar \left(\hat{U}(t) \frac{\partial}{\partial t} \phi + \frac{\partial}{\partial t} \hat{U}(t) \phi \right) = \hat{H}_{AL} \hat{U}(t)\phi. \quad (4.13)$$

We expand the Hamiltonian matrix, taking the partial differential of $\hat{U}(t)$ and re-arranging terms:

$$i\hbar\hat{U}(t)\frac{\partial}{\partial t}\phi = \left[\begin{pmatrix} -\frac{E}{2} & \hbar g e^{i\omega_L t} \\ \hbar g e^{-i\omega_L t} & \frac{E}{2} \end{pmatrix} + \begin{pmatrix} \hbar\omega_L t/2 & 0 \\ 0 & -\hbar\omega_L t/2 \end{pmatrix} \right] \hat{U}(t)\phi \quad (4.14)$$

$$i\hbar\frac{\partial}{\partial t}\phi = U^{-1}(t)\hbar \begin{pmatrix} \Delta/2 & g e^{i\omega_L t} \\ g e^{-i\omega_L t} & \Delta/2 \end{pmatrix} \hat{U}(t)\phi. \quad (4.15)$$

Thus, the Schrödinger equation in this rotating frame is

$$i\hbar\frac{\partial}{\partial t}\phi = \hbar \begin{pmatrix} \Delta/2 & g \\ g & -\Delta/2 \end{pmatrix} \phi. \quad (4.16)$$

Here, $\Omega_0 = 2g$, such that we get an effective Rabi-frequency [145] and energy separation between dressed states on diagonalizing this matrix as $\Omega_{\text{eff}} = \sqrt{\Omega_0^2 + \Delta^2}$.

4.2.2 Including motional degrees of freedom

The motional component of the Schrödinger equation is of the form

$$\left(\frac{-\hbar^2}{2m} \frac{\partial^2}{\partial x^2} + V_0 \sin^2(k_L x) \right) \psi = E_X \psi. \quad (4.17)$$

Here, m is the mass of the atom, V_0 is the maximum potential depth of the lattice, k_L is the wavevector of lattice light and E_X are the eigenenergies in position space. For convenience, we rescale to dimensionless units. Replacing with $x' = x k_L / \sqrt{2}$ and noting that $\hbar^2 k_L^2 / 2m = E_{\text{rec}}$ where E_{rec} is the recoil energy of a lattice photon, Eq 4.17 evaluates to

$$\left(-\frac{1}{2} \frac{\partial^2}{\partial x'^2} + \frac{V_0}{E_{\text{rec}}} \sin^2(x' / \sqrt{2}) \right) \psi = \frac{E_X}{E_{\text{rec}}} \psi. \quad (4.18)$$

This naturally leads to an energy re-scaling in units of E_{rec} , and further a frequency scaling of $\omega_{\text{rec}} = E_{\text{rec}} / \hbar$. To incorporate the inversion of the excited state, we create a

complete Hamiltonian H_T of the form

$$H_T = \hat{H}_{AL} \otimes \hat{I}_X + \begin{pmatrix} 1 & 0 \\ 0 & V_{\text{ratio}} \end{pmatrix} \otimes \hat{H}_X. \quad (4.19)$$

I_X is an identity matrix in position space and H_X describes the lattice potential. $V_{\text{ratio}} = -6$ for an inverted excited state potential six times larger than the ground state potential. In the current stage, we do not include the motional kick from absorption of a photon. This would lead to a linear momentum gain with every absorption and thus a quadratic gain in energy which becomes the dominant heating mechanism, masking the heating effect of the inverted excited state. We can consider this as simulating the heating in the \bar{z} axis while the near resonant polarizer and repumping beams are in the $x - y$ plane.

We include the recoil kick from scattering photons via the collapse operators

$$c_{(0,1)} = \left(\frac{1}{2} \sqrt{\Gamma} a \otimes e^{-ik_R x}, \frac{1}{2} \sqrt{\Gamma} a \otimes e^{ik_R x} \right), \quad (4.20)$$

where k_R is the wavevector of the scattered photon, a is the annihilation operator $|0\rangle \langle 1|$ and Γ is the scattering rate from the excited state. The two terms describe a recoil kick in the $-x$ direction and the $+x$ direction, respectively, with 50% probability of each collapse.

In the following sections, we utilize the quantum trajectory method to simulate a 2-level atom within a position space of 1024 discrete points. The time-evolution is averaged over a large number of trajectories (M) to reduce statistical errors. The number of trajectories is chosen by simulating the system up to 10 scattering events (see equation 4.21) with $M = 100$. This is repeated with higher M at each iteration until the results do not depend on M and do not vary significantly between iterations. In doing so, we find that $M = 500$ is sufficient for time-evolution up to 10 scattering events and all simulations in this chapter average over $M = 500$ trajectories. However, as the statistical errors grow with evolution time, higher M and more computational resources would be required for time-evolution of up to 100 or more scattering events.

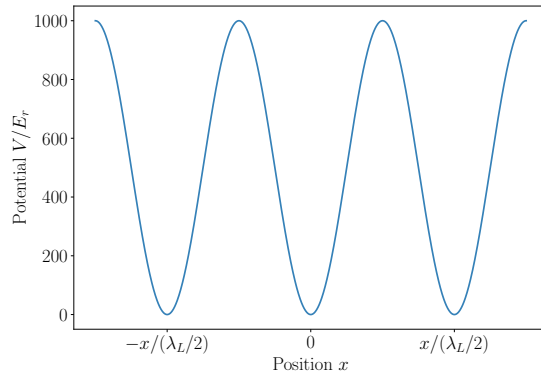


Figure 4.2: Three-site 1D optical lattice: $V = V_0 \sin^2(k_L x)$, $x \in [-3\lambda_L/4, 3\lambda_L/4]$, $V_0 = 1400E_r^L$ used in the quantum-trajectory simulations.

We do not include error bars as we are interested in qualitative results at this stage, however, see section III B of [140] for details on estimating errors from the quantum trajectory technique. In section 4.2.3, we discuss the starting point of all simulations, i.e., the method we use to initialize the system.

4.2.3 Constructing the initial state

During the imaging process we expect the atoms are well localized to individual lattice sites. Therefore we need to initialize the simulation with an atom fully localized in a single site. However, the eigenstates of a 1D lattice are typically de-localized across the lattice, whereas atoms are localized in individual sites during imaging. For simplicity, we aim to initially populate only in the central site of a three-site lattice. This is equivalent to the atom's state after it has scattered the very first fluorescence photon and localized to a lattice site.

A straightforward approach to create localized eigenstates is by adding a small Gaussian confining potential that lowers the energy of eigenstates localized in the central site. This approach works well, breaking the degeneracy of eigenstates in each band with one eigenstate being localized at the central site and of lower energy than the other eigenstates of the lattice energy band (see Fig. 4.3). The number of eigenstates in a band is equal to the number of sites. i.e. for a three-site 1D lattice (figure 4.2), there are three eigenstates $m = 0$, $m = 1$ and $m = 2$ in the lowest vibrational level $n = 0$

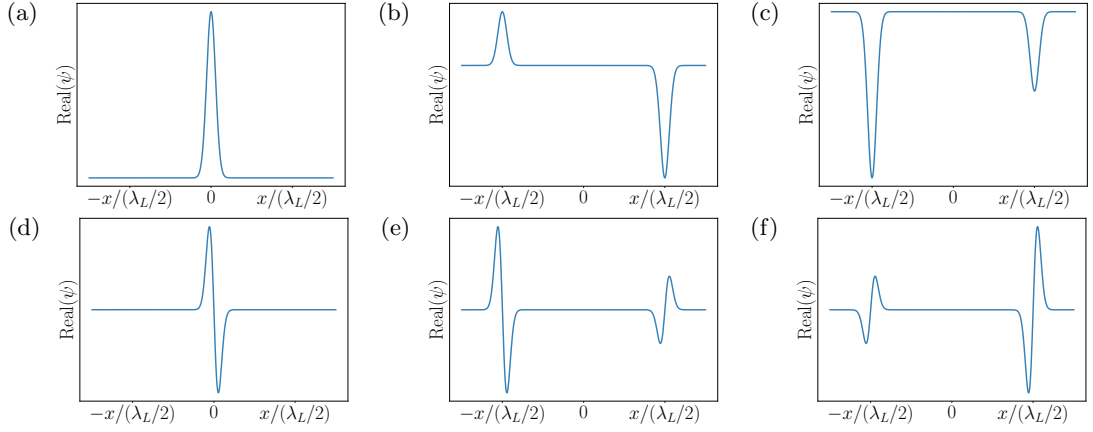


Figure 4.3: Atom wavefunctions in 3-site optical lattice with sites at $x = -\lambda/2$, 0 and $+\lambda/2$. Eigenstates of $n = 0$ vibrational level ((a) $m = 0$, (b) $m = 1$ and (c) $m = 2$) and $n = 1$ vibrational level ((d) $m = 3$, (e) $m = 4$ and (f) $m = 5$) for a three-site 1D optical lattice with $\omega_T = 2\pi \times 300$ kHz with an additional weak Gaussian confinement ($V_G = 0.01 x^2$).

(i.e. of energy $\sim 0.5\hbar\omega_T$). With the added Gaussian confinement, the $m = 0$ state is localized to the central site (figure 4.3a). The eigenstates $m = 1$ and $m = 2$ fill the non-central sites (figures 4.3b, 4.3c) and are degenerate. Similar behaviour is observed for the states in the $\sim 1.5\hbar\omega_T$ vibrational level (figures 4.3d, 4.3e, 4.3f) and higher.

It would however be preferable not to require an additional confinement as it might affect tunnelling rates. An alternative approach we have tested with success is to initialize the system in the eigenstates of a harmonic oscillator potential which is aligned with the central lattice site (see Fig. 4.4a). We compare the eigenstates of the harmonic oscillator potential against a one-site lattice potential (Fig. 4.4c). We find that for sufficiently deep traps, the harmonic oscillator eigenstates are very similar to lattice eigenstates for a one-site lattice. Therefore we can initialize the atoms in the eigenstates of a harmonic potential at the central site. This gives us a greater degree of flexibility in where we initialize the atom by making initialization independent of the lattice potential.

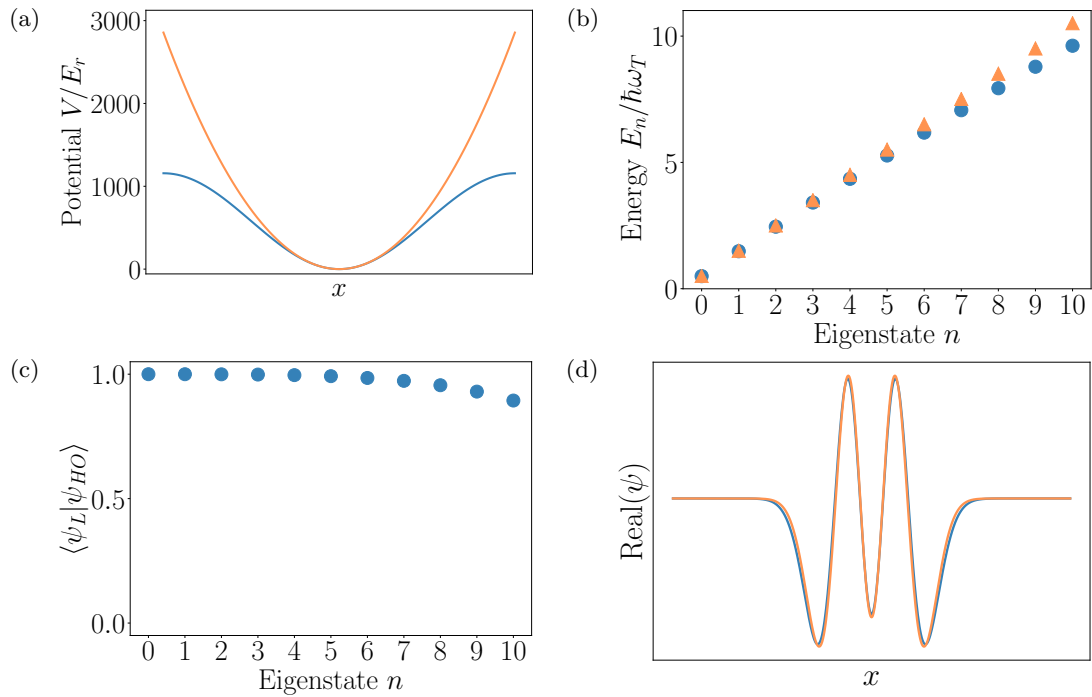


Figure 4.4: Comparing harmonic oscillator eigenstates and eigenenergies with one-site lattice: (a) Harmonic trap (orange) centred on a one-site 1D lattice (blue). (b) Eigenenergies of harmonic oscillator potential (orange) and one-site 1D lattice (blue). (c) Inner-product of harmonic oscillator and corresponding 1D lattice eigenstate for $\omega_T = 2\pi \times 50$ kHz (orange) and $\omega_T = 2\pi \times 300$ kHz (blue). Figure (d) shows the harmonic oscillator (orange) and lattice (blue) eigenstate wavefunctions corresponding to $n = 4$.

4.2.4 Benchmarking with non-inverted excited state

There are three key advantages to implementing the simulation via the QuTiP package. First, the parallel computation of quantum trajectories is built-in and provides a dramatic speedup to calculations. Second, it implements efficient memory management, saving only the expectation values of our chosen observables in memory rather than the full wavefunction. Lastly, `qutip.mcsolve` calibrates the size of time steps dt such that the change in the norm of the state $\psi(t + dt)$ in each time step is small. In this section we check that the results from the program match our physical intuitions.

While our objective is to simulate the behaviour of the atom at $V_{\text{ratio}} = -6$, we first simulate the behaviour of the atom for $V_{\text{ratio}} = 1$. This beta simulation serves as a sanity check for the developed code (refer figure 4.5). A convenient unit of time to study the behaviour of the atom is $t' = \Gamma_{\text{eff}}t$. $\Gamma_{\text{eff}} = P_e\Gamma$ is the effective scattering rate of the two-level system depending on the average population in the excited state:

$$P_e = \frac{\Omega^2}{2\Omega^2 + 4\Delta^2 + \Gamma^2}. \quad (4.21)$$

Here, Ω is the coupling strength of incident light, Δ is its detuning from resonance and Γ is the natural linewidth of the excited state. $\Gamma_{\text{eff}}t$ is a dimensionless unit of time. Once the atom has reached its steady-state distribution in the excited state (equation 4.21), we expect on average one spontaneous decay event per $\Gamma_{\text{eff}}t$. Note, the cooling provided by the Raman sideband process opposes the heating from all sources. Hence, in the physical experiment we expect the system to quickly reach an equilibrium temperature and band-number distribution. Since we do not include a cooling mechanism in the numerical calculations, we evolve the system up to 10 scattering events so as to get a qualitative idea of the heating mechanism which would directly impact the equilibrium distribution during imaging. For the parameters listed in the figure 4.5, we see the physically expected behaviour which completes the sanity check. The internal states of the atom undergo damped Rabi oscillations (figure 4.5a). To understand the evolution of kinetic energy (figure 4.5d) and momentum (figure 4.5c) we recall that the scattering events cause momentum transfers in opposite directions with a probability of 1/2 in

Chapter 4. Simulating heating rates

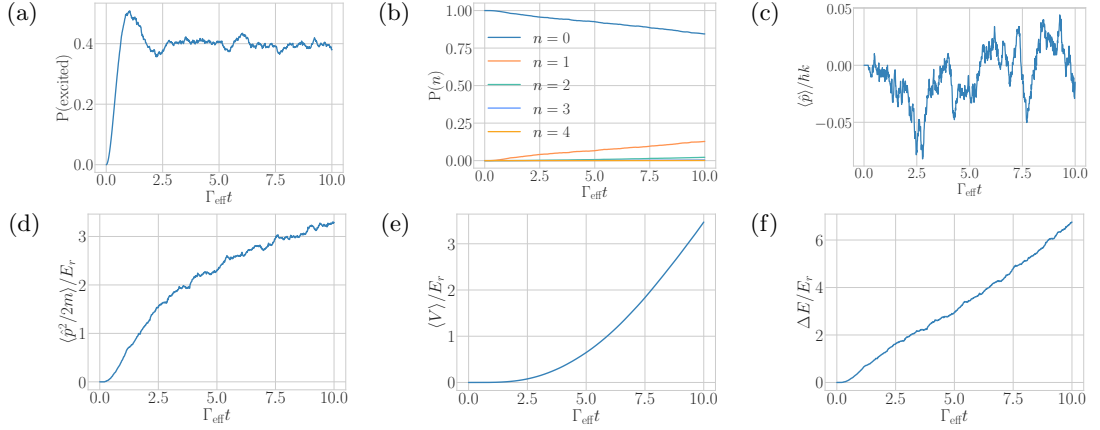


Figure 4.5: Time evolution of key atomic observables up to 10 spontaneous scattering events for a non-inverted excited state: single-site 1D lattice with $\Omega_0 = 5/6\Gamma$, $\Delta = -1/6\Gamma$, $\omega_T = 2\pi \times 300$ kHz. (a) Damped Rabi oscillations of population in excited state. (b) Motional state distribution. (c) Momentum gain $\langle \hat{p} \rangle$. (d) Kinetic energy gain $\langle \hat{p}^2 / 2m \rangle$. (e) Potential energy gain $\langle V_0 \sin^2(k_L \hat{x}) \rangle$. (f) Total energy gain $\langle \hat{H}_X \rangle$. Momentum in $\hbar k$ units, Energies in $\hbar^2 k^2 / 2m$ units where k corresponds to a D1 photon and m is the mass of a ^{40}K atom.

each. The change in momentum Δp at each time step i is equal to $\pm \hbar k$ where $\hbar k$ is the momentum of the emitted photon with the sign of Δp corresponding to momentum kicks in the positive and negative directions. Hence the average momentum after n scattering events would be:

$$\langle \hat{p} \rangle = \left\langle \sum_i (\pm \hbar k) \right\rangle = 0. \quad (4.22)$$

As on average half the momentum kicks are positive and half are negative, we do not expect a net momentum gain over time. However, the kinetic energy gain after i time steps scales as the momentum squared:

$$\langle \hat{p}^2 \rangle = \left\langle \sum_i (\pm \hbar k)^2 \right\rangle = n(\hbar k)^2. \quad (4.23)$$

Thus, the kinetic energy initially increases linearly (Fig 4.5d) until the atom's wavefunction spreads in the trap, leading to a damping of kinetic energy gain and a growth in potential energy (Fig 4.5e). The total energy (figure 4.5f) gain is linear, growing at

roughly one D1 photon recoil energy per scattering event. This behaviour is independent of trap depth ω_T which is what we expect in the case of a non-inverted potential, i.e. the trap does not contribute to the heating of atoms. We do not include the effect of photon recoil from absorption of photons from the light field as this is always in the same direction and leads to a linear momentum gain and hence a quadratic gain in kinetic energy over time, obscuring the heating caused by the inverted excited state.

4.3 Heating due to inverted excited state

Critically, we are interested in heating rates and its dependence on trap depth, laser detuning and the motional state of the atoms. The microscope objective captures 12% of the photons scattered by each atom and requires ~ 1000 photons per atom for an appropriate signal-to-noise ratios. Hence, we need to ensure the atoms scatter photons at 10 kHz for a 1 s imaging duration, i.e., if we detune the incident light further, we also increase its intensity such that the effective scattering rate is maintained (figure 4.7). This also matches well with the measured scattering rate (table 3.2) from the re-pumping beam (P_2) which is the source of fluorescence photons.

Trap depth

Once we have an inverted excited state, we see that atom heating is dependent on the trap depth (see Fig. 4.6), where for a non-inverted potential there was no dependence on trap depth (Fig. 4.6a). Furthermore, the heating rate from the inverted excited state is an order of magnitude greater than the recoil heating caused by scattering photons by spontaneous decay.

Detuning

The further we are detuned from resonance, the lower the heating from the inverted excited state. The fraction of time spent by atoms in the excited state is inversely dependent to the detuning from resonance. The closer to resonance the incident light field, the more time atoms spend in the excited state for a given laser intensity. To be

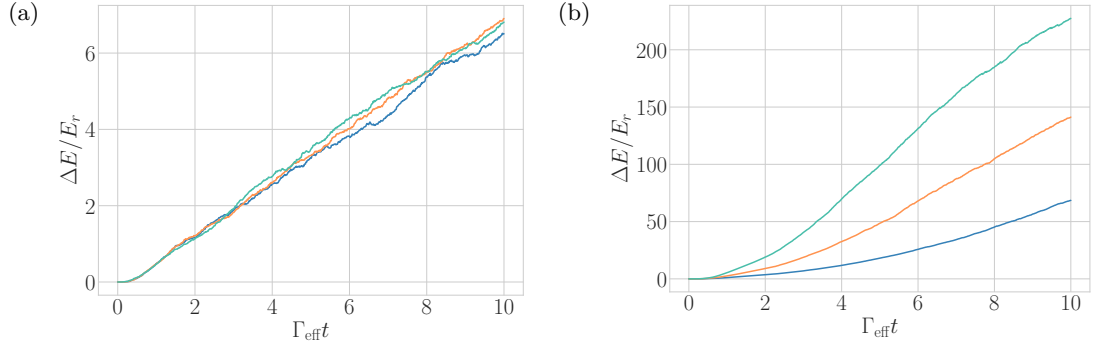


Figure 4.6: Heating rate dependence on trap depth ω_T . $\Omega_0 = 5/6\Gamma$, $\Delta = -1/6\Gamma$, $\omega_T = 2\pi \times 200$ kHz (blue), $2\pi \times 300$ kHz (orange), $2\pi \times 400$ kHz (green). Figure (a) Non-inverted excited state: $V_{\text{ratio}} = 1$, (b) Strongly-inverted excited state: $V_{\text{ratio}} = -6$.

more accurate, when we are closer to resonance the lower dressed state has a higher percentage of $4P$ or anti-trapped character as described by equation 4.21.

However, even matching the coupling strength of incident light to ensure the same percentage of the atoms in the excited state, (i.e. we fix scattering rate $\Gamma_{\text{eff}} = P_e\Gamma$ to 10 kHz), detuning plays a significant role in heating /energy gain in the system (see Fig. 4.7). This matches what we have observed in experiment (see table 3.2 where we find optimal imaging at detuning $\geq 25\Gamma$). This is another indication that the inverted state heating is a more dominant effect than the photon-recoil of scattering fluorescence photons as the number of scattered photons is kept constant while changing detuning.

Initial motional state

Unlike in the case of detuning or trap depth, we do not find a conclusive dependence of heating rates on the motional state the atom is in prior to being illuminated with near-resonant light (Fig. 4.8). While $n = 4$ appears to show the greatest heating rate, we see that $n = 5$ appears to have the lowest heating rate. We expect this has arisen from the uncertainty in the simulation technique. This is of importance to our experiment as depending on the Raman cooling parameters, we believe we reach an equilibrium distribution of motional states with $n > 0$ as the lowest lattice bands are dark to the Raman transition. Furthermore, the upper limit for energy bands is roughly $n \sim 10$ due

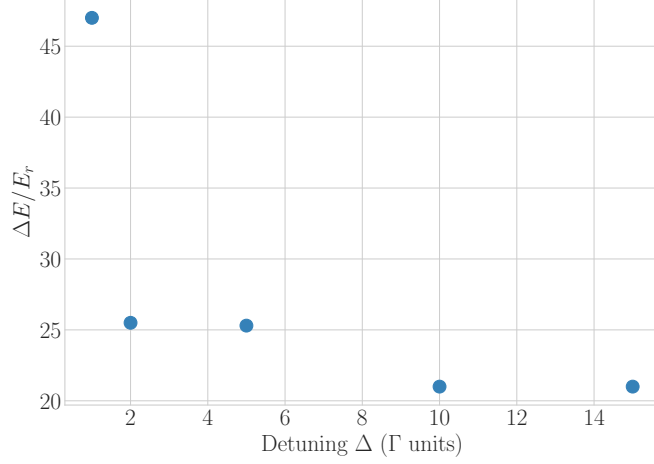


Figure 4.7: Energy increase/heating vs laser detuning while maintaining 10 kHz scattering rate.

to the effect of the anharmonicity of the lattice leading to about a 4.4 kHz separation between Raman transitions for successive n levels.

4.3.1 Tunnelling probability over time

The tunnelling matrix element in the Hubbard model, referred to as J in this chapter, decreases for deeper lattices, i.e., we expect lower tunnelling rates in deeper lattices. The fluorescence imaging scheme requires ~ 1 s of exposure. If a non-negligible fraction of atoms hop to neighbouring sites within this time, we cannot reliably reconstruct the atom distribution prior to imaging. The timescales for such tunnelling, τ , for a Hubbard tunnelling parameter, J , is approximately $\tau(J) = \hbar/2J$. The tunneling matrix element for the lowest band in shallow lattices can be approximated via the Mathieu equation [146] (Fig. 4.9a and 4.9b)

$$J = \frac{4}{\pi} E_r (s)^{3/4} e^{-2\sqrt{s}}$$

where $s = V_0/E_r$. We see that tunnelling timescales in the $n = 0$ band become exceedingly larger than lattice lifetimes for traps $\geq 80 E_r$, hence we expect this to be negligible for deep traps ($\sim 1000 E_r$) used during imaging.

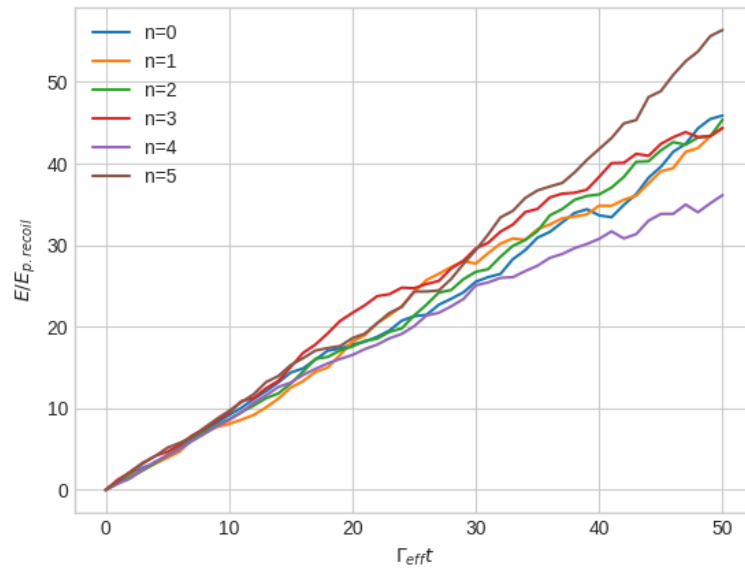


Figure 4.8: Energy increase/heating vs effective time for initial motional states $n = 0$ to $n = 5$.

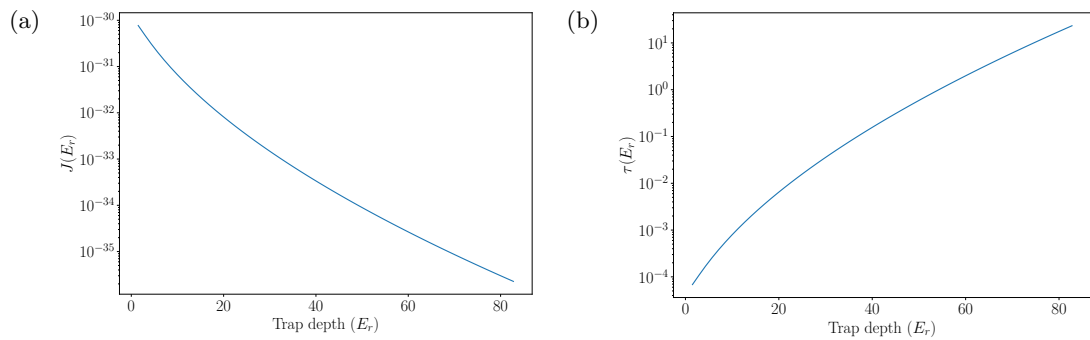


Figure 4.9: Tunneling characteristics in the $n = 0$ vibrational level vs lattice trap depth: (a) J parameter. (b) Tunneling timescale $\tau(J) = \hbar/2J$.

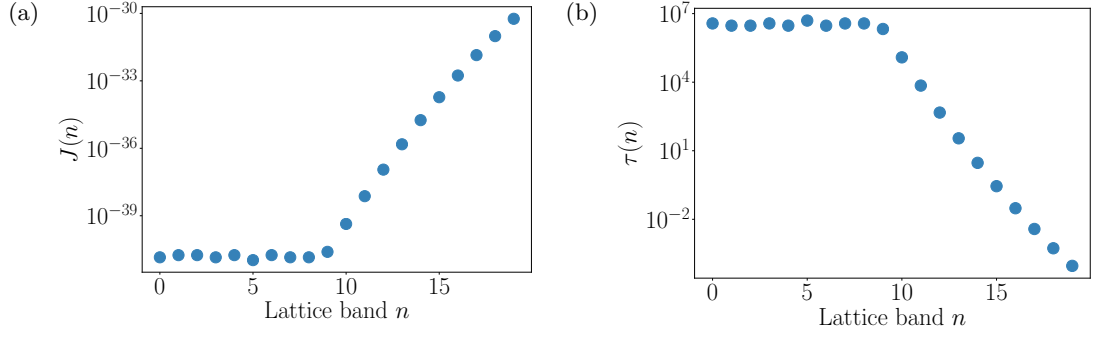


Figure 4.10: (a) Tunnelling parameter J and (b) tunnelling timescale $\tau = \hbar/2J$ for atoms in energy band n in a lattice of $\omega_T = 2\pi \times 300$ kHz.

We can also diagonalize the Hamiltonian and numerically calculate the tunneling parameter J vs n for deep lattices. We consider a deep lattice ($\omega_T = 2\pi \times 300$ kHz) which is of the order used during fluorescence imaging. Treating the deep lattice in accordance with the tight-binding model, we find the tunnelling parameter for a lattice band as $J(n) = W(n)/4$, where $W(n)$ is the width of the band n [147]. From figures 4.10a and 4.10b we see that tunnelling timescale in deep lattices approaches the imaging duration for $n \geq 12$. The takeaway from these calculations is that to reduce inter-site hopping during imaging we should prevent atoms occupying motional states $n \geq 12$. Moreover, atoms in lattice bands $n \geq 15$ would become off resonant to the Raman cooling transition (table 3.1). This further underscores the need for efficient cooling during imaging to prevent atoms reaching these high n states. From temperature measurements in figure 3.6b we see that the atoms are cooled well enough that occupying such high energy bands during Raman imaging is low. Using the quantum-trajectory method, we simulate the probability of atoms remaining in the central site of a 3-site 1D lattice when being exposed to near resonant light. Counter-intuitively, we see that the tunnelling probability - like the heating effect - is directly proportional to the trap depth, i.e, deeper traps lead to faster tunnelling rates. To get a fuller picture we would need to incorporate Raman cooling as well. However, initial indications via simulation and experiment are that increasing trap depths would not improve loss and hopping percentages during imaging. More strikingly, the motional band n occupied by the atom is not the dominant factor determining the probability of the atom tunneling to

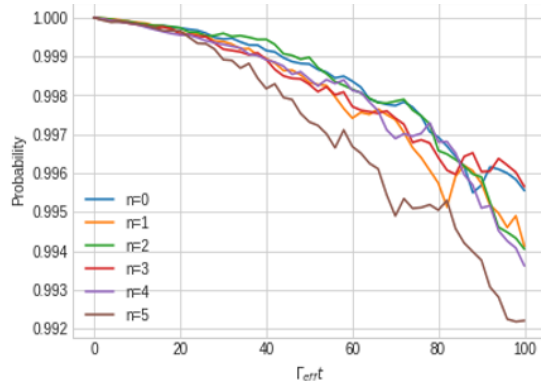


Figure 4.11: Probability of atom staying in the central site of a 3-site lattice over increasing effective time $\Gamma_{\text{eff}}t$. Simulated for different initial motional state n for light-field parameters $\Omega = 2.5\Gamma$, $\Delta = -10\Gamma$, $\omega_T = 2\pi \times 300$ kHz.

neighbouring sites. In figure 4.11 we notice that the tunneling rate does not conclusively depend on motional state, with $n = 3$ appearing to have the lowest tunneling rate and $n = 5$ the highest tunneling rate, with less than a percent of difference arising over 100 scattering events. We believe this variance is within the uncertainty of the quantum trajectory method which grows over simulation time. This implies that the tunnelling effect caused by heating from incident light dwarfs the probability of tunnelling via the Hubbard parameter J .

4.4 New intuitions and future work

In conclusion, we find that the inverted excited state can play a critical role in lifetimes and imaging fidelities. The numerical calculations of this chapter help us develop a better understanding of the behaviour of atoms in the inverted excited state. Tunneling/heating effects arising due to this phenomenon are counter-intuitive to our expectations from the Hubbard model. Deeper traps lead to faster tunnelling, and also the probability of this tunnelling doesn't depend on the motional state occupied by the atom, both results being opposite to what the Hubbard model would predict. We also observe tunnelling timescales faster than that predicted by the Hubbard model at the relevant trap depths. This further suggests that the primary tunnelling mechanism is owing to the interaction with near-resonant light either due to the recoil energy of

Chapter 4. Simulating heating rates

absorbing photons from the beam or due to heating associated with the inverted excited state. We do not observe any preferred direction of tunnelling during our imaging scheme, which suggests that the highly directional absorption of momentum from near-resonant beams may not be the primary cause of atoms tunnelling to neighbouring sites. Additionally, we gain some understanding on the primary barriers to imaging fidelity and the range of detuning and trap depths that could help to mitigate them. The work to incorporate Raman cooling and to compare against simplified experimental test cases is on-going.

This chapter also serves as a conclusion to my work involving the ^{40}K quantum-gas microscope. The following and final chapter is a result of work undertaken during the final year of my PhD on a bosonic quantum-gas microscope.

Chapter 5

Towards a ^{85}Rb quantum-gas microscope

This chapter details our work implementing Λ grey-molasses cooling for ^{85}Rb as part of a Rubidium quantum-gas microscope setup. Similar to the ^{40}K experiment, the Rb experiment aims to trap neutral atoms in an optical lattice for site-resolved imaging. In contrast, however, this experiment applies the principles discussed in chapter 1 to bosonic atoms - ^{87}Rb and ^{85}Rb . The two-species Rb microscope is the result of the efforts of recent PhD graduates A. Ulibarrena [148] and I. Despard [149]. The experiment implemented site-resolved imaging for ^{87}Rb via red-molasses cooling and achieved the observation of the superfluid to Mott-Insulator transition [146] in the optical lattice. Our work detailed in this chapter builds towards incorporating the second species of ^{85}Rb for a more versatile bosonic quantum simulator.

The atomic species ^{85}Rb comes with a key advantage - Feshbach resonances to tune the ^{85}Rb - ^{85}Rb [150] and ^{85}Rb - ^{87}Rb [151] interaction strengths by tuning the magnetic field experienced by the atoms. ^{85}Rb atoms at zero external field experience an attractive interaction that leads to the formation of molecules at typical temperatures and densities of cold-atom experiments. However, the $|F, m_F\rangle = |2, -2\rangle$ state presents a Feshbach resonance at 155 G. Moreover, the resonance is sufficiently wide (~ 10.7 G), which is orders of magnitude broader than the level of B -field precision and homogene-

ity achievable with magnetic coils in our experiment. Utilizing magnetic fields greater than 155 G [152, 153] allows for positive scattering lengths and repulsive inter-atomic interactions - key to Bose-Einstein condensation [154–157] of ^{85}Rb and the regime of strongly-correlated many-body physics [158, 159]. Additionally, there exists an accessible inter-species (between ^{85}Rb and ^{87}Rb atoms) resonance near 267 G, essential to exploring the rich phase diagram for two-component Bose-Hubbard systems. Particularly of interest are magnetic ordering effects such as the z-Neel phase deep in the Mott regime and the impact of magnetic ordering on the MI-SF transition [160, 161]. Realising the two-component Hubbard system with two isotopes of Rubidium rather than two magnetic-states of the same isotope leads to several advantages. Most notably, as the two isotopes have different optical coupling strengths for a given wavelength of incident light, we can configure optical lattices with different isotope-dependent hopping to neighbouring sites. This corresponds to spin-dependent tunneling in the Bose-Hubbard model, which is difficult to achieve with two magnetic states of the same isotope. Additionally, we can readily control and fix the magnetization, i.e., the ratio of n_{\uparrow} and n_{\downarrow} states in the optical lattice by changing the ratio of ^{85}Rb and ^{87}Rb atoms loaded into the lattice. Lastly, it is significantly easier to achieve spin-dependent detection when utilizing different isotopes which have different resonant optical transition wavelengths as opposed to magnetic states of the same isotope which would be indistinguishable to imaging light.

5.1 Experimental setup

For complete details on the components and implementation of the bosonic QGM, we refer the reader to A. Ulibarrena’s thesis [148] and the thesis of I. Despard [149]. We summarize in brief the experimental setup which bears resemblances to section 1.4 of chapter 1 of this thesis.

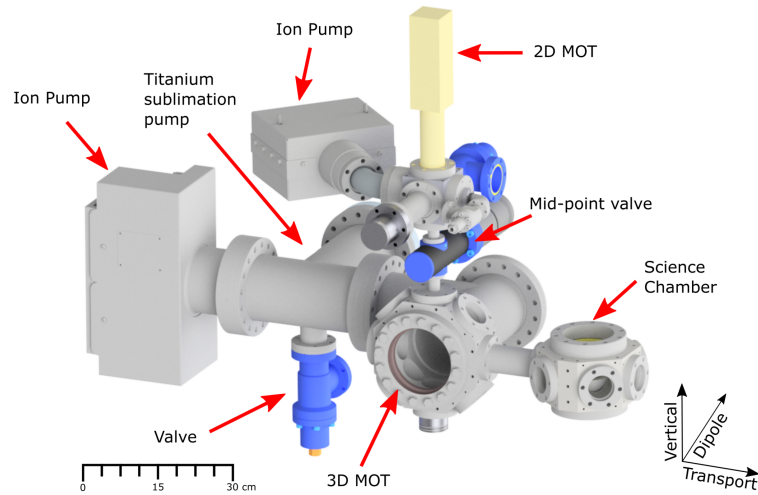


Figure 5.1: 3D rendering of Rb experiment, reproduced from [149]

Rubidium atoms at their natural abundances (72% ^{85}Rb , 28% ^{87}Rb) diffuse from an oven at 40 °C to a 2D-MOT chamber that is located directly above a 3D-MOT chamber. While for the discussion in this chapter the MOTs are tuned for ^{85}Rb , it is intended in future that both species will be simultaneously trapped and cooled in the same experimental setup. The long axis of the 2D-MOT is aligned with the vertical axis and the 3D-MOT such that a near-resonant push beam loads 10^9 atoms from the 2D-MOT to the 3D-MOT through a differential-pumping tube. Atoms reach a temperature of 200 μK in the MOT and are further cooled via 30 ms red-molasses cooling and 1.5 ms Λ grey-molasses cooling to reach 3.5 μK . The implementation and characterization for the final step of Λ grey-molasses makes section 5.2 of this chapter.

In the case of ^{87}Rb atoms, the experimental procedure is very similar up to the grey-molasses cooling stage. Beyond this stage, we can load ^{87}Rb atoms in a crossed optical-dipole trap (CODT) comprising two 200 W beams at an angle of 17°. This CODT is evaporated to load a tightly-focused dimple beam to transport atoms to the lattice chamber, where similar to the ^{40}K experiment a 2D sample of atoms are trapped and imaged in an optical lattice. In the case of ^{85}Rb , before loading into the CODT, we require to configure magnetic coils capable of providing ~ 165 G fields (where ^{87}Rb atoms are non-interacting with each other) for several seconds. The necessary coil is in the process of being installed and characterized [162]. A magnetic coil was also installed

between the 3D-MOT and lattice chambers during the building of the setup such that 165 G fields can be maintained during optical transport of the atoms between the two chambers.

Where the ^{87}Rb and ^{85}Rb experiment differs from that of ^{40}K is in its quick cycle times. It aims to be five times faster than the ^{40}K experiment for cooling to the degenerate quantum-gas regime. The experiment has achieved Bose-Einstein condensates of ^{87}Rb in a cycle time of 10 s in the 17°CODT in the 3D-MOT chamber [149]. The final step to BEC is performed all-optically, evaporating atoms in an optical trap composed of the CODT and a tightly focused dimple trap aligned at the centre of the CODT. In this configuration, we evaporate to BEC in a mere four seconds. The 2D-MOT chamber being placed vertically above the 3D-axis allows for a more compact setup (see figures 2.1, 5.1). In addition, this enables easier optical and physical access to the chambers, including for the magnetic coils necessary to generate near 165 G fields to manipulate the interaction strength of ^{85}Rb via Feshbach resonance.

At the time of writing this thesis, site-resolved imaging (via molasses cooling) of a 2D Mott-insulator of ^{87}Rb has been accomplished (subject of I. Despard's thesis [149]). As part of building towards two-species capabilities, we implemented Λ grey-molasses cooling of ^{85}Rb , which has not previously been demonstrated. Figure 5.2 depicts the level diagram for the D2 transitions and the targeted transitions for the MOT (figure 5.2a) and Λ grey-molasses cooling scheme (figure 5.2b). The separation of hyperfine ground states ^{85}Rb is 3 GHz as compared to 6.8 GHz for ^{87}Rb . We are able to use the same laser system as for ^{87}Rb which is a primary reference laser locked via polarization spectroscopy to the D2 transitions of ^{85}Rb in conjunction with a cooling and a repumping laser offset locked from the primary laser (see section 3.4 of A. Ulibarrena's thesis [148] for a full description of the laser system setup for ^{87}Rb). We require separate microwave antennae to drive transitions between the hyperfine ground states of ^{85}Rb as the antennae for ^{87}Rb are not efficient at driving frequencies near 3 GHz.

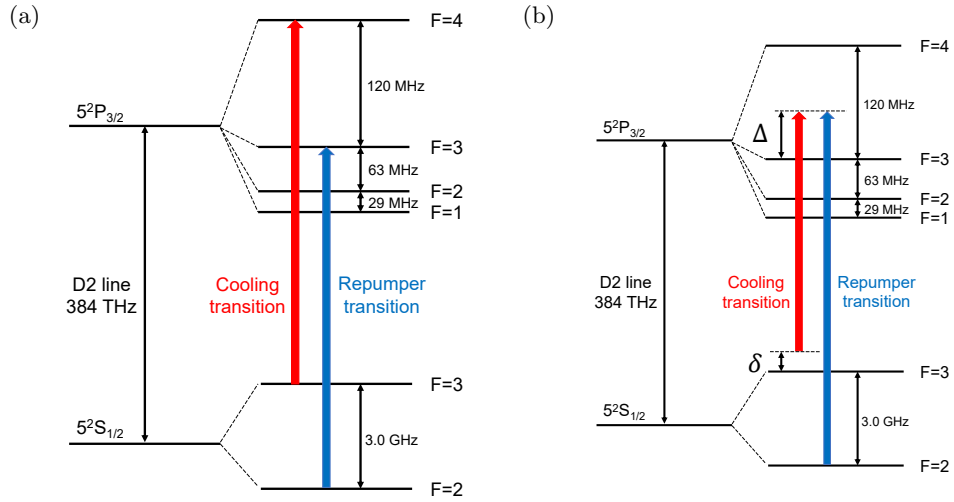


Figure 5.2: D2 transition level diagram of ^{85}Rb and cooling/repumping transitions for (a) MOT lasers and (b) Λ grey-molasses lasers, adapted from [162].

5.2 Grey-molasses cooling

In the Λ grey-molasses cooling scheme, two phase-coherent lasers - the cooling and repumping lasers - are blue detuned by Δ from the same internal state ($F' = 3$) as shown in figure 5.2b. The lasers are far enough detuned such that $F' = 3$ serves as a virtual excited state in a Λ system involving the ground states $F = 3$ and $F = 2$. In this configuration, coherent population trapping (CPT) [163] occurs that creates a dark state composed of a mixture of the $F = 3$ and $F = 2$ states. Furthermore, this dark state is velocity selective (similar to [164, 165]) i.e., atoms in this state near zero velocity are dark to both beams whereas faster moving atoms oscillate into “bright” states. The photon recoil from spontaneous decay allows for a random walk across momentum space until the atoms find the zero momentum dark state. Hence, atoms accumulate in the slow dark state over time [166, 167], which can be understood as an optical pumping effect in translation space [168]. This technique has previously been studied for several atomic species, including ^{87}Rb [169], ^{133}Cs [170], ^7Li [171], ^{39}K [172] and ^{40}K [173]. In the following section we demonstrate the implementation and results

of this cooling scheme for ^{85}Rb .

5.2.1 Implementation

An extended-cavity diode laser (ECDL) is offset locked near the $F = 3 \rightarrow F' = 4$ transition in case of MOT cooling and near the $F = 3 \rightarrow F' = 3$ transition during Λ grey molasses cooling. The light from the ECDL is passed through a fibre electro optical modulator (EOM) to generate repumper light at the appropriate relative detuning (~ 3 GHz) and relative power ($\sim 1/10^{\text{th}}$ the cooling beam power) in the same beam path. This power imbalance ensures the dark state has largely $F = 2$ character, making it darker to cooling light. This beam is amplified via a tapered amplifier (TA) to achieve the necessary power for the MOT (~ 300 mW in the bimodal beam).

The microwave signal that drives the EOM is branched off from the same amplifier circuit that powers the microwave antennae in the 3D-MOT chamber and lattice chamber. The ^{85}Rb and ^{87}Rb sequences share the same signal generator (as shown in figure 5.3). A high-pass filter (HPF) in the ^{85}Rb path and a low-pass filter (LPF) in the ^{87}Rb path allow the signal generator to switch between the necessary frequencies (3 GHz for ^{85}Rb and 0.5 GHz for ^{87}Rb path) without any change to the circuit. The 0.5 GHz signal in the ^{87}Rb path is mixed with a 6.3 GHz signal to provide the necessary frequency offset between the cooling and repumping beams. This step is not necessary for the ^{85}Rb path as the microwave signal generator is capable of frequencies up to 4 GHz. $50\ \Omega$ directional couplers protect the amplifiers from back reflections of the signal. The ^{85}Rb and ^{87}Rb paths are combined again and the resultant signal serves as the input to the EOM. Generating the repumper light through the EOM ensures that the polarizer and repumper beams are phase coherent which is the most efficient configuration for the Λ grey-molasses cooling scheme. The amplitude of the microwave signal driving the EOM sets the fraction of repumper light in the modulated beam.

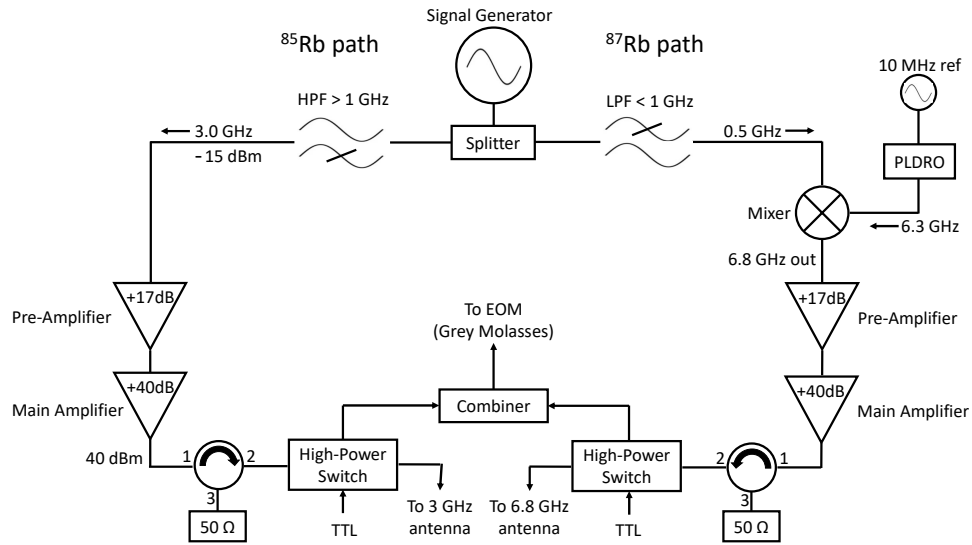


Figure 5.3: Circuit diagram depicting microwave signal generation, amplification, and input to microwave antennae/EOM for ^{87}Rb and ^{85}Rb , reproduced from [162].

Scanning the two-photon detuning (the detuning of the two-photon transition from $F = 3$ to $F = 2$ ground states) against the width of the atom cloud (figure 5.4) for Λ grey molasses cooling presents a characteristic profile shaped similar to a Fano resonance [172]. Increasing the global detuning (the shared single-photon detunings from $F = 3$, $F = 2$ to the $F' = 3$ excited state) leads to a smaller (i.e. colder) cloud by reducing single-photon scattering events that can heat the atom out of the dark state.

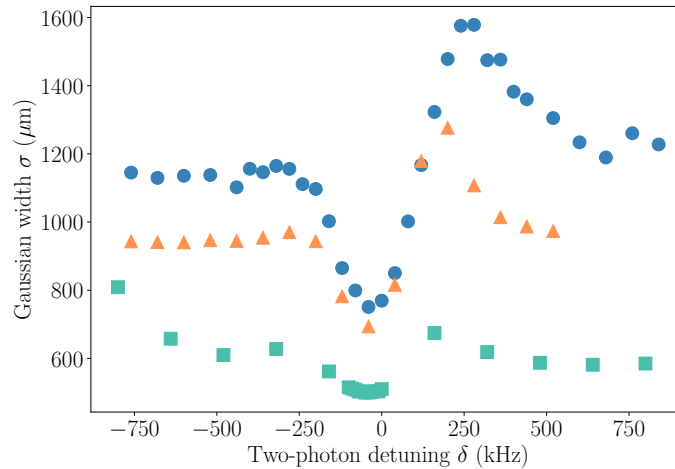


Figure 5.4: ^{85}Rb atom cloud width as a function of two-photon detuning, plotted for varying global detunings: 1.64Γ (blue circles), 2.47Γ (orange triangles) and 4.94Γ (cyan squares) where $\Gamma = 6.066\text{ MHz}$.

Demonstration of cooling

While in figure 5.4 we used the width of the cloud after TOF expansion as a proxy for temperature, we take a closer look at the behaviour of the cooling scheme in figure 5.5. The temperature measurements after 1 ms of the Λ grey-molasses pulse at the single-photon detuning $\Delta = 1.64\Gamma$ demonstrate a Fano-like profile. The atoms are initially cooled to $20\ \mu\text{K}$ via standard red-molasses cooling. This is followed by the grey-molasses pulse where we scan the two-photon detuning. We see that the scheme begins to heat atoms for two-photon detuning $\delta > 0$. The coldest temperatures are achieved slightly below $\delta = 0$, contrary to the expectation that this scheme is most efficient on resonance. We expect this arises due to differential light shifts experienced by the $F = 3$ and $F = 2$ hyperfine states arising from the power imbalance between the cooling ($F = 3$ to $F' = 3$ transition) and repumping beams ($F = 2$ to $F' = 3$ transition) that shift the true resonance point by a few 10s of kHz.

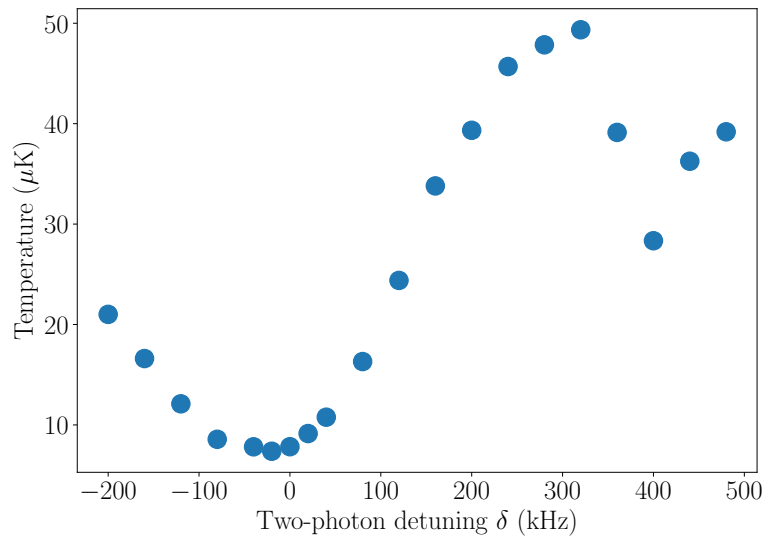


Figure 5.5: Temperature of ^{85}Rb atoms after $1\ \mu\text{s}$ of Λ grey molasses at varying two-photon detuning (global detuning $\Delta = 1.64\Gamma$).

The most efficient cooling was found at $\Delta = 5\Gamma$ with an intensity ratio of 10:1 between the cooling and repumping beams. With a 1.5 ms of the Λ grey molasses pulse, the atoms are cooled from $20\ \mu\text{K}$ to $3.5\ \mu\text{K}$ (figure 5.6). This is similar to the $4\ \mu\text{K}$ temperatures achieved for ^{87}Rb with this technique [169].

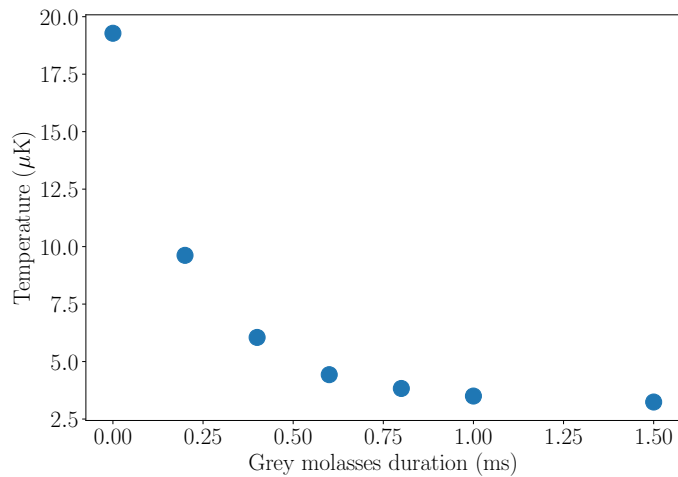


Figure 5.6: Temperature of ^{85}Rb atoms at varying durations of Λ grey molasses pulse. Two-photon detuning $\delta = 2\pi \times -50\ \text{kHz}$, global detuning $\Delta = 5\Gamma$.

Following Λ grey-molasses cooling, we could load the atoms into a crossed optical-dipole trap using the same beams as for ^{87}Rb . However, owing to the negative scattering length between ^{85}Rb atoms at zero field, the dense optical trap suffer from short lifetimes (~ 3 s), and condensates above a small critical number of atoms are unstable. To overcome this challenge, it is required to generate a bias field of ~ 165 G, near a zero crossing of the scattering length owing to the Feshbach resonance at 155 G. Doing so would increase the atom lifetimes in the trap by an order of magnitude, and allow the creation of ^{85}Rb BECs with tuneable interactions [157].

5.3 Optical pumping for ^{85}Rb

Finally, an optical pumping scheme is implemented to prepare ^{85}Rb in the $|F, m_F\rangle = |3, -3\rangle$ state. Immediately after grey-molasses cooling at zero field, the atoms populate all m_F levels in the $F = 3$ state. A magnetic field of 0.53 G is applied to Zeeman-shift the ground state m_F levels out of degeneracy. The resulting energy shift from the hyperfine splitting of transitions between m_F levels in the $F = 3$ and $F' = 2$ states are

$$\Delta E = (m_F + m_{F'}) \Delta_0 \quad (5.1)$$

where $\Delta_0 = 2\pi \times 250$ kHz is the Zeeman-shift for the $m_F = 1$ state at this applied field and m_F and $m_{F'}$ correspond to the sublevels of the $F = 3$ and $F' = 2$ states respectively. As m_F and $m_{F'}$ values range from $[3, -3]$ and $[2, -2]$, there exist ten possible transition energies between m_F levels from $F = 3$ to $F' = 2$, each separated by ΔE_0 .

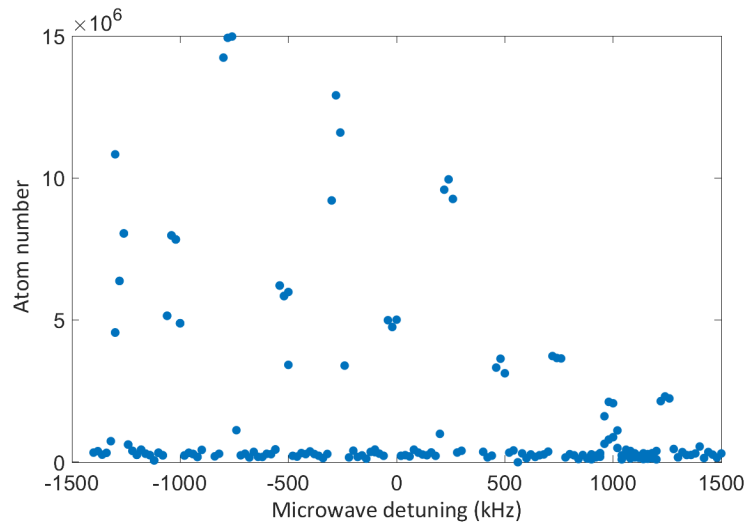


Figure 5.7: ^{85}Rb atom number transferred to $F = 2$ hyperfine level for applied microwave pulse detuning.

A microwave antenna (figure 5.3) placed near the 3D-MOT chamber drives transitions between the hyperfine ground states of ^{85}Rb with a Rabi frequency of $2\pi \times 4.3$ kHz. As the microwave pulses are linearly polarized, the allowed transitions correspond to a change in m_F such that

$$\Delta m_F = m_F - m_{F'} = 0, \pm 1. \quad (5.2)$$

The 10 possible transition frequencies are observed in figure 5.7 on scanning the centre frequency of the microwave pulse (where zero detuning corresponds to the un-shifted hyperfine splitting of ^{85}Rb ground states of 3.035 GHz).

The atom cloud is then illuminated with $\sigma-$ polarized light near-resonant to the $F = 3$ to $F' = 4$ transition. This polarization favours transitions from $m_F \rightarrow m_F - 1$, leading to an accumulation of atoms in the $|3, -3\rangle$ state (figure 5.8). A $\sigma-$ polarized repumper beam resonant to the $F = 2$ to $F' = 3$ transition preserves atoms in the $F = 3$ manifold.

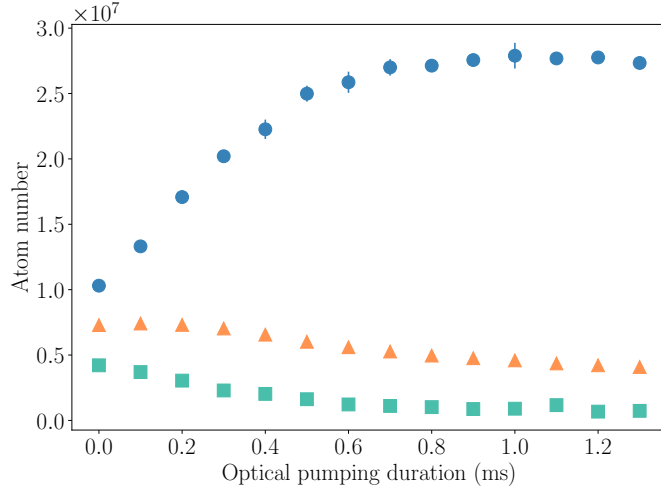


Figure 5.8: ^{85}Rb optical pumping: pulse duration and resulting atom population in states $|F, m_F\rangle = |3, -3\rangle$ (blue circles), $|3, -2\rangle$ (orange triangles) and $|3, -1\rangle$ (cyan squares).

For the state-selective measurements of the atom population presented in figure, 5.8, we utilize microwave transitions between the m_F levels of the $F = 3$ and $F = 2$ hyperfine ground states similar to the microwave spectra of figure 5.7. At an applied magnetic field of 0.53 G, the transition between $|3, -3\rangle$ and $|2, -2\rangle$ is red-shifted 1.25 MHz from the hyperfine splitting at zero field. To measure atom number in the $m_F = -3$ state, we red-detune the microwave pulse by 1.25 MHz, allowing us to selectively excite this transition. We can deterministically transfer nearly all atoms in the selected m_F level by using a 10 ms adiabatic microwave passage (ramping the frequency slowly across the resonance). A resonant cooling pulse targeting the $F = 3$ to $F' = 4$ transition heats away atoms still remaining in the $F = 3$ state. We can then apply the same microwave pulse to restore atoms to the $F = 3$ manifold or use repumping light to image atoms transferred to the $F = 2$ state. The same procedure with the microwave detuning at 1 MHz provides us with the $|3, -2\rangle$ population. To measure the $|3, -1\rangle$ population, we cannot directly apply a microwave pulse resonant to the $|3, -1\rangle$ to $|2, -2\rangle$ transition as this would also drive the $|3, -2\rangle$ to $|2, -1\rangle$ transition (according to equation 5.1 and the microwave selection rules 5.2). Instead, we first apply an adiabatic transfer pulse at 1 MHz to transfer atoms in the $|3, -2\rangle$ state to the $|2, -2\rangle$ state. We then apply

a 750 kHz pulse to exchange the atom population in the $|3, -1\rangle$ and $|2, -2\rangle$ sublevels, transferring the atoms in the $|3, -1\rangle$ state to the $F = 2$ manifold (where they are protected from the subsequent heating pulse on the $F = 3$ to $F' = 4$ cycling transition) while keeping atoms originally in the $|3, -2\rangle$ state in the $F = 3$ manifold.

5.4 Future work

The next stage for the Rb experiment is to take advantage of the intra-species Feshbach resonance of ^{85}Rb at 155 G and the inter-species resonance between ^{85}Rb and ^{87}Rb at 267 G. This calls for the implementation of various upgrades to the experiment's capabilities that have been in development for the past few months. First is the implementation of three magnetic coils that would be positioned at the 3D-MOT chamber, science chamber and between the 3D-MOT and science chambers [162]. In conjunction, this would maintain the necessary magnetic fields (near the Feshbach resonance) at the atoms at every all-optical stage of the experiment. Second is the implementation of a digital micro-mirror device (DMD) [174] aligned along the path of the high-resolution microscope aimed at the science chamber. The DMD is an array of microscopic mirrors that correspond to pixels in the image plane. Each mirror can be individually controlled to project a 'bright' or 'dark' pixel, i.e., reflecting light along the imaging path or deflecting to a beam dump [175]. In addition, the DMD can reduce the effective intensity of light at each pixel by rapidly switching between bright/dark states. Hence, this device enables us to generate arbitrary (time-averaged) optical potentials [176,177] at the focus of the microscope in the optical lattice. This capability along with the tunability offered by the inter-species Feshbach resonance will play a key role in exploring the phase diagram of two-component Bose-Hubbard systems [160,178,179] and more exotic many-body phenomenon [180,181].

Chapter 6

Conclusions and outlook

During my PhD, I had the opportunity to work on two different and equally complex experiments spanning three species of atoms - primarily ^{40}K , yet also ^{87}Rb and ^{85}Rb . In both experiments we believe we have made progress in developing techniques for cold atom experiments and enabling future research on quantum many-body dynamics.

In case of ^{40}K , we implemented Raman sideband cooling and studied its advantages and challenges, particularly as it compares to the EIT technique. With 1 s Raman cooling pulses, we achieve $\sim 5\%$ atom loss between successive images of the same atom sample. I have also studied numerically the heating effect of the inverted excited state of ^{40}K . These techniques have been applied towards solving a narrow set of problems (i.e. single-atom imaging of ^{40}K atoms). However, the lessons we have learned in the process aid in the development of the broadly applicable techniques of Raman sideband cooling, EIT cooling and quantum Monte-Carlo simulations. Our characterizations of single-atom imaging using Raman cooling and EIT cooling is valuable to better understand these important techniques as well as in designing and optimizing quantum-gas microscope experiments. Our work simulating the imaging scheme showcases the strengths of the quantum trajectory technique for time-evolution of quantum systems with large Hilbert spaces. We have gained valuable insights into the limitations of site-resolved imaging ^{40}K . Moreover, we hope the approach we have used makes the quantum trajectory technique more accessible to experiments interested in the dynamics of atom-light systems. In the case of ^{85}Rb , there is no published work (as of the

writing of this thesis) on implementing the grey-molasses scheme, and this work fills this gap in the literature and contributes to this vitally important sub-doppler cooling scheme. We achieve atom temperatures of $3.5\ \mu\text{K}$ with a $1.5\ \text{ms}$ of Λ grey-molasses cooling, a significant improvement over typical red-molasses temperatures of $20\ \mu\text{K}$.

Most important, both the fermionic and bosonic experiments are positioned for novel research in quantum many-body physics. We have achieved sufficient imaging fidelity of ^{40}K to explore the Fermi-Hubbard model with single-site resolution and serve as a valuable investigative tool into strongly-correlated systems. The Rb experiment with the newly added capability of trapping and cooling ^{85}Rb is in range of its final aim as a dual species bosonic quantum-gas microscope with tunable interactions.

Appendix A

Discussion of lattice potentials

The following is a semi-classical approach to energy levels of atoms in a lattice trap. In particular, we discuss the structure of the target lattice potential in 1D is of the form $U = U_0 \sin^2(k_L x)$ where k_L is the lattice wave-vector $k_l = 2\pi/\lambda_L$. We find the Taylor expansion of this potential near $x = 0$ to be

$$U = U_0 \left(k_L^2 x^2 - \frac{1}{3} k_L^4 x^4 + \frac{2}{45} k_L^6 x^6 \dots \right). \quad (\text{A.1})$$

We restrict our discussion to the 1st and 2nd non-zero terms in the Taylor expansion. The 1st term can be treated as a Harmonic potential (see figure A.1):

$$U_0 k_L^2 x^2 = \frac{1}{2} m \omega_T^2 x^2, \quad (\text{A.2})$$

$$\omega_T = \sqrt{\frac{2U_0 k_L^2}{m}}. \quad (\text{A.3})$$

Note that ω_T is linked to the depth of the lattice potential, U_0 , also referred to as trap depth. Since it is a physically measurable quantity, we will prefer to quantify the trap depth in terms of the corresponding trap frequency ω_T rather than in Lattice recoil units (E_r^L). A lattice depth of $1400 E_r^L$ corresponds to a trap depth (or trap frequency) of $\omega_T = 2\pi \times 330$ kHz. Thus along with their electronic states, atoms also have a motional state associated with the Harmonic oscillator potential they are trapped in,

Appendix A. Discussion of lattice potentials

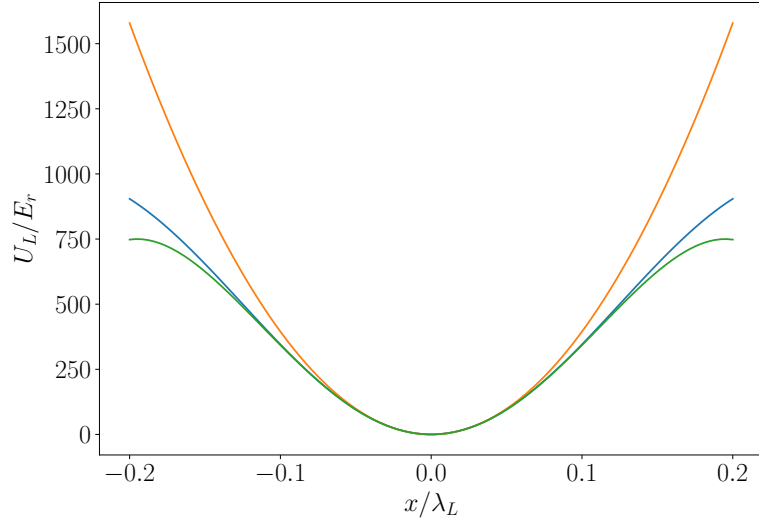


Figure A.1: Comparing lattice potential $U_L = U_0 \sin^2(k_L x)$ (blue), 1st term of U_L Taylor expansion - $U_{HO} = m\omega^2/2$ (orange) and sum of 1st and 2nd terms (green).

typically numbered from lower to higher energy $|0\rangle$, $|1\rangle$, $|2\rangle$ and so on. The eigenenergy of motional state $|n\rangle$ is $(n + 1/2)\hbar\omega_T$. The eigenstates of atoms in a harmonic potential take the form of Hermite polynomials in position space. It can be shown that for atoms in a state $|\psi(t)\rangle$, the state evolves such that

$$\psi(nT) = e^{i\phi}\psi(0). \quad (\text{A.4})$$

Here, $T = 2\pi/\omega_T$, n is an integer and $|\psi\rangle$ a phase factor between $[0, 2\pi]$. i.e. the state observables oscillate with a time period set by the trap frequency.

Ideally, the trap frequencies experienced by all atoms in our image would be identical, and the trap describing each well would be purely harmonic, ensuring equal spacing between motional energy levels. However, due to experimental limitations, inhomogeneities arise across the trap. Such inhomogeneities could lead to spatial inhomogeneity in our images. Earlier estimates showed that the largest source of inhomogeneity of frequencies (~ 40 kHz) across the $150 \times 150 \mu\text{m}$ image was the radial Gaussian profile of the lattice beams (see Table 3.1).

Another key source of spectral aberrations is the anharmonicity of each individual potential well of the lattice, which we will discuss in detail below. The motivation

Appendix A. Discussion of lattice potentials

for these calculations were to answer two questions : 1. Would lowering the depth of the lattice potential reduce anharmonicity, and hence spectral averrations at individual lattice sites? 2. For our current parameters, having a transition width during imaging of ~ 50 kHz how many harmonic oscillator (motional) energy levels are resonant to Raman sideband cooling?

Anharmonicity term

The second term of the potential $U = U_0(k_L^2 x^2 - 1/3k_L^4 x^4 + \dots)$ is the anharmonicity, i.e., a deviation in the Harmonic oscillator energy level spacing (see Figure A.1). For $\Delta U = -1/3U_0k_L^4\hat{x}_4$, we take the expectation value to find the energy difference between the expected Harmonic energy levels (treating it as a perturbative correction).

$$\Delta E_n = -\frac{1}{3}U_0k_L^4\langle\hat{x}^4\rangle \quad (\text{A.5})$$

For a harmonic oscillator, $\hat{x} = x_0(\hat{a} + \hat{a}^\dagger)$ where \hat{a} and \hat{a}^\dagger are the lowering and raising operators respectively. Therefore:

$$\hat{x}^4/x_0^4 = b + \hat{a}\hat{a}\hat{a}^\dagger\hat{a}^\dagger + \hat{a}^\dagger\hat{a}^\dagger\hat{a}\hat{a} + \hat{a}^\dagger\hat{a}\hat{a}^\dagger\hat{a} + \hat{a}\hat{a}^\dagger\hat{a}\hat{a}^\dagger + \hat{a}^\dagger\hat{a}\hat{a}\hat{a}^\dagger + \hat{a}\hat{a}^\dagger\hat{a}^\dagger\hat{a} \quad (\text{A.6})$$

Here, b includes all the terms with unequal powers of \hat{a} and \hat{a}^\dagger and thus have zero expectation value. Equation A.6 can be term-wise evaluated to show that:

$$\langle\hat{x}^4\rangle_n = x_0^4(6n^2 + 6n + 3) \quad (\text{A.7})$$

Note, n is the motional state number of the Harmonic oscillator levels. The difference in energy of a motional level $|n\rangle$ from its expected harmonic energy of $(n + 1/2)\hbar\omega$ is therefore:

$$\Delta E_n = -\frac{1}{3}U_0k_L^4x_0^4(6n^2 + 6n + 3) \quad (\text{A.8})$$

Appendix A. Discussion of lattice potentials

The transition energies ϵ_n (i.e. the energy difference between successive levels n and $(n - 1)$) are:

$$\epsilon_{(n \rightarrow n-1)} = \hbar\omega_T - U_0 k_L^4 x_0^4 (2n^2 + 2n + 1 - (2(n-1)^2 + 2(n-1) + 1)) \quad (\text{A.9})$$

$$= \hbar\omega_T - U_0 k_L^4 x_0^4 (4n) \quad (\text{A.10})$$

We make the required substitutions $x_0 = \sqrt{\hbar/2m\omega_T}$, $U_0 k_L^2 = m\omega_T^2/2$. We also note that the first term in the expression of ϵ_n is the Harmonic oscillator energy independent of n which we subtract to have $\Delta\epsilon_n = \epsilon_n - \hbar\omega$ and find:

$$\Delta\epsilon_{(n \rightarrow n-1)} = \frac{(\hbar k_L)^2}{8m} (4n) \quad (\text{A.11})$$

Recognizing that $(\hbar k_L)^2/2m$ is the lattice recoil energy E_r^L , we have:

$$\Delta\epsilon_{(n \rightarrow n-1)} = nE_r^L \quad (\text{A.12})$$

The calculation above suggests that the anharmonicity of the trap is independent of the trap frequency ω to first order. More explicitly, the energy separation of motional states $|1\rangle \rightarrow |0\rangle$ is $(\hbar\omega - 1 E_r^L)$, the energy separation $|2\rangle \rightarrow |1\rangle$ is $(\hbar\omega - 2 E_r^L)$, and so on. Thus we have indications that lowering the lattice depth would not reduce spectral aberrations in our system, and that for a Rabi frequency of ~ 10 kHz we would be resonant to two transitions, namely - $|1\rangle \rightarrow |0\rangle$ and $|2\rangle \rightarrow |1\rangle$. (The lattice recoil energy E_r^L for 1064 nm lattice beams and ^{40}K atoms is calculated to be approximately 4.4 kHz).

Appendix B

Sideband transitions and the Lamb-Dicke parameter

Light-atom interactions typically cause transitions between electronic states. However, when atoms are trapped in a harmonic trap, they can simultaneously cause transitions between the harmonic oscillator levels. We refer to them as sideband transitions. In the regime where the sidebands are well resolved (i.e., the trap frequency is greater than the Rabi frequency corresponding to the strength of the electronic transition), the motional and electronic degrees of freedom are separated. Thus we may write the state of the system as $|\Psi_{i,n}\rangle = |\psi_i, n\rangle$, where $|\psi_i\rangle$ refer to the internal/electronic states and $|n\rangle$ the motional states. Thus the carrier transition would be from $|\psi_1, n\rangle \rightarrow |\psi_2, n\rangle$ and sideband transitions would be from $|\psi_1, n\rangle \rightarrow |\psi_2, n'\rangle$ where $n \neq n'$. Since motional energy states are separated by $\Delta E = \omega_T$ in harmonic traps, the frequency separation between the peak of the carrier transition and the peak of the 1st sideband transitions ($n' = n \pm 1$) is ω_T . The strength for a dipole transition between electronic states is given by:

$$\hbar\Omega_0 = \langle\psi_2|\vec{d}\cdot\vec{E}|\psi_1\rangle. \quad (\text{B.1})$$

\vec{d} is the induced atomic dipole moment, \vec{E} is the electric field vector of incident light. $\vec{E} = E_0 e^{i(\vec{k}\cdot\vec{x} - \omega_L t)}$. Ω_0 is known as the Rabi frequency, and for a laser detuned from

Appendix B. Sideband transitions and the Lamb-Dicke parameter

resonance by Δ , the generalized Rabi frequency $\Omega_R = \sqrt{\Omega_0^2 + \Delta^2}$. For purely electronic transitions (i.e., carrier transitions) we consider that the size of the atom is much smaller than the wavelength of optical light. Thus the atom effectively experiences an electric field oscillating at frequency ω_L and the spatial variation of the electric field can be ignored. For sideband transitions, (the coupling between motional levels) the spatially varying component of the electric field provides the necessary momentum transfer. As demonstrated in section 3.1.1, the coupling strength of red-sideband transitions is of the form:

$$\Omega_{RSB} = \eta\sqrt{n}\Omega_R. \quad (\text{B.2})$$

Similarly, it can be shown that for blue-sideband transitions, the coupling strength is

$$\Omega_{BSB} = \eta\sqrt{n+1}\Omega_R. \quad (\text{B.3})$$

Here, the Lamb-Dicke parameter [182] is $\eta = kx_0$ (in the x-axis), where k is the wavenumber of incident light and x_0 is the characteristic length of the harmonic trap, equal to $\sqrt{\hbar/2m\omega_T}$. The Lamb-Dicke parameter can be re-written as

$$\eta = \sqrt{\frac{(\hbar k)^2/2m}{\hbar\omega_T}} = \sqrt{\frac{E_r}{E_T}}. \quad (\text{B.4})$$

I.e., the Lamb-Dicke parameter is the square root of the ratio between the recoil energy $E_r = (\hbar k)^2/2m$ and the energy separation between harmonic oscillator levels $E_T = \hbar\omega_T$. When an atom in an excited state decays to the ground state while emitting a photon (with linewidth $\Gamma \gg \hbar\omega_T$), the Lamb-Dicke parameter describes the probability of the atom gaining or losing a motional quanta of energy due the recoil energy from scattering a photon.

$$P(n \rightarrow n') \propto \|\langle n' | e^{i\vec{k}\cdot\vec{x}} | n \rangle\|^2 \quad (\text{B.5})$$

Appendix B. Sideband transitions and the Lamb-Dicke parameter

The transition is broad enough that it can drive simultaneously the carrier, blue-sideband and red-sideband transitions. Thus for every decay transition, the probability of gaining a motional quanta is $\eta^2(n+1)$ and the probability to lose a motional quanta is η^2n . This leads to a net probability of $\eta^2(n+1) - \eta^2(n) = \eta^2$ of gaining a motional quanta during spontaneous emission. If we are in the ‘Lamb-Dicke regime’ ($\eta \ll 1$), i.e., when the recoil energy the atoms gain from emitting a photon is far less than the energy spacing between motional states, photon emission/recoil has a low probability of changing the motional state of the atom. The probability of gaining/losing two motional energy quanta in this transition ($n' = n \pm 2$) is of the order η^4 and is thus strongly suppressed. For typical optical transitions, $\eta = 0.1$. Hence, we can usually ignore higher order sideband transitions. The Lamb-Dicke parameter also describes the coupling strength of the sideband transitions relative to the carrier transition Ω_R (equation B.2 and B.3). This is why in our experiment we require two-photon optical transitions to couple between ground states only 1.28 GHz apart. The recoil energy from a microwave photons are an order of magnitude too small to drive any appreciable cooling transitions, i.e., microwave photons would be deep in the Lamb-Dicke regime for our imaging lattices and unable to change the motional level of the atom.

To find the Lamb-Dicke parameter associated with the two-photon Raman transitions, η_R , we need to consider the net recoil energy. The momentum change from the two-photon transition is described by $\Delta\vec{k} = \pm\vec{k}_1 + \vec{k}_2$ where \vec{k}_1 and \vec{k}_2 are the wavevectors associated with the individual Raman beams. In our experiment correspond this corresponds to D2 photons. As the two Raman beams are orthogonal, however, the total momentum kick is greater than the single D2 photon momentum by a factor $\sqrt{2}$. Furthermore, as the beam is not equally aligned to every lattice axis, the projection of the resultant vector on the vertical, east and west axes have relative magnitude $1/\sqrt{2}$, $1/2$ and $1/2$ respectively. Accordingly, we find that η_R is different along the vertical axis as compared to the horizontal axes. For typical imaging trapping frequencies of $2\pi \times 300$ kHz that corresponds to $\sim 1000 E_r$, we observe Lamb-Dicke parameters of 0.17 and 0.12 respectively for the vertical and horizontal axes B.1. Accordingly, the Raman transition strength in the vertical axis is higher than along the horizontal axes.

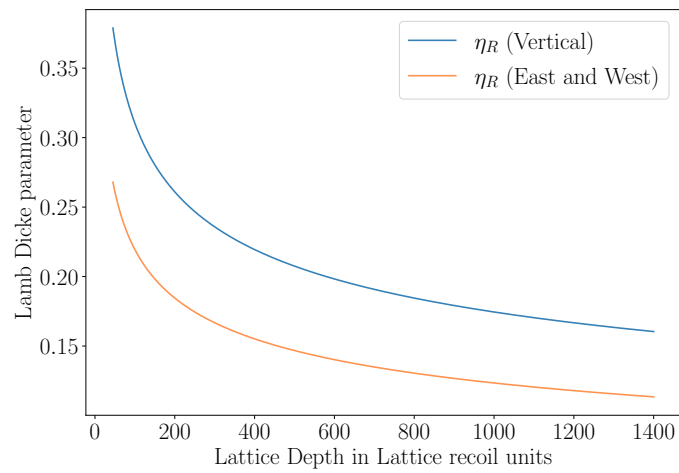


Figure B.1: Lamb-Dicke parameter in the vertical (blue) and horizontal axes (orange) as a function of lattice depth.

Bibliography

- [1] Heike Kamerlingh-Onnes. Investigations into the properties of substances at low temperatures, which have led, amongst other things, to the preparation of liquid helium, 1913.
- [2] Walther Meissner and Robert Ochsenfeld. Ein neuer effekt bei eintritt der supraleitfähigkeit. *Naturwissenschaften*, 21(44):787–788, 1933.
- [3] Rainer Wesche. High-temperature superconductors. In *Springer Handbook of Electronic and Photonic Materials*, page 1. 2017.
- [4] Hanno Essén and Miguel C N Fiolhais. Meissner effect, diamagnetism, and classical physics—a review. *American Journal of Physics*, 80(2):164–169, 2012.
- [5] J. Bardeen, L. N. Cooper, and J. R. Schrieffer. Theory of superconductivity. *Physical Review*, 108(5):1175–1204, 1957.
- [6] Anthony James Leggett. *Quantum Liquids*. Oxford University Press, September 2006.
- [7] J. N. Rjabinin and L. W. Shubnikow. Magnetic properties and critical currents of supraconducting alloys. *Nature*, 135(3415):581–582, 1935.
- [8] Alexei A Abrikosov. Type II superconductors and the vortex lattice. *Nobel Prize Lectures*, 2004.
- [9] B. Keimer, S. A. Kivelson, M. R. Norman, S. Uchida, and J. Zaanen. From quantum matter to high-temperature superconductivity in copper oxides. *Nature* 2015 518:7538, 518(7538):179–186, 2015.

Bibliography

- [10] J G Bednorz and K A Miiller. Condensed Possible High T_c Superconductivity in the Ba-La-Cu-O System. *Z. Phys. B-Condensed Matter*, 64:189–193, 1986.
- [11] M K Wu, J R Ashburn, C J Torng, P H Hor, R L Meng, L Gao, Z J Huang, Y Q Wang, and C. W. Chu. Superconductivity at 93 K in a new mixed-phase Yb-Ba-Cu-O compound system at ambient pressure. *Physical Review Letters*, 58(9):908–910, 1987.
- [12] D. A. Wollman, D. J. Van Harlingen, W. C. Lee, D. M. Ginsberg, and A. J. Leggett. Experimental determination of the superconducting pairing state in YBCO from the phase coherence of YBCO-Pb dc SQUIDs. *Physical Review Letters*, 71(13):2134–2137, September 1993. Publisher: American Physical Society.
- [13] W. N. Hardy, D. A. Bonn, D. C. Morgan, Ruixing Liang, and Kuan Zhang. Precision measurements of the temperature dependence of λ in YBa₂CuO_{6.95}: Strong evidence for nodes in the gap function. *Physical Review Letters*, 70(25):3999–4002, June 1993. Publisher: American Physical Society.
- [14] Z.-X. Shen, D. S. Dessau, B. O. Wells, D. M. King, W. E. Spicer, A. J. Arko, D. Marshall, L. W. Lombardo, A. Kapitulnik, P. Dickinson, S. Doniach, J. DiCarlo, T. Loeser, and C. H. Park. Anomalously large gap anisotropy in the a-b plane of Bi₂Sr₂CaCu₂O₈+. *Physical Review Letters*, 70(10):1553–1556, March 1993. Publisher: American Physical Society.
- [15] C. C. Tsuei and J. R. Kirtley. Pairing symmetry in cuprate superconductors. *Reviews of Modern Physics*, 72(4):969–1016, October 2000. Publisher: American Physical Society.
- [16] Catherine Kallin and A. John Berlinsky. Are the high T_c superconductors d-wave? *Hyperfine Interactions*, 86(1):489–503, December 1994.
- [17] Yuping Wu and Teunis van Ree. Introduction: Energy technologies and their role in our life. *Metal Oxides in Energy Technologies*, pages 1–16, 2018.

Bibliography

- [18] Vitaly L. Ginzburg. *On Superconductivity and Superfluidity: A Scientific Autobiography*. 2009.
- [19] Xingjiang Zhou, Wei Sheng Lee, Masatoshi Imada, Nandini Trivedi, Philip Phillips, Hae Young Kee, Päivi Törmä, and Mikhail Erements. High-temperature superconductivity. *Nature Reviews Physics*, 3(7):462–465, 2021.
- [20] Ben Simons. Chapter 2: Ginzburg-Landau Phenomenology. In *Phase transitions and collective phenomena*. 1997.
- [21] John Hubbard. Electron correlations in narrow energy bands. *Proceedings of the Royal Society of London. Series A. Mathematical and Physical Sciences*, 276(1365):238–257, 1963.
- [22] Dylan A. Cotta. *A single-site resolution fermionic quantum-gas microscope*. PhD thesis, University of Strathclyde, 2018.
- [23] S. N. Kaul. Low-temperature magnetization and spin-wave excitations in amorphous Ni-rich transition-metal—metalloid alloys. *Physical Review B*, 27(9):5761, 1983.
- [24] Edmund C. Stoner. Atomic moments in ferromagnetic metals and alloys with non-ferromagnetic elements. *The London, Edinburgh, and Dublin Philosophical Magazine and Journal of Science*, 15(101):1018–1034, 1933.
- [25] Marcus Ekholm. Theoretical Descriptions of Complex Magnetism in Transition Metals and Their Alloys. *PhD Thesis*, pages 1–146, 2013.
- [26] Jerry B. Torrance, Philippe Lacorre, Chinnarong Asavaroengchai, and Robert M. Metzger. Why are some oxides metallic, while most are insulating? *Physica C: Superconductivity and its applications*, 182(4-6):351–364, 1991.
- [27] E. P. Wohlfarth. The Theoretical and Experimental Status of the Collective Electron Theory of Ferromagnetism. *Reviews of Modern Physics*, 25(1):211, 1953.

Bibliography

- [28] J. H. Van Vleck. Models of Exchange Coupling in Ferromagnetic Media. *Reviews of Modern Physics*, 25(1):220, 1953.
- [29] Michael Foss-feig. *Quantum simulation of many-body physics with neutral atoms, molecules, and ions*. PhD thesis, University of Colorado, 2013.
- [30] Junjiro Kanamori. Electron Correlation and Ferromagnetism of Transition Metals. *Progress of Theoretical Physics*, 30(3):275–289, 1963.
- [31] Martin C. Gutzwiller. Effect of Correlation on the Ferromagnetism of Transition Metals. *Physical Review Letters*, 10(5):159–162, 1963.
- [32] Fabian HL Essler, Holger Frahm, Frank Göhmann, Andreas Klümper, and Vladimir E Korepin. *The one-dimensional Hubbard model*. 2005.
- [33] J. M Ziman. *Principles of the Theory of Solids*. Cambridge University Press, Cambridge, 1979. OCLC: 889948737.
- [34] Matthew P. A. Fisher, Peter B. Weichman, G. Grinstein, and Daniel S. Fisher. Boson localization and the superfluid-insulator transition. *Phys. Rev. B*, 40(1):546–570, 1989.
- [35] J. K. Freericks and H. Monien. Phase diagram of the bose Hubbard model. *Europhysics Letters (EPL)*, 26(7):545–550, 1994.
- [36] Tilman Esslinger. Fermi-hubbard physics with atoms in an optical lattice. *Annual Review of Condensed Matter Physics*, 1:129–152, 2010.
- [37] Antoine Georges. Condensed Matter Physics With Light And Atoms: Strongly Correlated Cold Fermions in Optical Lattices. *arXiv:cond-mat/0702122*, 2007.
- [38] Koji Kosuge. The phase diagram and phase transition of the V2O3-V2O5, system. *Journal of Physics and Chemistry of Solids*, 28(8):1613–1621, 1967.
- [39] C. N. R. Rao. Transition Metal Oxides. *Annual Review of Physical Chemistry*, 40(1):291–326, 1989.

Bibliography

- [40] J. Spalek. t-J Model Then and Now: a Personal Perspective from the Pioneering Times. *Acta Physica Polonica A*, 111(4):409–424, April 2007.
- [41] David Markowitz and Leo P. Kadanoff. Effect of Impurities upon Critical Temperature of Anisotropic Superconductors. *Phys. Rev.*, 131(2):563–575, 1963.
- [42] Kang Jung. The doping effects on the critical temperature of high-temperature superconductors. *Metals and Materials*, 2(4):219–226, 1996.
- [43] Dongjoon Song, Shigeyuki Ishida, Akira Iyo, Masamichi Nakajima, Jun-ichi Shimoyama, Michael Eisterer, and Hiroshi Eisaki. Distinct doping dependence of critical temperature and critical current density in $\text{Ba}_{1-x}\text{K}_x\text{Fe}_2\text{As}_2$ superconductor. *Scientific Reports*, 6(1):26671, 2016.
- [44] A. P. Durajski and R. Szczesniak. Doping dependence of critical temperature for superconductivity induced by hole-phonon interaction. *Physics Letters A*, 381(38):3332–3336, 2017.
- [45] Annabelle Bohrdt, Lukas Homeier, Christian Reinmoser, Eugene Demler, and Fabian Grusdt. Exploration of doped quantum magnets with ultracold atoms. *Annals of Physics*, 435:168651, 2021.
- [46] Fabian H. L. Essler, Vladimir E. Korepin, and Kareljan Schoutens. Complete solution of the one-dimensional Hubbard model. *Phys. Rev. Lett.*, 67(27):3848–3851, 1991.
- [47] Editorial. The Hubbard model at half a century. *Nature Physics*, 9(9):523, 2013.
- [48] John Preskill. Quantum computing 40 years later. *Feynman Lectures on Computation*, 2021.
- [49] Christina V. Kraus and J. Ignacio Cirac. Generalized Hartree-Fock theory for interacting fermions in lattices: Numerical methods. *New Journal of Physics*, 12, 2010.

Bibliography

- [50] W. M.C. Foulkes, L. Mitas, R. J. Needs, and G. Rajagopal. Quantum Monte Carlo simulations of solids. *Reviews of Modern Physics*, 73(1):33–83, 2001.
- [51] J. Carlson, Stefano Gandolfi, Kevin E. Schmidt, and Shiwei Zhang. Auxiliary-field quantum Monte Carlo method for strongly paired fermions. *Physical Review A - Atomic, Molecular, and Optical Physics*, 84(6):061602, 2011.
- [52] Artur Ekert and Peter L. Knight. Entangled quantum systems and the Schmidt decomposition. *American Journal of Physics*, 63(5):415, 1998.
- [53] Ulrich Schollwöck. The density-matrix renormalization group in the age of matrix product states. *Annals of Physics*, 326(1):96–192, 2010.
- [54] R. O. Jones. Density functional theory: Its origins, rise to prominence, and future. *Rev. Mod. Phys.*, 87(3):897–923, 2015.
- [55] Antoine Georges, Gabriel Kotliar, Werner Krauth, and Marcelo J. Rozenberg. Dynamical mean-field theory of strongly correlated fermion systems and the limit of infinite dimensions. *Rev. Mod. Phys.*, 68:13–125, Jan 1996.
- [56] J Eisert, M Cramer, and M B Plenio. Colloquium: Area laws for the entanglement entropy. *Reviews of Modern Physics*, 82(1):277–306, 2010.
- [57] Jun Kondo. Superconductivity of the 2d hubbard model with a small u . *Denshi Gijutsu Sogo Kenkyusho Iho/Bulletin of the Electrotechnical Laboratory*, 64, 11 2000.
- [58] Richard P Feynman. Simulating Physics with Computers. *International Journal of Theoretical Physics*, 21(6), 1982.
- [59] Seth Lloyd. Universal Quantum Simulators. *Science*, 273(5278):1073–1078, 1996.
- [60] D. Jaksch, C. Bruder, J. I. Cirac, C. W. Gardiner, and P. Zoller. Cold Bosonic Atoms in Optical Lattices. *Phys. Rev. Lett.*, 81(15):3108–3111, 1998.
- [61] Ivan H. Deutsch and Poul S. Jessen. Quantum-state control in optical lattices. *Physical Review A*, 57(3):1972, 1998.

Bibliography

- [62] David Deutsch. Quantum theory, the Church-Turing principle and the universal quantum computer. *Appeared in Proceedings of the Royal Society of London A*, 400:97–117, 1985.
- [63] Rudolf Grimm, Matthias Weidemüller, and Yurii B. Ovchinnikov. Optical Dipole Traps for Neutral Atoms. volume 42 of *Advances In Atomic, Molecular, and Optical Physics*, pages 95–170. 2000.
- [64] Sepehr Ebadi, Tout T. Wang, Harry Levine, Alexander Keesling, Giulia Semeghini, Ahmed Omran, Dolev Bluvstein, Rhine Samajdar, Hannes Pichler, Wen Wei Ho, Soonwon Choi, Subir Sachdev, Markus Greiner, Vladan Vuletić, and Mikhail D. Lukin. Quantum phases of matter on a 256-atom programmable quantum simulator. *Nature*, 595(7866):227–232, July 2021.
- [65] Cheng Chin, Rudolf Grimm, Paul Julienne, and Eite Tiesinga. Feshbach resonances in ultracold gases. *Reviews of Modern Physics*, 82(2):1225–1286, 2010.
- [66] W. Ketterle, D. S. Durfee, and D. M. Stamper-Kurn. Making, probing and understanding Bose-Einstein condensates. *arXiv:cond-mat/9904034*, 1999.
- [67] Immanuel Bloch. Ultracold quantum gases in optical lattices. *Nature Physics*, 1(1):23–30, 2005.
- [68] Immanuel Bloch, Jean Dalibard, and Wilhelm Zwerger. Many-body physics with ultracold gases. *Reviews of Modern Physics*, 80(3):885–964, 2008.
- [69] W. Ketterle and M. W. Zwierlein. Making, probing and understanding ultracold Fermi gases. *La Rivista del Nuovo Cimento*, 31(5):247–422, 2008.
- [70] Immanuel Bloch, Jean Dalibard, and Sylvain Nascimbène. Quantum simulations with ultracold quantum gases. *Nature Physics*, 2012.
- [71] Leticia Tarruell and Laurent Sanchez-Palencia. Quantum simulation of the Hubbard model with ultracold fermions in optical lattices. *Comptes Rendus Physique*, 19(6):365–393, 2018.

Bibliography

- [72] Christian Gross and Waseem S. Bakr. Quantum gas microscopy for single atom and spin detection. *Nature Physics*, 17(12):1316–1323, 2021.
- [73] K. B. Davis, M. O. Mewes, M. R. Andrews, N. J. van Druten, D. S. Durfee, D. M. Kurn, and W. Ketterle. Bose-einstein condensation in a gas of sodium atoms. *Phys. Rev. Lett.*, 75:3969–3973, Nov 1995.
- [74] Markus Greiner, Olaf Mandel, Tilman Esslinger, Theodor W. Hänsch, and Immanuel Bloch. Quantum phase transition from a superfluid to a Mott insulator in a gas of ultracold atoms. *Nature*, 415(6867):39–44, 2002.
- [75] Markus Greiner, Cindy A. Regal, and Deborah S. Jin. Emergence of a molecular Bose-Einstein condensate from a Fermi gas. *Nature*, 426(6966):537–540, 2003.
- [76] Robert Jördens, Niels Strohmaier, Kenneth Günter, Henning Moritz, and Tilman Esslinger. A Mott insulator of fermionic atoms in an optical lattice. *Nature*, 455(7210):204–207, 2008.
- [77] U. Schneider, L. Hackermüller, S. Will, Th. Best, I. Bloch, T. A. Costi, R. W. Helmes, D. Rasch, and A. Rosch. Metallic and Insulating Phases of Repulsively Interacting Fermions in a 3D Optical Lattice. *Science*, 322(5907):1520–1525, 2008.
- [78] Stefan Kuhr. Quantum-gas microscopes: a new tool for cold-atom quantum simulators. *National Science Review*, 3(2):170–172, 2016.
- [79] Waseem S. Bakr, Jonathon I. Gillen, Amy Peng, Simon Fölling, and Markus Greiner. A quantum gas microscope for detecting single atoms in a Hubbard-regime optical lattice. *Nature*, 462(7269):74–77, 2009.
- [80] W. S. Bakr, A. Peng, M. E. Tai, R. Ma, J. Simon, J. I. Gillen, S. Fölling, L. Pollet, and M. Greiner. Probing the Superfluid-to-Mott Insulator Transition at the Single-Atom Level. *Science*, 329(5991):547–550, 2010.

Bibliography

- [81] Jacob F. Sherson, Christof Weitenberg, Manuel Endres, Marc Cheneau, Immanuel Bloch, and Stefan Kuhr. Single-atom-resolved fluorescence imaging of an atomic Mott insulator. *Nature*, 467(7311):68–72, 2010.
- [82] Lawrence W. Cheuk, Matthew A. Nichols, Melih Okan, Thomas Gersdorf, Vinay V. Ramasesh, Waseem S. Bakr, Thomas Lompe, and Martin W. Zwierlein. Quantum-Gas Microscope for Fermionic Atoms. *Physical Review Letters*, 114(19):193001, 2015.
- [83] Elmar Haller, James Hudson, Andrew Kelly, Dylan A. Cotta, Bruno Peaudecerf, Graham D. Bruce, and Stefan Kuhr. Single-atom imaging of fermions in a quantum-gas microscope. *Nature Physics*, 11(9):738–742, 2015.
- [84] Daniel Greif, Maxwell F. Parsons, Anton Mazurenko, Christie S. Chiu, Sebastian Blatt, Florian Huber, Geoffrey Ji, and Markus Greiner. Site-resolved imaging of a fermionic Mott insulator. *Science*, 351(6276):953–957, 2016.
- [85] Lawrence W. Cheuk, Matthew A. Nichols, Katherine R. Lawrence, Melih Okan, Hao Zhang, and Martin W. Zwierlein. Observation of 2D fermionic Mott insulators of ^{40}K with single-site resolution. *Physical Review Letters*, 116(23):235301, 2016.
- [86] V. Celebonovic. The two dimensional Hubbard model:a theoretical tool for molecular electronics. *Journal of Physics: Conference Series*, 253:012004, 2010.
- [87] D. J. Scalapino. A common thread: The pairing interaction for unconventional superconductors. *Rev. Mod. Phys.*, 84(4):1383–1417, 2012.
- [88] Yoshiharu Krockenberger and Hideki Yamamoto. High-temperature Superconductivity without Doping - Synthesis of Conceptually New Superconductors. *NTT Technical Review*, 12(8):7, 2014.
- [89] Marc Cheneau, Peter Barmettler, Dario Poletti, Manuel Endres, Peter Schauß, Takeshi Fukuhara, Christian Gross, Immanuel Bloch, Corinna Kollath, and Ste-

Bibliography

- fan Kuhr. Light-cone-like spreading of correlations in a quantum many-body system. *Nature*, 481(7382):484–487, 2012.
- [90] Manuel Endres, Marc Cheneau, Takeshi Fukuhara, Christof Weitenberg, Peter Schauß, Christian Gross, Leonardo Mazza, Mari Carmen Banuls, Lode Pollet, Immanuel Bloch, and Stefan Kuhr. Single-site- and single-atom-resolved measurement of correlation functions. *Applied Physics B*, 113(1):27–39, 2013.
- [91] Anton Mazurenko, Christie S. Chiu, Geoffrey Ji, Maxwell F. Parsons, Márton Kanász-Nagy, Richard Schmidt, Fabian Grusdt, Eugene Demler, Daniel Greif, and Markus Greiner. A cold-atom Fermi-Hubbard antiferromagnet. *Nature*, 545(7655):462–466, 2017.
- [92] Russell A. Hart, Pedro M. Duarte, Tsung Lin Yang, Xinxing Liu, Thereza Paiva, Ehsan Khatami, Richard T. Scalettar, Nandini Trivedi, David A. Huse, and Randall G. Hulet. Observation of antiferromagnetic correlations in the Hubbard model with ultracold atoms. *Nature*, 519(7542):211–214, 2015.
- [93] Joannis Koepsell, Jayadev Vijayan, Pimonpan Sompert, Fabian Grusdt, Timon A. Hilker, Eugene Demler, Guillaume Salomon, Immanuel Bloch, and Christian Gross. Imaging magnetic polarons in the doped Fermi-Hubbard model. *Nature*, 572(7769):358–362, 2019.
- [94] Joannis Koepsell, Dominik Bourgund, Pimonpan Sompert, Sarah Hirthe, Annabelle Bohrdt, Yao Wang, Fabian Grusdt, Eugene Demler, Guillaume Salomon, Christian Gross, and Immanuel Bloch. Microscopic evolution of doped Mott insulators from polaronic metal to Fermi liquid. *Science*, 374(6563):82–86, 2021.
- [95] Christie S. Chiu, Geoffrey Ji, Annabelle Bohrdt, Muqing Xu, Michael Knap, Eugene Demler, Fabian Grusdt, Markus Greiner, and Daniel Greif. String patterns in the doped Hubbard model. *Science*, 365(6450):251–256, 2019.
- [96] A. Recati, P. O. Fedichev, W. Zwerger, and P. Zoller. Spin-charge separation in ultra-cold quantum gases. *Physical Review Letters*, 90(2):020401, 2003.

Bibliography

- [97] Jayadev Vijayan, Pimonpan Sompet, Guillaume Salomon, Joannis Koepsell, Sarah Hirthe, Annabelle Bohrdt, Fabian Grusdt, Immanuel Bloch, and Christian Gross. Time-resolved observation of spin-charge deconfinement in fermionic Hubbard chains. *Science*, 367(6474):186–189, 2020.
- [98] John L. Bohn. Cooper pairing in ultracold k-40 using feshbach resonances. *Physical Review A*, 61(5), apr 2000.
- [99] W. Hofstetter, J. I. Cirac, P. Zoller, E. Demler, and M. D. Lukin. High-temperature superfluidity of fermionic atoms in optical lattices. *Physical Review Letters*, 89(22):220407, November 2002. arXiv:cond-mat/0204237.
- [100] Prof Rafael M Fernandes. Lecture Notes : BCS theory of superconductivity. Technical report, 1911.
- [101] Florian Schreck and Klaasjan van Druten. Laser cooling for quantum gases. *Nature Physics 2021 17:12*, 17(12):1296–1304, 2021.
- [102] G. D. Bruce, E. Haller, B. Peaudecerf, D. A. Cotta, M. Andia, S. Wu, M. Y. H. Johnson, B. W. Lovett, and S. Kuhr. Sub-Doppler laser cooling of ^{40}K with Raman gray molasses on the D2 line. *Journal of Physics B: Atomic, Molecular and Optical Physics*, 50(9):095002, 2017.
- [103] William D. Phillips. Nobel Lecture: Laser cooling and trapping of neutral atoms. *Rev. Mod. Phys.*, 70(3):721–741, 1998.
- [104] E. L. Raab, M. Prentiss, Alex Cable, Steven Chu, and D. E. Pritchard. Trapping of Neutral Sodium Atoms with Radiation Pressure. *Phys. Rev. Lett.*, 59(23):2631–2634, 1987.
- [105] J Dalibard and C Cohen-Tannoudji. Laser cooling below the Doppler limit by polarization gradients: simple theoretical models. *Journal of the Optical Society of America B*, 6(11):2023, 1989.
- [106] C.J. Foot. Atomic Physics (Oxford Master Series in Atomic, Optical and Laser Physics). *Citeulike.Org*, 2005.

Bibliography

- [107] Paul D. Lett, Richard N. Watts, Christoph I. Westbrook, William D. Phillips, Phillip L. Gould, and Harold J. Metcalf. Observation of Atoms Laser Cooled below the Doppler Limit. *Physical Review Letters*, 61(2):169–172, 1988.
- [108] Mikhail D. Lukin. *Modern Atomic and Optical Physics II*. Lecture Notes. Harvard University, 2016.
- [109] Paul D. Lett, Richard N. Watts, Christoph I. Westbrook, William D. Phillips, Phillip L. Gould, and Harold J. Metcalf. Observation of atoms laser cooled below the doppler limit. *Phys. Rev. Lett.*, 61:169–172, Jul 1988.
- [110] B. Peaudecerf, M. Andia, M. Brown, E. Haller, and S. Kuhr. Microwave preparation of two-dimensional fermionic spin mixtures. *New Journal of Physics*, 21(1):013020, 2019.
- [111] Hans G. Dehmelt. Entropy reduction by motional sideband excitation. *Nature*, 262(5571):777, 1976.
- [112] D J Wineland and Wayne M Itano. Laser cooling of atoms. *Physical Review A*, 20(4):1521–1540, 1979.
- [113] F. Diedrich, J. C. Bergquist, Wayne M. Itano, and D. J. Wineland. Laser Cooling to the Zero-Point Energy of Motion. *Physical Review Letters*, 62(4):403, 1989.
- [114] W Neuhauser, M Hohenstatt, P Toschek, and H Dehmelt. Optical-sideband cooling of visible atom cloud confined in parabolic well. *Physical Review Letters*, 41(4):233–236, 1978.
- [115] D J Heinzen and D J Wineland. Quantum-limited cooling and detection of radio-frequency oscillations by laser-cooled ions. *Physical Review A*, 42(5):2977–2994, 1990.
- [116] Giovanna Morigi, Jürgen Eschner, and Christoph H. Keitel. Ground state laser cooling using electromagnetically induced transparency. *Physical Review Letters*, 85(21):4458–4461, 2000.

Bibliography

- [117] C. Monroe, D. M. Meekhof, B. E. King, S. R. Jefferts, W. M. Itano, D. J. Wineland, and P. Gould. Resolved-sideband Raman cooling of a bound atom to the 3D zero-point energy. *Physical Review Letters*, 75(22):4011–4014, 1995.
- [118] C. S. Roos, D. Leibfried, A. Mundt, F. Schmidt-Kaler, J. Eschner, and R. Blatt. Experimental Demonstration of Ground State Laser Cooling with Electromagnetically Induced Transparency. *Physical Review Letters*, 85(26):5547–5550, 2000.
- [119] H. Perrin, A. Kuhn, I. Bouchoule, and C. Salomon. Sideband cooling of neutral atoms in a far-detuned optical lattice. *Europhysics Letters*, 42(4):395–400, 1998.
- [120] Tobias Kampschulte, Wolfgang Alt, Sebastian Manz, Miguel Martinez-Dorantes, René Reimann, Seokchan Yoon, Dieter Meschede, Marc Bienert, and Giovanna Morigi. Electromagnetically-induced-transparency control of single-atom motion in an optical cavity. *Physical Review A - Atomic, Molecular, and Optical Physics*, 89(3):033404, 2014.
- [121] Maxwell F. Parsons, Florian Huber, Anton Mazurenko, Christie S. Chiu, Widagdo Setiawan, Katherine Wooley-Brown, Sebastian Blatt, and Markus Greiner. Site-Resolved imaging of fermionic li 6 in an optical lattice. *Physical Review Letters*, 114(21):213002, 2015.
- [122] Ryuta Yamamoto, Jun Kobayashi, Takuma Kuno, Kohei Kato, and Yoshiro Takahashi. An ytterbium quantum gas microscope with narrow-line laser cooling. *New Journal of Physics*, 18(2):023016, 2016.
- [123] Michael Gröbner, Philipp Weinmann, Emil Kirilov, and Hanns Christoph Nägerl. Degenerate Raman sideband cooling of K 39. *Physical Review A*, 95(3), 2017.
- [124] Lawrence W Cheuk, Matthew A Nichols, Melih Okan, Thomas Gersdorf, Vinay V Ramasesh, Waseem S Bakr, Thomas Lompe, and Martin W Zwierlein. Quantum-gas microscope for fermionic atoms. *Physical Review Letters*, 114(19), 2015.
- [125] V M Porozova, L V Gerasimov, I B Bobrov, S S Straupe, S P Kulik, and D V Kupriyanov. Raman sideband cooling of a single atom in an optical dipole trap:

Bibliography

- Toward a theoretical optimum in a three-dimensional regime. *Physical Review A*, 99(4), 2019.
- [126] P Sompert, Y H Fung, E Schwartz, M. D.J. Hunter, J Phrompao, and M F Andersen. Zeeman-insensitive cooling of a single atom to its two-dimensional motional ground state in tightly focused optical tweezers. *Physical Review A*, 95(3):31403, 2017.
- [127] Jiazhong Hu, Alban Urvoy, Zachary Vendeiro, Valentin Crépel, Wenlan Chen, and Vladan Vuletić. Creation of a Bose-condensed gas of 87Rb by laser cooling. *Science*, 358(6366):1078–1080, 2017.
- [128] D. J. Wineland, C. Monroe, W. M. Itano, D. Leibfried, B. E. King, and D. M. Meekhof. Experimental Issues in Coherent Quantum-State Manipulation of Trapped Atomic Ions. *Journal of Research of the National Institute of Standards and Technology*, 103(3):259–328, 1998.
- [129] Daniel Adam Steck. Quantum and Atom Optics, Lecture Notes. *Book*, 2012.
- [130] M Squared. Ti Sapphire Laser - <https://www.m2lasers.com/solstis.html>.
- [131] moglabs. Tunable cateye laser - <https://www.moglabs.com/products/cateye-laser>.
- [132] Toptica Eagleyard. GAIN CHIPS AR coated Fabry-Perot laser - eyp-rwe-0790.
- [133] L. B. Lucy. An iterative technique for the rectification of observed distributions. *The Astronomical Journal*, 79(6):745, 1974.
- [134] Elmar Haller, James Hudson, Andrew Kelly, Dylan A. Cotta, Bruno Peaudecerf, Graham D. Bruce, and Stefan Kuhr. Single-atom imaging of fermions in a quantum-gas microscope. *Nature Physics*, 11(9):738–742, 2015.
- [135] G. J.A. Edge, R Anderson, D Jervis, D. C. McKay, R. Day, S Trotzky, and J H Thywissen. Imaging and addressing of individual fermionic atoms in an optical lattice. *Physical Review A - Atomic, Molecular, and Optical Physics*, 92(6), 2015.

Bibliography

- [136] Regina Lechner, Christine Maier, Cornelius Hempel, Petar Jurcevic, Ben P Lanyon, Thomas Monz, Michael Brownnutt, Rainer Blatt, and Christian F Roos. Electromagnetically-induced-transparency ground-state cooling of long ion strings. *Physical Review A*, 93(5), 2016.
- [137] I A Semerikov, I V Zalivako, A S Borisenko, K Y Khabarova, and N N Kolachevsky. EIT Ground State Cooling Scheme of 171Yb^+ Based on the $2S_{1/2} \rightarrow 2P_{1/2}$ Cooling Transition. *Journal of Russian Laser Research*, 39(6):568–574, 2018.
- [138] Nils Scharnhorst, Javier Cerrillo, Johannes Kramer, Ian D Leroux, Jannes B Wübbena, Alex Retzker, and Piet O Schmidt. Experimental and theoretical investigation of a multimode cooling scheme using multiple electromagnetically-induced-transparency resonances. *Physical Review A*, 98(2), 2018.
- [139] J. R. Johansson, P. D. Nation, and Franco Nori. QuTiP: An open-source Python framework for the dynamics of open quantum systems. *Computer Physics Communications*, 183(8):1760–1772, 2012.
- [140] Andrew J. Daley. Quantum trajectories and open many-body quantum systems. *Advances in Physics*, 63(2):77–149, 2014.
- [141] Yurii A. Izyumov. Strongly correlated electrons: the t-J model. *Physics-Uspokhi*, 40(5):445, 1997.
- [142] Andrey R. Kolovsky. Quantum entanglement and the Born-Markov approximation for an open quantum system. *Physical Review E*, 101(6):062116, 2020.
- [143] Stig Stenholm. The semiclassical theory of laser cooling. *Reviews of Modern Physics*, 1986.
- [144] Kazuyuki Fujii and Kazuyuki Fujii. Introduction to the Rotating Wave Approximation (RWA): Two Coherent Oscillations. *Journal of Modern Physics*, 8(12):2042–2058, 2017.
- [145] I. I. Rabi. Space quantization in a gyrating magnetic field. *Physical Review*, 1937.

Bibliography

- [146] Wilhelm Zwerger. Mott Hubbard transition of cold atoms in optical lattices. *Journal of Optics B: Quantum and Semiclassical Optics*, 5(2):S9–S16, 2003.
- [147] David Tong. Band Structure. In *Lectures on Solid State Physics*. 2017.
- [148] Andres. Ulibarrena. *Creation of an all-optical Bose-Einstein condensate*. PhD thesis, University of Strathclyde, 2020.
- [149] Ilian Despard. *The Construction of a Bosonic Quantum-Gas Microscope*. PhD thesis, University of Strathclyde, 2021.
- [150] Caroline L. Blackley, C. Ruth Le Sueur, Jeremy M. Hutson, Daniel J. McCarron, Michael P. Köppinger, Hung-Wen Cho, Daniel L. Jenkin, and Simon L. Cornish. Feshbach resonances in ultracold ^{85}Rb . 2012.
- [151] S. B. Papp and C. E. Wieman. Observation of Heteronuclear Feshbach Molecules from a $^{85}\text{Rb} - ^{87}\text{Rb}$ Gas. *Physical Review Letters*, 97(18):180404, 2006.
- [152] Ph. Courteille, R. S. Freeland, D. J. Heinzen, F. A. van Abeelen, and B. J. Verhaar. Observation of a Feshbach Resonance in Cold Atom Scattering. *Physical Review Letters*, 81(1):69–72, 1998.
- [153] J. L. Roberts, N. R. Claussen, James P. Burke, Chris H. Greene, E. A. Cornell, and C. E. Wieman. Resonant Magnetic Field Control of Elastic Scattering in Cold ^{85}Rb . *Physical Review Letters*, 81(23):5109–5112, 1998.
- [154] P. A. Ruprecht, M. J. Holland, K. Burnett, and Mark Edwards. Time-dependent solution of the nonlinear Schrödinger equation for Bose-condensed trapped neutral atoms. *Physical Review A*, 51(6):4704–4711, 1995.
- [155] Franco Dalfovo, Stefano Giorgini, Lev P. Pitaevskii, and Sandro Stringari. Theory of Bose-Einstein condensation in trapped gases. *Reviews of Modern Physics*, 71(3):463–512, 1999.
- [156] S. L. Cornish, N. R. Claussen, J. L. Roberts, E. A. Cornell, and C. E. Wieman. Stable ^{85}Rb Bose-Einstein Condensates with Widely Tunable Interactions. *Physical Review Letters*, 85(9):1795–1798, 2000.

Bibliography

- [157] A. L. Marchant, S. Händel, S. A. Hopkins, T. P. Wiles, and S. L. Cornish. Bose-Einstein condensation of ^{85}Rb by direct evaporation in an optical dipole trap. *Physical Review A*, 85(5):053647, 2012.
- [158] N. R. Claussen, E. A. Donley, S. T. Thompson, and C. E. Wieman. Microscopic Dynamics in a Strongly Interacting Bose-Einstein Condensate. *Physical Review Letters*, 89(1):010401, 2002.
- [159] B. Damski, L. Santos, E. Tiemann, M. Lewenstein, S. Kotochigova, P. Julienne, and P. Zoller. Creation of a Dipolar Superfluid in Optical Lattices. *Physical Review Letters*, 90(11):110401, 2003.
- [160] Ehud Altman, Walter Hofstetter, Eugene Demler, and Mikhail D. Lukin. Phase diagram of two-component bosons on an optical lattice. *New Journal of Physics*, 5:113–113, 2003.
- [161] James P. Burke, John L. Bohn, B. D. Esry, and Chris H. Greene. Prospects for Mixed-Isotope Bose-Einstein Condensates in Rubidium. *Physical Review Letters*, 80(10):2097–2100, 1998.
- [162] Lennart Koehn. *Laser cooling and trapping of ^{85}Rb* . MSc Report, University of Strathclyde, 2022.
- [163] E. Arimondo. V Coherent Population Trapping in Laser Spectroscopy. *Progress in Optics*, 35(C):257–354, 1996.
- [164] A. Aspect, E. Arimondo, R. Kaiser, N. Vansteenkiste, and C. Cohen-Tannoudji. Laser Cooling below the One-Photon Recoil Energy by Velocity-Selective Coherent Population Trapping. *Physical Review Letters*, 61(7):826–829, 1988.
- [165] Fam Le Kien and V I Balykin. Atom cooling by VSCPT: Accumulation plus filtering. *Journal of Experimental and Theoretical Physics*, 88(2):246–253, 1999.
- [166] M. Weidemüller, T Esslinger, M. A. Ol’shanii, A Hemmerich, and T. W. Hänsch. A novel scheme for efficient cooling below the photon recoil limit. *EPL*, 27(2):109–114, 1994.

Bibliography

- [167] G. Grynberg and J.-Y. Courtois. Proposal for a Magneto-Optical Lattice for Trapping Atoms in Nearly-Dark States. *Europhysics Letters (EPL)*, 27(1):41–46, 1994.
- [168] D. E. Pritchard, K. Helmerson, V. S. Bagnato, G. P. Laffyatis, and A. G. Martin. Optical Pumping in Translation Space. In Willy Persson and Sune Svanberg, editors, *Laser Spectroscopy VIII*, Springer Series in Optical Sciences, pages 68–72, Berlin, Heidelberg, 1987.
- [169] Sara Rosi, Alessia Burchianti, Stefano Conclave, Devang S. Naik, Giacomo Roati, Chiara Fort, and Francesco Minardi. λ -enhanced grey molasses on the D 2 transition of Rubidium-87 atoms. *Scientific Reports*, 8(1):1–9, 2018.
- [170] Ya Fen Hsiao, Yu Ju Lin, and Ying Cheng Chen. λ -enhanced gray-molasses cooling of cesium atoms on the D2 line. *Physical Review A*, 98(3):033419, 2018.
- [171] Andrew T. Grier, Igor Ferrier-Barbut, Benno S. Rem, Marion Delehaye, Lev Khaykovich, Frédéric Chevy, and Christophe Salomon. λ -enhanced sub-Doppler cooling of lithium atoms in D1 gray molasses. *Physical Review A - Atomic, Molecular, and Optical Physics*, 87(6):063411, 2013.
- [172] Dipankar Nath, R. Kollengode Easwaran, G. Rajalakshmi, and C. S. Unnikrishnan. Quantum-interference-enhanced deep sub-Doppler cooling of 39K atoms in gray molasses. *Physical Review A - Atomic, Molecular, and Optical Physics*, 88(5):053407, 2013.
- [173] G. D. Bruce, E. Haller, B. Peaudecerf, D. A. Cotta, M. Andia, S. Wu, M. Y.H. Johnson, B. W. Lovett, and S. Kuhr. Sub-Doppler laser cooling of 40K with Raman gray molasses on the D2 line. *Journal of Physics B: Atomic, Molecular and Optical Physics*, 2017.
- [174] Larry J. Hornbeck, T. Russ Howell, Richard L. Knipe, and Michael A. Mignardi. Digital Micromirror Device™: Commercialization of a Massively Parallel MEMS Technology. In *Microelectromechanical Systems (MEMS)*, pages 3–8, Dallas, Texas, USA, 1997.

Bibliography

- [175] Clemens Ulm. *Multi-Site Addressing of Single Atoms in a Quantum Gas Microscope*. PhD thesis, University of Strathclyde, 2022.
- [176] G. Gauthier, I. Lenton, N. McKay Parry, M. Baker, M. J. Davis, H. Rubinsztein-Dunlop, and T. W. Neely. Direct imaging of a digital-micromirror device for configurable microscopic optical potentials. *Optica*, 3(10):1136–1143, 2016.
- [177] Guillaume Gauthier, Thomas A. Bell, Alexander B. Stilgoe, Mark Baker, Halina Rubinsztein-Dunlop, and Tyler W. Neely. Chapter One - Dynamic high-resolution optical trapping of ultracold atoms. In Louis F. Dimauuro, H el ene Perrin, and Susanne F. Yelin, editors, *Advances In Atomic, Molecular, and Optical Physics*, volume 70, pages 1–101. 2021.
- [178] K. Ziegler. Two-component Bose gas in an optical lattice at single-particle filling. *Physical Review A*, 68(5):053602, 2003.
- [179] Jize Zhao, Shijie Hu, Jun Chang, Ping Zhang, and Xiaoqun Wang. Ferromagnetism in a two-component Bose-Hubbard model with synthetic spin-orbit coupling. *Physical Review A*, 89(4):043611, 2014.
- [180] Rajibul Islam, Ruichao Ma, Philipp M. Preiss, M. Eric Tai, Alexander Lukin, Matthew Rispoli, and Markus Greiner. Measuring entanglement entropy in a quantum many-body system. *Nature*, 528(7580):77–83, 2015.
- [181] Matthew Rispoli, Alexander Lukin, Robert Schittko, Sooshin Kim, M. Eric Tai, Julian L eonard, and Markus Greiner. Quantum critical behaviour at the many-body localization transition. *Nature*, 573(7774):385–389, 2019.
- [182] D.J. Wineland, C. Monroe, W.M. Itano, D. Leibfried, B.E. King, and D.M. Meekhof. Experimental issues in coherent quantum-state manipulation of trapped atomic ions. *Journal of Research of the National Institute of Standards and Technology*, 103(3):259, May 1998.